PREFACE TO THE EDITION

The forthcoming issue of the **International Journal of Pure Science Research Studies (IJPSRS)** presents a rich and intellectually rigorous collection of articles that span fundamental scientific inquiry across environmental science, physics, mathematics, and cryptography. The contributions in this volume reflect the journal's commitment to advancing theoretical depth, quantitative precision, and experimental insight in the pure sciences.

Environmental and Earth system sciences feature prominently in this issue. The analysis of ocean deoxygenation synthesizes current understanding of anthropogenic impacts on marine oxygen cycles, highlighting the expansion of hypoxic zones and the urgent need for integrated climate and nutrient management strategies. Complementing this, the comprehensive study of carbon cycle dynamics provides a quantitative assessment of global carbon fluxes, sink efficiencies, and feedback mechanisms, offering critical insights into climate stabilization pathways under ongoing anthropogenic perturbations.

In the realm of physics and cosmology, this issue explores both the quantum and cosmic frontiers. A theoretical investigation into quantum Higgs echoes in superconductors proposes a novel mechanism for quantum memory storage, advancing the application of collective quantum modes in emerging technologies. At cosmological scales, the examination of gravitational lensing presents compelling experimental evidence for dark matter, reinforcing its foundational role in contemporary astrophysics through observational and theoretical synthesis.

Mathematical and computational rigor is further demonstrated in the convergence analysis of the Newton-Raphson method for nonlinear integral equations, extending classical finite-dimensional theory into Banach spaces and establishing robust analytical error bounds. Meanwhile, the algebraic study of elliptic curve cryptography deepens understanding of the discrete logarithm problem, reaffirming the mathematical foundations that secure modern communication systems.

Collectively, the articles in this issue exemplify the breadth and depth of pure science research from subatomic phenomena to cosmic structures, from abstract mathematical theory to environmental system dynamics. The editorial board expresses sincere appreciation to the authors and reviewers whose scholarship and dedication have shaped this volume. We trust that this issue will contribute meaningfully to ongoing scientific discourse and inspire further exploration across the foundational sciences.

Dr. Sandhya E
Chief Editor

CONTENTS

INTERNATIONAL JOURNAL OF PURE SCIENCE RESEARCH STUDIES (IJPSRS)
(Open Access, Double-Blind Peer Reviewed Journal)
ISSN Online: ISSN Print
EDU SCHOOL
ijpsrs.com

Ocean Deoxygenation: Causes, Consequences, and Conservation Strategies

Kesavan K

Associate Professor and Head, Department of Aquaculture, MES Asmabi College, Vemballur, Kerala, India

Article information
Received: 4th August 2025
Received in revised form: 12th September 2025
Accepted: 15th October 2025
Available online: 14th November 2025

Volume: 1
Issue: 1
DOI: https://doi.org/10.5281/zenodo.17607758

Abstract

Ocean deoxygenation represents a critical consequence of anthropogenic climate change and nutrient pollution, yet remains under-recognized compared to ocean warming and acidification. This paper synthesizes current understanding of the mechanisms driving oxygen loss in marine environments, evaluates cascading ecological and biogeochemical consequences, and assesses conservation strategies. Global ocean dissolved oxygen has declined approximately 2% since 1960, with oxygen minimum zones expanding and coastal hypoxic areas increasing tenfold. Primary drivers include warming-induced stratification reducing oxygen solubility and ventilation, alongside eutrophication-driven microbial respiration in coastal waters. Consequences span cellular stress responses and metabolic constraints to habitat compression, biodiversity loss, and altered biogeochemical cycles including enhanced greenhouse gas emissions. Effective conservation requires integrated approaches: climate mitigation to address thermal deoxygenation through emissions reductions aligned with Paris Agreement targets, and comprehensive nutrient management combining agricultural best practices, wastewater treatment upgrades, and watershed restoration. We propose an integrated framework spanning global climate policy to local watershed management, emphasizing adaptive management, enhanced monitoring through autonomous platforms, and recognition of multi-decadal response timescales. Success demands unprecedented coordination across disciplines, sectors, and jurisdictions, guided by robust science while accommodating inherent uncertainties in this complex Earth system challenge.

Keywords: Ocean Deoxygenation, Hypoxia, Eutrophication, Climate Change, Marine Conservation, Biogeochemical Cycles

I. INTRODUCTION

The world's oceans contain approximately 200 times less dissolved oxygen (DO) than the atmosphere, making marine organisms highly vulnerable to oxygen availability changes[1]. Since the mid-20th century, global ocean oxygen content has declined by more than 2%, with oxygen-depleted waters expanding substantially[2]. This phenomenon operates through two primary pathways: thermal deoxygenation in open oceans driven by warming-induced stratification, and eutrophication-driven hypoxia in coastal systems influenced by nutrient over-enrichment[3]. The expansion of oxygen minimum zones (OMZs) in tropical oceans and proliferation of seasonal hypoxic "dead zones" in coastal waters represent distinct expressions of this global challenge.

Despite growing recognition, significant knowledge gaps persist regarding the relative contributions of various drivers, non-linear interactions between thermal and nutrient-driven processes, and effectiveness of proposed mitigation strategies across different oceanographic contexts. This paper addresses these gaps through four objectives:

- Elucidate physical, chemical, and biological mechanisms driving oxygen loss
- Synthesize evidence regarding ecological, biogeochemical, and socioeconomic consequences
- Critically assess conservation and mitigation strategies
- Propose an integrated management framework recognizing regional heterogeneity while providing actionable guidance.

We employ a synthetic analytical approach, integrating empirical data from global ocean observation systems including the World Ocean Database and Global Ocean Oxygen Database, results from mechanistic biogeochemical models, and theoretical frameworks from marine ecology. The analysis examines temporal trends, spatial patterns, and correlations with physical and biogeochemical drivers, while evaluating conservation strategies through comparative analysis across regional contexts.

II. MECHANISMS OF OCEAN DEOXYGENATION

1.1. Fundamental Oxygen Dynamics

Dissolved oxygen concentrations result from the balance between supply and consumption processes. Oxygen enters through air-sea gas exchange and photosynthetic production, with solubility depending inversely on temperature and salinity[4]. Supply to subsurface waters occurs through advection, mixing, and ventilation. Consumption occurs throughout the water column via aerobic respiration, with microbial decomposition of organic matter representing the dominant sink[5]. The biological pump—organic matter sinking from surface waters—delivers oxygen demand to depth.

Figure 1: ocean oxygen balance

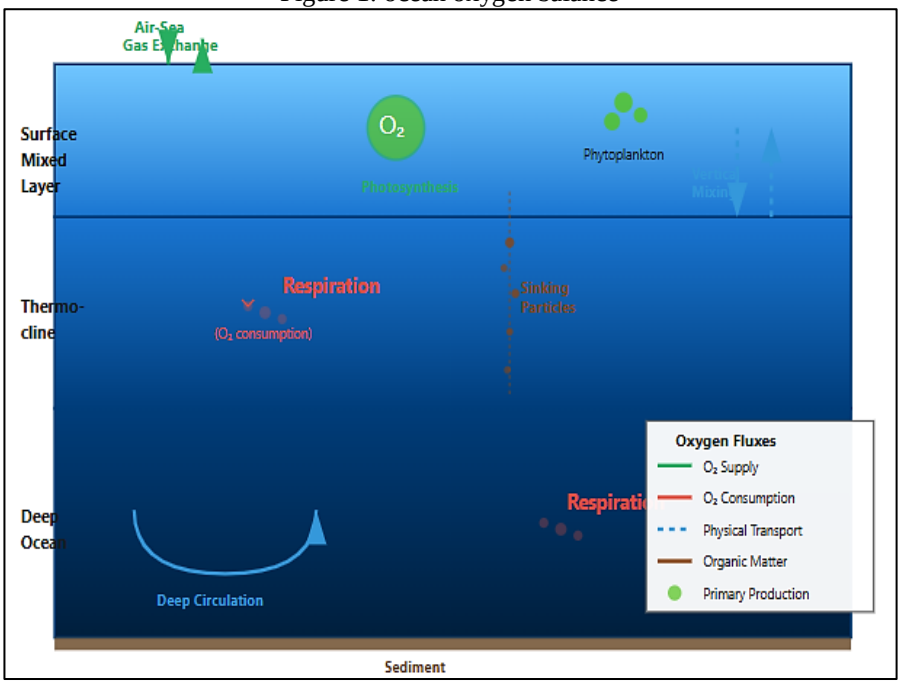

Figure 1 Shows a Conceptual diagram showing oxygen balance in the ocean, including air-sea exchange, photosynthetic production, physical transport mechanisms, and respiratory consumption at different depths. The figure should illustrate the vertical structure of the ocean with surface mixed layer, thermocline, and deep ocean, with arrows indicating oxygen fluxes.

1.2. Thermal Deoxygenation

Thermal deoxygenation refers to oxygen loss driven by ocean warming and associated circulation changes, operating globally but particularly evident in subtropical and tropical OMZs[6]. Multiple interconnected processes contribute:

- Reduced Solubility: Oxygen solubility decreases approximately 1.4% per degree Celsius[7]. Given surface warming of ~0.6°C since 1950, solubility effects alone account for ~0.8% oxygen decline.
- Enhanced Stratification: Preferential surface warming increases temperature gradients, reducing vertical mixing and ventilation of subsurface layers[8]. Shoaling mixed layers may increase surface productivity in some regions while reducing nutrient supply to euphotic zones in others.

- Circulation Changes: Large-scale circulation patterns respond to surface warming and altered atmospheric forcing. Modeling suggests weakening Atlantic Meridional Overturning Circulation and shifts in thermocline ventilation depth and intensity[9], affecting oxygen supply to intermediate-depth waters forming OMZ cores.
- Metabolic Amplification: Temperature-dependence of metabolic rates exceeds that of oxygen solubility, creating a "metabolic squeeze" wherein warming reduces supply while increasing demand[10]. This effect intensifies at low oxygen concentrations where organisms operate near physiological thresholds.

Observational evidence confirms significant OMZ expansion in tropical Pacific, Indian, and Atlantic Oceans[11]. Analysis reveals the volume of water with oxygen below 80 µmol/kg increased approximately 4.5 million km³ between 1960 and 2010, with pronounced changes in tropical thermocline waters at 200-700m depths.

1.3. Eutrophication-Driven Coastal Hypoxia

Coastal hypoxia develops through anthropogenic nutrient loading, algal blooms, and enhanced respiration during organic matter decomposition, typically in semi-enclosed systems with restricted circulation[12].

- Nutrient Loading: Human activities dramatically increased nutrient delivery through agricultural runoff, urban wastewater, atmospheric deposition, and aquaculture effluents. Global riverine nitrogen export increased 2-3 fold since pre-industrial times[13].
- Primary Production and Export: Elevated nutrients stimulate phytoplankton growth, increasing primary production. While initially increasing oxygen production, subsequent sinking and decomposition creates intense oxygen demand in bottom waters, with efficiency depending on stratification preventing re-aeration.
- Stratification Dynamics: Seasonal patterns interact with nutrient loading: spring/summer warming establishes thermal stratification, river discharge creates salinity stratification, and the combination isolates bottom waters from atmospheric oxygen supply.
- Feedback Mechanisms: Hypoxia development triggers positive feedbacks including phosphorus release from sediments, altered microbial communities shifting toward anaerobic metabolism, reduced bioturbation, and decreased grazing pressure.

Documented coastal hypoxic zones increased from approximately 10 in 1960 to over 500 currently, with total affected area exceeding 245,000 km² [14]. Major systems include the northern Gulf of Mexico, Baltic Sea, northwestern Black Sea continental shelf, and numerous smaller systems worldwide

Figure 2: Mechanisms of Ocean Deoxygenation

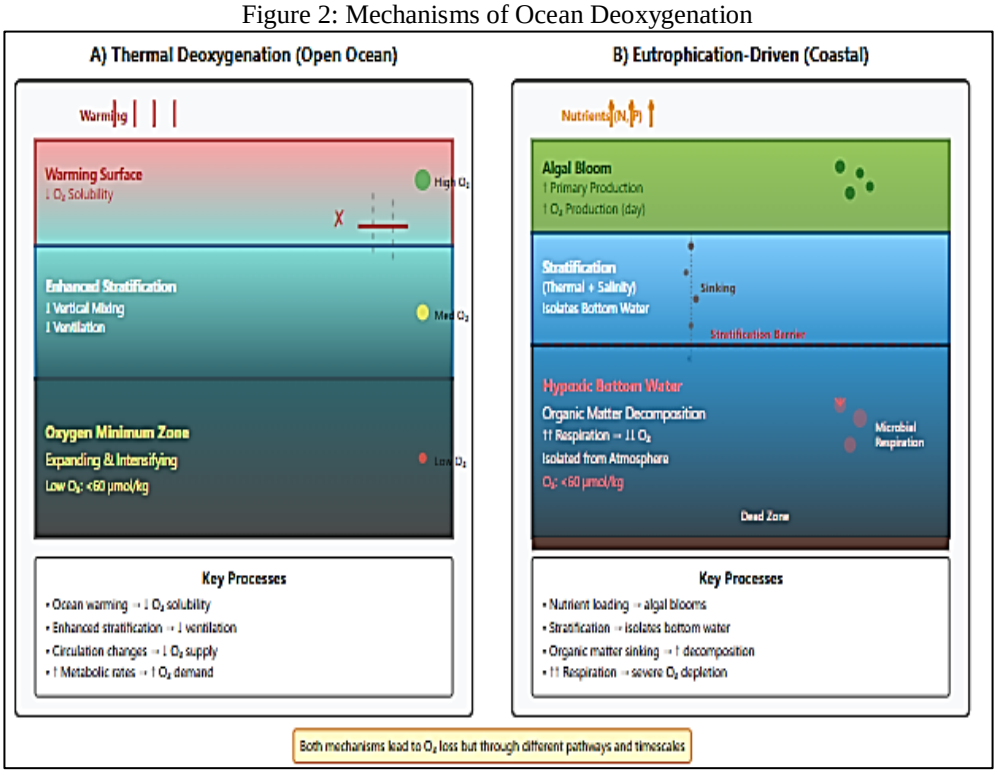

Figure 2 Shows Dual-panel conceptual diagram comparing thermal deoxygenation mechanism (left panel) and eutrophication-driven hypoxia mechanism (right panel). Each panel should show the key processes: for thermal - warming, stratification, reduced ventilation; for eutrophication - nutrient loading, algal bloom, organic matter decomposition, stratification. Use color gradients to indicate oxygen concentrations.

1.4. Synergistic Interactions

Thermal and eutrophication-driven deoxygenation interact synergistically, amplifying oxygen loss beyond additive effects[15]. Climate warming exacerbates eutrophication-driven hypoxia through earlier and stronger stratification extending hypoxic seasons, temperature-driven increases in metabolic rates enhancing consumption, altered precipitation affecting nutrient loading timing, and changes in phytoplankton community composition affecting organic matter quality. Regional manifestations vary: open ocean OMZs exhibit predominantly thermal mechanisms, coastal upwelling systems show natural low oxygen amplified by thermal trends, river-influenced systems demonstrate eutrophication dominance with warming modulation, and semi-enclosed seas experience strong synergistic effects.

III. CONSEQUENCES OF OCEAN DEOXYGENATION

3.1. Physiological and Organism-Level Impacts

Marine organisms experience progressive metabolic limitation as oxygen declines[16]. Critical oxygen thresholds vary widely, from <10 µmol/kg for tolerant invertebrates to >60 µmol/kg for active fishes and cephalopods. Sublethal hypoxia reduces aerobic scope, shifts metabolism toward less efficient anaerobic pathways, and alters energy allocation from growth and reproduction toward maintenance. Both hypoxia and reoxygenation induce oxidative stress through reactive oxygen species generation, potentially overwhelming antioxidant defenses[17]. The hypoxia-inducible factor pathway represents the primary molecular response, triggering transcriptional changes affecting metabolism, angiogenesis, and survival[18].

Meta-analyses demonstrate sublethal hypoxia significantly reduces growth rates and reproductive output across taxa[19]: reduced growth efficiency, delayed maturation, decreased fecundity and offspring quality, and disrupted reproductive timing. Mobile organisms exhibit behavioral modifications including migration to avoid low-oxygen waters, altered feeding, modified predator-prey interactions, and changed vertical migration patterns. Severe hypoxia (<20-30 µmol/kg) causes direct mortality through respiratory failure, with documented mass mortality events affecting fish, crustaceans, and benthic invertebrates.

3.2. Ecosystem Restructuring

Individual organism responses drive large-scale community and ecosystem changes. "Habitat compression" occurs as oxygen concentrations decline [20]: shoaling of upper OMZ boundaries restricts vertical habitat, compression increases vulnerability to surface fisheries, reduced thermal refuge eliminates escape from warm surface waters, and altered species co-occurrence patterns change community assembly. Analysis of fisheries data reveals billfishes, tunas, and large pelagic species increasingly avoid expanding low-oxygen waters, concentrating in surface layers experiencing thermal stress and increased fishing pressure.

Figure 3: Habitat Compression from Ocean Deoxygenation

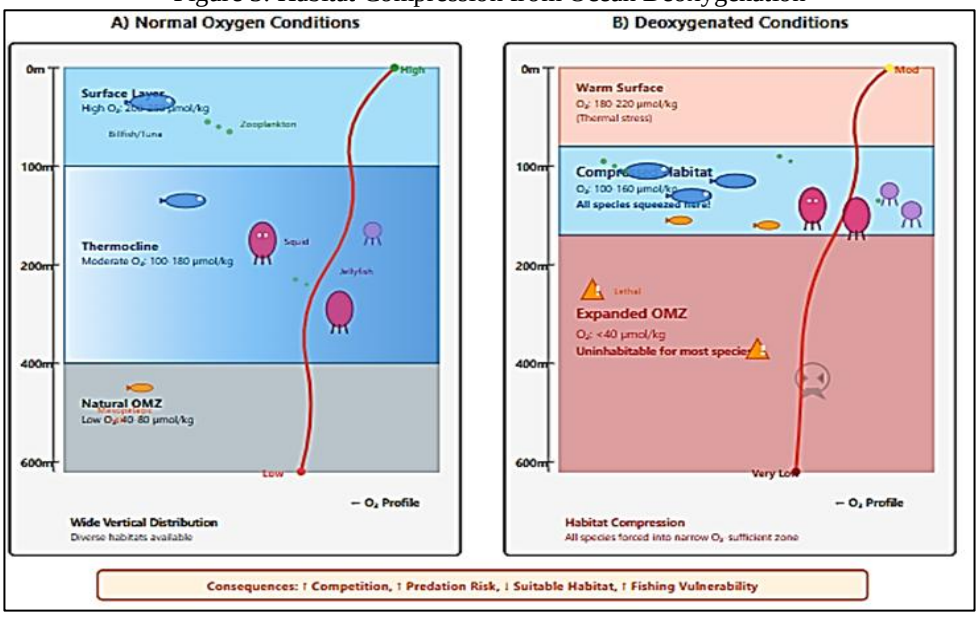

Figure 3 Shows Multi-panel diagram showing habitat compression in the water column. Panel A shows normal oxygen profile with vertical distribution of different taxa (fish, zooplankton, etc.). Panel B shows deoxygenated conditions with compressed habitats and species squeezed into narrower oxygen-sufficient zones. Use color coding for oxygen concentrations and silhouettes for different organisms.

Chronic hypoxia selects for tolerant species while eliminating sensitive taxa: reduced species richness and altered community structure, dominance by opportunistic hypoxia-tolerant species, loss of functional diversity, and modified size structure favoring smaller individuals with lower oxygen demands. In benthic communities, severe hypoxia eliminates macrofauna entirely, while moderate hypoxia shifts communities toward polychaete-dominated assemblages with reduced diversity. Trophic cascade effects propagate through food webs via altered predator-prey dynamics as spatial overlap changes, modified energy transfer efficiency between trophic levels, potential pelagic-benthic coupling decoupling, and shifts in dominant energy pathways.

3.3. Biogeochemical Consequences

Ocean deoxygenation fundamentally alters marine biogeochemical cycles with implications extending beyond direct ecological effects. The nitrogen cycle exhibits particular sensitivity to redox conditions[21]: enhanced denitrification in suboxic conditions removes bioavailable nitrogen, increased nitrous oxide (N_2O) production occurs in oxygen-depleted zones, altered nitrification-denitrification coupling affects nitrogen retention, and anammox zone expansion modifies nitrogen removal pathways. Expanding OMZs potentially increase oceanic N_2O emissions, creating positive feedback to climate warming.

Oxygen availability influences carbon cycling through multiple pathways: altered organic matter remineralization rates, modified biological pump efficiency, changed organic carbon export to deep ocean, and potential methane release from sediments under severe hypoxia. Redox-sensitive elements including iron, manganese, and phosphorus exhibit altered cycling[22]: enhanced phosphorus release from sediments fuels surface productivity, modified iron speciation affects phytoplankton nutrition, altered trace metal availability influences primary production patterns, and potential harmful algal bloom promotion through modified nutrient ratios. Bottom-water hypoxia dramatically alters sediment biogeochemistry through shifts from aerobic to anaerobic metabolic pathways, decreased bioturbation reducing oxygen penetration, modified organic matter preservation efficiency, and hydrogen sulfide release under severe conditions.

3.4. Socioeconomic Impacts

Deoxygenation translates into significant socioeconomic costs across multiple sectors. Fisheries experience impacts through reduced suitable habitat decreasing carrying capacity, habitat compression increasing catchability potentially leading to overharvest, sublethal effects reducing growth and reproductive output, shifts in species composition altering catch value, and increased uncertainty complicating stock assessment[23]. Economic analyses estimate potential losses of billions of dollars annually from hypoxia-related fisheries impacts in major systems.

Coastal hypoxia degrades multiple ecosystem services: biodiversity loss reduces ecosystem resilience and option value, degraded water quality impacts recreation and tourism, reduced nutrient cycling capacity affects system productivity, and loss of cultural values associated with healthy marine ecosystems. Severe hypoxia events damage infrastructure including desalination plant intake fouling, fish farm mortality, beach closures, and property value reductions. Total economic costs remain incompletely quantified but likely amount to tens of billions of dollars annually globally, with costs increasing as deoxygenation expands and intensifies.

IV. CONSERVATION AND MITIGATION STRATEGIES

4.1. Climate Change Mitigation

Addressing thermal deoxygenation fundamentally requires reducing greenhouse gas emissions to limit ocean warming and circulation changes, aligning with Paris Agreement objectives[24]. Modeling indicates achieving 1.5-2.0°C warming limits would substantially reduce but not eliminate thermal deoxygenation. Under high-emission scenarios (RCP8.5), global ocean oxygen could decline an additional 3-4% by 2100; under moderate mitigation (RCP4.5), approximately half this magnitude; even under aggressive mitigation (RCP2.6), some continued deoxygenation would occur due to thermal inertia. These projections emphasize critical importance of rapid, substantial emissions reductions.

Ocean-based climate solutions targeting ocean systems include ocean alkalinity enhancement, macroalgae cultivation for carbon sequestration, protection and restoration of blue carbon ecosystems (mangroves, seagrasses, salt marshes), and ocean iron fertilization (controversial due to uncertain effectiveness and side effects). Effectiveness, scalability, and potential unintended consequences require careful evaluation.

Blue carbon ecosystem restoration offers co-benefits for deoxygenation mitigation through localized nutrient uptake and enhanced oxygen production.

Given multi-decadal persistence of thermal deoxygenation due to ocean thermal inertia, adaptation strategies are necessary: spatial management adjusting marine protected area boundaries, fisheries management incorporating deoxygenation effects into assessments and harvest strategies, aquaculture siting accounting for projected oxygen trends, and early warning systems for severe events.

4.2. Nutrient Management for Coastal Hypoxia

Eutrophication-driven coastal hypoxia is theoretically amenable to relatively rapid mitigation through anthropogenic nutrient loading reduction, though implementation faces substantial technical, economic, and political challenges.

4.2.1. Agricultural Best Management Practices:

Agriculture represents the dominant nutrient source to many coastal systems[25]. Effective practices include precision agriculture using variable-rate fertilizer application, cover cropping and conservation tillage reducing runoff, riparian buffer strips intercepting nutrients, constructed wetlands treating agricultural drainage, and nitrogen management planning with timing and splitting applications. Strategic implementation achieves substantial nutrient reductions at reasonable cost, though full mitigation requires widespread adoption.

4.2.2. Wastewater Treatment Upgrades:

Urban wastewater represents geographically concentrated but significant nutrient sources: advanced nutrient removal technology in treatment plants, green infrastructure for stormwater management, septic system upgrades in sensitive watersheds, and combined sewer overflow control. Wastewater nutrient removal is generally more cost-effective than agricultural controls per-unit-nutrient, with regulations increasingly mandating upgrades.

4.2.3. Watershed-Scale Planning:

Effective nutrient management requires integrated approaches[26]: identification of critical source areas contributing disproportionate loads, targeting management efforts for maximum reduction per dollar, coordination across jurisdictional boundaries, and adaptive management incorporating monitoring to assess effectiveness.

4.2.4. Nature-Based Solutions:

Restoration of natural nutrient retention capacity offers multiple co-benefits: wetland restoration providing nutrient uptake and denitrification, riparian forest buffers for interception, oyster reef restoration enhancing filtration and removal, and seagrass restoration increasing oxygen production and nutrient sequestration.

Figure 4: Watershed Management for Nutrient Reduction

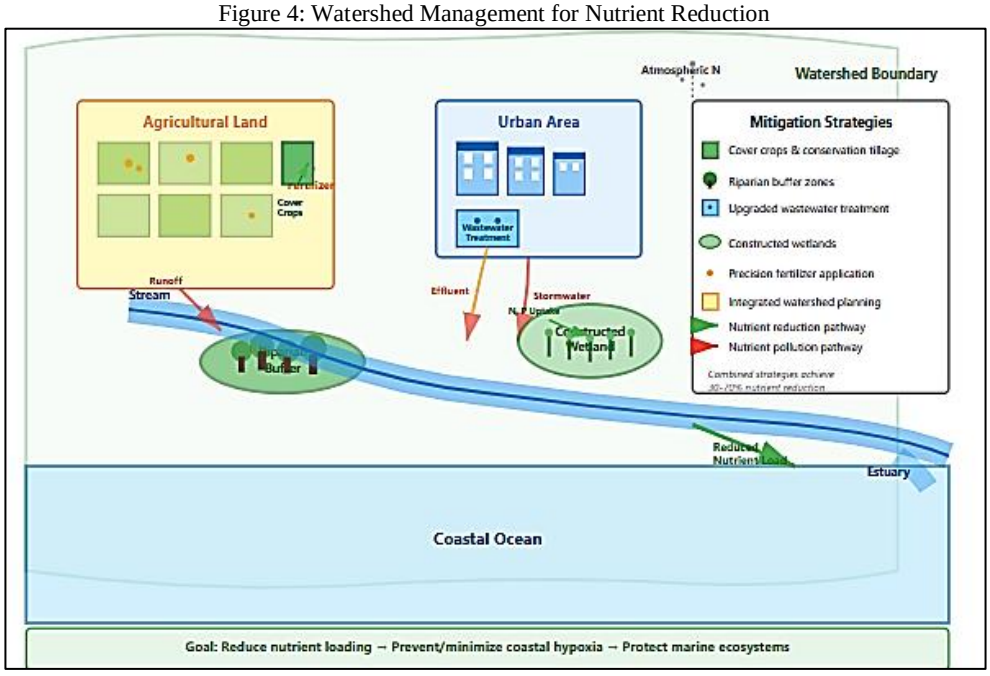

Figure 4 shows a Watershed management schematic showing different nutrient sources (agriculture, urban, atmospheric) and mitigation strategies (best management practices, wetlands, buffer zones, wastewater treatment). Include arrows showing nutrient pathways and reduction points. Use icons to represent different interventions.

4.3. Marine Spatial Planning and Monitoring

Strategic spatial management maintains refugia for oxygen-sensitive species and promotes ecosystem resilience. Dynamic management approaches include real-time management adjusting fishing closures based on observed oxygen, mobile protected areas tracking suitable habitat, seasonal closures timed to hypoxic periods, and adaptive boundaries responding to multi-year oxygen trends. Marine protected area networks should include naturally high-oxygen areas serving as climate refugia, connectivity planning accounting for oxygen-driven dispersal barriers, representation of diverse oxygen environments maintaining evolutionary potential, and buffer zones around protected areas accounting for oxygen variability.

Effective management requires robust monitoring to detect trends, trigger responses, and assess effectiveness[27]. Multiple platforms contribute to oxygen monitoring: fixed moorings providing high-temporal-resolution time series, profiling floats (Argo-Oxygen) enabling global subsurface monitoring, autonomous underwater vehicles conducting spatial surveys, Volunteer Observing Ships contributing opportunistic observations, and satellite remote sensing of surface conditions. Integration through data assimilation systems provides comprehensive monitoring capacity. Mechanistic models enable forecasting: seasonal hypoxia forecasts for coastal systems, climate model projections of long-term trends, short-term forecasts using real-time data assimilation, and machine learning approaches identifying predictive patterns.

4.4. Case Study Insights

Specific system implementations provide valuable lessons. Chesapeake Bay's 40+ year nutrient reduction effort achieved substantial loading decreases, yet hypoxia persists at significant levels[28]: legacy nutrients in sediments continue fueling hypoxia decades after reductions, climate warming offsets some benefits, agricultural sources prove particularly challenging to control, and sustained political and financial commitment is essential. The Baltic Sea's coordinated international action through the Helsinki Commission reduced nutrient loading, with recent improvement signs: long time lags between loading reductions and ecosystem response, importance of addressing all sources including atmospheric deposition, need for coordinated action across national jurisdictions, and value of integrated monitoring programs. Tampa Bay represents a success story where aggressive nutrient management substantially improved oxygen conditions: strict wastewater treatment requirements, seagrass restoration serving as indicator and driver, public-private partnerships in implementation, and adaptive management adjusting strategies based on monitoring.

These case studies highlight that while nutrient reduction can effectively mitigate coastal hypoxia, success requires sustained commitment, comprehensive approaches addressing all major sources, and realistic expectations regarding ecosystem recovery time frames.

V. INTEGRATED MANAGEMENT FRAMEWORK

5.1. Multi-Scale Action Framework

Effective response to ocean deoxygenation requires integration across spatial scales, temporal horizons, and governance levels. We propose a hierarchical framework recognizing distinct characteristics of thermal versus eutrophication-driven deoxygenation while addressing synergistic interactions.

5.1.1. Global Scale - Climate Mitigation:

At the largest scale, reducing greenhouse gas emissions remains the only effective approach to limiting thermal deoxygenation, requiring national commitments aligned with Paris Agreement targets, transition to renewable energy systems, carbon pricing mechanisms, and international cooperation. Timeline: Multi-decadal commitment required, with emissions reductions this decade critical for limiting mid- and late-century oxygen loss.

5.1.2. Regional Scale - Marine Spatial Planning:

Within large marine ecosystems and coastal seas: coordinated monitoring networks providing regional oxygen assessments, marine spatial plans incorporating deoxygenation projections, fisheries management adapting to changing oxygen conditions, and regional cooperation on nutrient management for shared water bodies. Timeline: Decades for full implementation, with adaptive management adjusting strategies based on observed trends.

5.1.3. Local Scale - Watershed and Coastal Management:

At individual estuary and coastal system scales: nutrient Total Maximum Daily Loads or equivalent frameworks, implementation of best management practices in watersheds, local habitat restoration enhancing resilience, and community engagement and stakeholder participation. Timeline: Years to decades for implementation, with monitoring tracking progress toward targets.

Figure 5 : Integrated Management Framework for Ocean Deoxygenation

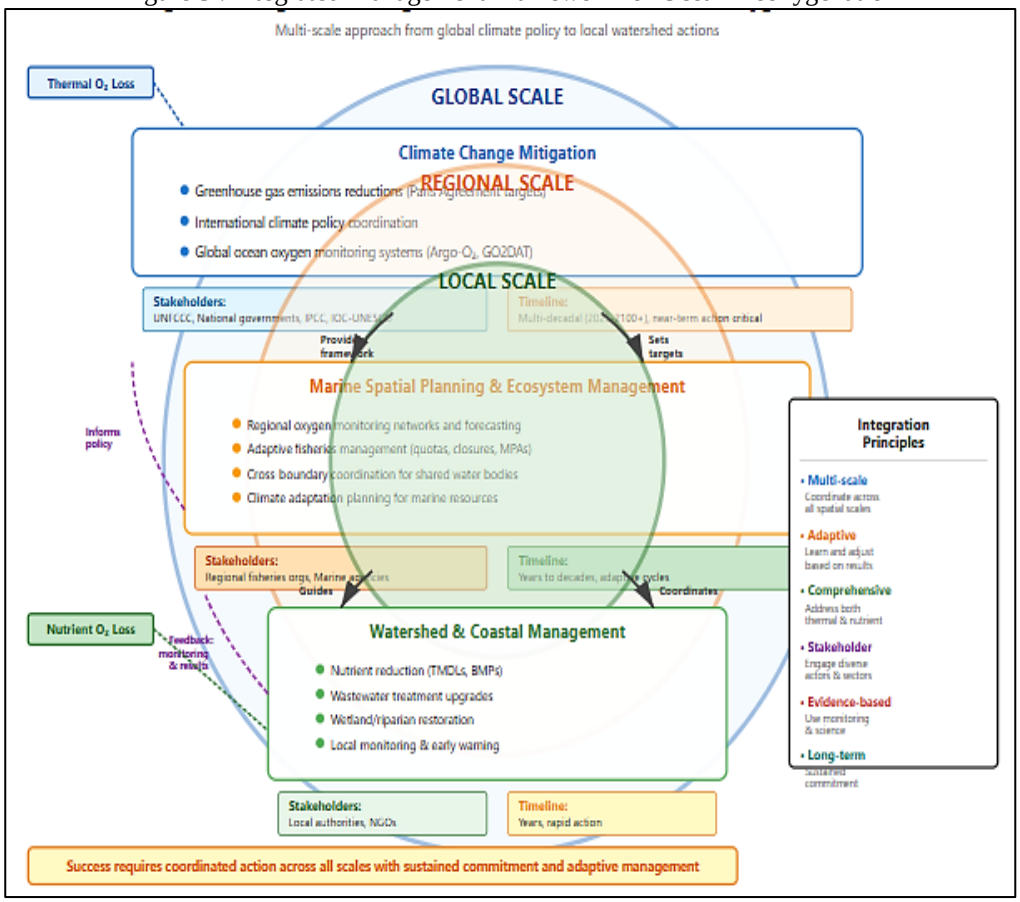

Figure 5 shows a Hierarchical framework diagram showing three nested scales (global, regional, local) with key actions, stakeholders, and timelines for each scale. Use concentric circles or nested boxes to show the relationship between scales, with specific strategies listed for each.

5.2. Priority Actions and Implementation

Based on analysis of deoxygenation mechanisms, consequences, and mitigation options, priority actions span multiple domains:

- Science and Monitoring: Expansion of global oxygen observing system particularly in under-sampled regions, enhanced process studies elucidating mechanistic drivers and threshold behaviors, improved modeling capabilities for prediction across scales, and synthesis activities integrating diverse data streams.
- Policy and Governance: Incorporation of ocean deoxygenation into climate policy frameworks, strengthening of nutrient management regulations and enforcement, development of adaptive management frameworks for marine resources, and international cooperation mechanisms for shared ocean regions.
- On-Ground Implementation: Deployment of best management practices in agricultural watersheds, wastewater treatment infrastructure upgrades, coastal habitat restoration projects, and fisher and aquaculture operator adaptation strategies.
- Capacity Building: Training programs for resource managers on deoxygenation assessment and response, public education on ocean health and individual actions, stakeholder engagement in collaborative management, and knowledge exchange between regions facing similar challenges.

5.3. Adaptive Management and Barriers

Given substantial uncertainties regarding deoxygenation trajectories, ecosystem responses, and management effectiveness, adaptive management approaches are essential[29]. Key elements include clear management objectives specifying measurable targets, systematic monitoring and assessment tracking oxygen trends and ecosystem status, predictive models forecasting consequences of management alternatives, regular learning and adjustment reviewing data to assess progress, and institutional structures enabling adaptive decision-making while maintaining long-term commitment.

Implementation faces multiple barriers. Economic and political barriers include costs concentrated on specific sectors while benefits diffuse, misalignment between political and ecological time scales, competing priorities for limited resources, and stakeholder resistance to regulations. Overcoming these requires economic instruments (payments for ecosystem services, nutrient trading), demonstration of co-benefits beyond deoxygenation mitigation, building political constituencies, and equitable distribution of costs and benefits.

Technical and knowledge barriers include uncertainties in projections and thresholds, gaps in understanding ecosystem responses, limited predictive capacity for management effectiveness, and data scarcity in many regions. Addressing these requires continued investment in research and monitoring, improved translation of science to management guidance, capacity building in data collection and analysis, and collaborative learning across regions.

Institutional and governance barriers include fragmentation of authority across jurisdictions and sectors, mismatch between ecological and governance boundaries, limited integration across air quality, water quality, and marine management, and insufficient coordination between local, regional, and global actions. Solutions include integrated governance frameworks spanning sectors and jurisdictions, formal coordination mechanisms, clear allocation of responsibilities and accountability, and flexibility to adjust governance as understanding improves.

VI. CONCLUSIONS AND RECOMMENDATIONS

Ocean deoxygenation represents a critical dimension of global change with profound implications for marine ecosystems, biogeochemical cycles, and human societies. The phenomenon results from both climate warming at global scales and nutrient pollution in coastal systems, with synergistic interactions amplifying oxygen loss. Consequences cascade from molecular responses through ecosystem restructuring to socioeconomic impacts worth billions of dollars annually.

Key findings include:

- Multiple interacting drivers operate through thermal effects globally and nutrient pollution in coastal systems, with synergistic amplification;
- Multi-scale consequences span cellular to ecosystem levels with significant socioeconomic costs; (3) Differentiated solutions require climate mitigation for thermal deoxygenation and nutrient management for eutrophication-driven hypoxia;
- Multi-decadal time scales for both deoxygenation evolution and response to mitigation require sustained commitment;
- Implementation challenges often exceed purely technical obstacles.

Critical research priorities include: quantification of thermal versus eutrophication contributions in regions experiencing both, mechanisms and thresholds for non-linear responses, improved Earth System Model representation of oxygen dynamics, rigorous evaluation of nutrient management strategy effectiveness, and cost-benefit analyses of alternative intervention strategies.

Policy recommendations include: explicit incorporation of ocean deoxygenation into National Determined Contributions and climate assessments, mandatory oxygen monitoring in areas at risk, integration of deoxygenation projections into marine spatial planning, enforceable nutrient reduction targets based on Total Maximum Daily Load approaches, improved integration across climate, water quality, and marine resource management institutions, and support for long-term monitoring programs essential for adaptive management.

The integrated framework presented here provides actionable guidance while identifying critical research priorities. Success requires unprecedented coordination across disciplines, sectors, and jurisdictions, guided by robust science while accommodating inherent uncertainties. Ocean deoxygenation exemplifies complex, multi-scale Anthropocene challenges. Effective response demands comprehensive, sustained action recognizing multi-decadal persistence of oxygen debt in subsurface waters. The stakes are high: ocean ecosystems providing essential services to billions and harboring much of Earth's biodiversity. The time for action is now.

REFERENCES

1. Pörtner HO, Knust R. 2007. Climate change affects marine fishes through the oxygen limitation of thermal tolerance. *Science* 315(5808):95–97.
2. Schmidtko S, Stramma L, Visbeck M. 2017. Decline in global oceanic oxygen content during the past five decades. *Nature* 542(7641):335–339.
3. Breitburg D, et al. 2018. Declining oxygen in the global ocean and coastal waters. *Science* 359(6371):eaam7240.
4. Oschlies A, Brandt P, Stramma L, Schmidtko S. 2018. Drivers and mechanisms of ocean deoxygenation. *Nature Geoscience* 11(7):467–473.
5. Keeling RF, Körtzinger A, Gruber N. 2010. Ocean deoxygenation in a warming world. *Annual Review of Marine Science* 2:199–229.
6. Stramma L, Johnson GC, Sprintall J, Mohrholz V. 2008. Expanding oxygen-minimum zones in the tropical oceans. *Science* 320(5876):655–658.
7. Keeling RF, Garcia HE. 2002. The change in oceanic O_2 inventory associated with recent global warming. *Proceedings of the National Academy of Sciences USA* 99(12):7848–7853.
8. Hoegh-Guldberg O, Bruno JF. 2010. The impact of climate change on the world's marine ecosystems. *Science* 328(5985):1523–1528.
9. Caesar L, Rahmstorf S, Robinson A, Feulner G, Saba V. 2018. Observed fingerprint of a weakening Atlantic Ocean overturning circulation. *Nature* 556(7700):191–196.
10. Deutsch C, Ferrel A, Seibel B, Pörtner HO, Huey RB. 2015. Climate change tightens a metabolic constraint on marine habitats. *Science* 348(6239):1132–1135.
11. Ito T, Minobe S, Long MC, Deutsch C. 2017. Upper ocean O_2 trends: 1958–2015. *Geophysical Research Letters* 44(9):4214–4223.
12. Rabalais NN, Turner RE, Wiseman WJ Jr. 2002. Gulf of Mexico hypoxia, aka "The Dead Zone." *Annual Review of Ecology and Systematics* 33:235–263.
13. Galloway JN, et al. 2008. Transformation of the nitrogen cycle: recent trends, questions, and potential solutions. *Science* 320(5878):889–892.
14. Diaz RJ, Rosenberg R. 2008. Spreading dead zones and consequences for marine ecosystems. *Science* 321(5891):926–929.
15. Gobler EM, et al. 2018. Hypoxia and acidification in ocean ecosystems coupled with warming and nutrient pollution. *Science* 359(6371):eaan8714.
16. Seibel BA. 2011. Critical oxygen levels and metabolic suppression in oceanic oxygen minimum zones. *Journal of Experimental Biology* 214(2):326–336.
17. Semenza GL. 2011. Oxygen sensing, homeostasis, and disease. *New England Journal of Medicine* 365(6):537–547.
18. Wang GL, Semenza GL. 1993. General involvement of hypoxia-inducible factor 1 in transcriptional response to hypoxia. *Proceedings of the National Academy of Sciences USA* 90(9):4304–4308.
19. Levin LA, et al. 2009. Effects of natural and human-induced hypoxia on coastal benthos. *Biogeosciences* 6(10):2063–2098.
20. Stramma RK, et al. 2012. Expansion of oxygen minimum zones may reduce available habitat for tropical pelagic fishes. *Nature Climate Change* 2(1):33–37.
21. Codispoti LA. 2010. Interesting times for marine N_2O. *Science* 327(5971):1339–1340.
22. Slomp CP, Van Cappellen P. 2007. The global marine phosphorus cycle: sensitivity to oceanic circulation. *Biogeosciences* 4(2):155–171.
23. Brander KM. 2010. Impacts of climate change on fisheries. *Journal of Marine Systems* 79(3–4):389–402.
24. Long MC, Deutsch C, Ito T. 2016. Finding forced trends in oceanic oxygen. *Global Biogeochemical Cycles* 30(2):381–397.
25. Rabalais NN, et al. 2014. Eutrophication-driven deoxygenation in the coastal ocean. *Oceanography* 27(1):172–183.
26. Scavia D, et al. 2017. Ensemble modeling informs hypoxia management inthe northern Gulf of Mexico. *Proceedings of the National Academy of Sciences USA* 114(33):8823–8828.
27. Claustre H, et al. 2010. Guidelines towards an integrated ocean observation system for ecosystems and biogeochemical cycles. In: *Proceedings of OceanObs'09: Sustained Ocean Observations and Information for Society*. Vol. 1. ESA Publication WPP-306.
28. Kemp WM, et al. 2005. Eutrophication of Chesapeake Bay: historical trends and ecological interactions. *Marine Ecology Progress Series* 303:1–29.
29. Folke C, et al. 2005. Adaptive governance of social-ecological systems. *Annual Review of Environment and Resources* 30:441–473.

INTERNATIONAL JOURNAL OF PURE SCIENCE RESEARCH STUDIES (IJPSRS)
(Open Access, Double-Blind Peer Reviewed Journal)
ISSN Online: ISSN Print
EDU SCHOOL
ijpsrs.com

Elliptic Curve Cryptography and the Discrete Logarithm Problem: An Algebraic Perspective

Renjith Varghese

Research Scholar, Department of Mathematics, St. Thomas College (Autonomous), Thrissur, India

Article information
Received: 2th August 2025
Received in revised form: 10th September 2025
Accepted: 17th October 2025
Available online: 14th November 2025

Volume:1
Issue:1
DOI: https://doi.org/10.5281/zenodo.17670077

Abstract

Elliptic Curve Cryptography (ECC) has emerged as a cornerstone of modern cryptographic systems, offering security levels comparable to traditional public-key cryptosystems with significantly reduced key sizes. This paper provides a comprehensive algebraic analysis of ECC, focusing on the mathematical foundations underlying the Elliptic Curve Discrete Logarithm Problem (ECDLP). We examine the group-theoretic properties of elliptic curves over finite fields, analyze the computational complexity of the discrete logarithm problem in this context, and evaluate current algorithmic approaches for solving ECDLP. The study presents a rigorous mathematical framework encompassing Weierstrass equations, point addition operations, scalar multiplication, and the algebraic structures that render ECDLP computationally intractable. We further investigate state-of-the-art attack methodologies including Pollard's rho algorithm, Baby-step Giant-step, and index calculus variants, demonstrating why ECC maintains its security advantage. The analysis concludes with implications for cryptographic protocol design and future directions in post-quantum cryptographic research. Our findings reinforce the robustness of ECC as a foundational technology for secure communication systems while identifying theoretical vulnerabilities that merit continued scrutiny.

Keywords: Elliptic Curve Cryptography, Discrete Logarithm Problem, Finite Fields, Group Theory, Cryptanalysis, Algebraic Geometry

I. INTRODUCTION

1.1. Motivation and Context

The exponential growth of digital communication systems and the proliferation of internet-connected devices have elevated cryptographic security from a specialized concern to a fundamental infrastructure requirement. Public-key cryptography, pioneered by Diffie and Hellman in 1976 and subsequently instantiated through RSA by Rivest, Shamir, and Adleman in 1977, established the paradigm for secure key exchange and digital signatures in open networks. However, the computational overhead and key size requirements of traditional public-key systems have motivated research into more efficient alternatives.

Elliptic Curve Cryptography, independently proposed by Neal Koblitz and Victor Miller in 1985, represents a fundamental shift in cryptographic methodology. By leveraging the algebraic structure of elliptic curves over finite fields, ECC achieves equivalent security to RSA with dramatically smaller key sizes—a 256-bit ECC key provides security comparable to a 3072-bit RSA key. This efficiency advantage translates directly into reduced computational requirements, lower power consumption, and decreased bandwidth utilization, making ECC particularly attractive for resource-constrained environments including mobile devices, embedded systems, and Internet of Things (IoT) applications.

1.2. The Discrete Logarithm Problem

The security of ECC fundamentally depends on the computational intractability of the Elliptic Curve Discrete Logarithm Problem. Given an elliptic curve E defined over a finite field F_q, a point P ∈ E (F_q) of order n, and another point Q ∈ ⟨P⟩ (the cyclic subgroup generated by P), the ECDLP requires finding the integer k ∈ [0, n-1] such that Q = kP, where kP denotes k-fold scalar multiplication of P.

The discrete logarithm problem in multiplicative groups of finite fields has been extensively studied since the inception of public-key cryptography. However, the ECDLP exhibits distinct characteristics that significantly impact its computational complexity. Unlike the classical DLP in (F_q)*, where sub-exponential algorithms such as the Number Field Sieve achieve complexity $O(exp((64/9)^{1/3}\ \ (logq)^{1/3}\ \ (loglogq)^{2/3}))$ the ECDLP resists such approaches due to the absence of a smooth homomorphism from the elliptic curve group to a more tractable algebraic structure.

1.3. Research Objectives and Contributions

This paper provides a comprehensive algebraic analysis of ECC and ECDLP with the following specific objectives:

- Establish rigorous mathematical foundations: We develop the complete algebraic framework for elliptic curves over finite fields, including detailed derivations of group operations and structural properties.
- Analyze computational complexity: We present a thorough examination of ECDLP complexity, demonstrating why current best algorithms require exponential time and establishing concrete security parameters.
- Evaluate cryptanalytic approaches: We systematically analyze existing algorithms for solving ECDLP, including generic algorithms applicable to arbitrary groups and specialized methods exploiting elliptic curve properties.
- Assess cryptographic implications: We examine how the algebraic properties of elliptic curves translate into practical security guarantees for cryptographic protocols.
- Identify research directions: We outline theoretical challenges and emerging threats, particularly from quantum computing, that will shape future cryptographic research.

1.4. Paper Organization

The remainder of this paper is structured as follows: Section II provides comprehensive background on elliptic curves, establishing the mathematical foundations necessary for subsequent analysis. Section III develops the algebraic theory of elliptic curves over finite fields, including group structure and point operations. Section IV presents a detailed examination of the ECDLP and its computational complexity. Section V analyzes algorithmic approaches for solving ECDLP. Section VI discusses cryptographic applications and protocol implementations. Section VII concludes with implications and future research directions.

II. MATHEMATICAL FOUNDATIONS

2.1. Elliptic Curves: Algebraic Definition

An elliptic curve E over a field K is the set of solutions (x, y) ∈ K × K to a generalized Weierstrass equation:

$$E: y^2 + a_1xy + a_3y = x^3 + a_2x^2 + a_4x + a_6$$

where $a_1, a_2, a_3, a_4, a_6 \in K$, together with a distinguished point O called the point at infinity. The curve must be non-singular, meaning it has no cusps or self-intersections. Formally, this non-singularity condition requires that the discriminant $\Delta \neq 0$.

For cryptographic applications, we typically work with elliptic curves over finite fields F_p (where p is a large prime) or F_2^m (binary fields). In the prime field case with characteristic p > 3, the Weierstrass equation simplifies to the short Weierstrass form:

$$E: y^2 = x^3 + ax + b$$

where a, b ∈ F_p and the discriminant condition becomes $4a^3 + 27b^2 \neq 0 \pmod p$.

Figure 1: Elliptic Curve Point Addition

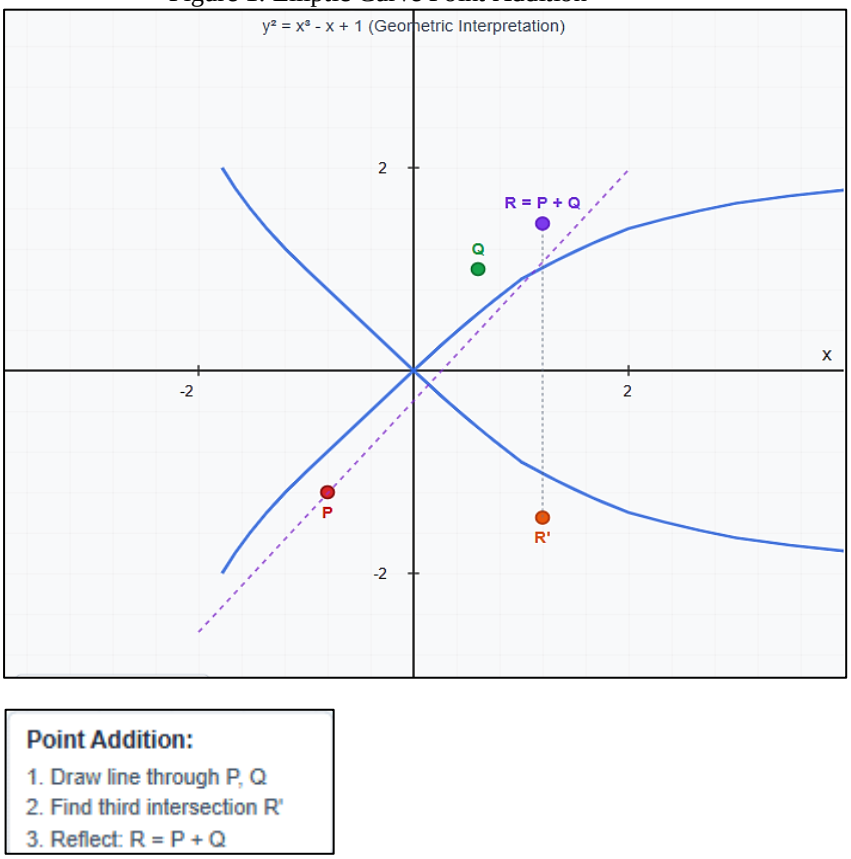

Figure 1 **:** Elliptic curve visualization showing the geometric structure of $y^2 = x^3 - x + 1$ over real numbers, illustrating the characteristic symmetric shape and point addition using the chord-and-tangent method

2.2. Group Structure on Elliptic Curves.

The set of points E(K) on an elliptic curve forms an abelian group under a geometric addition operation. For points $P = (x_1, y_1)$ and $Q = (x_2, y_2)$ on E, the sum $R = P + Q = (x_3, y_3)$ is defined through the following algebraic formulas:

2.2.1. Point Addition ($P \neq Q$):

If $x_1 \neq x_2$, the slope of the line through P and Q is: $\lambda = (y_2 - y_1) / (x_2 - x_1)$

$$\text{Then: } x_3 = \lambda^2 - x_1 - x_2 \; y_3 = \lambda(x_1 - x_3) - y_1$$

2.2.2. Point Doubling ($P = Q$):

For P = Q, where P has non-zero y-coordinate: $\lambda = (3x_1^2 + a) / (2y_1)$

$$\text{Then: } x_3 = \lambda^2 - 2x_1 \; y_3 = \lambda(x_1 - x_3) - y_1$$

2.2.3. Identity Element:

The point at infinity O serves as the identity element: $P + O = O + P = P$ for all $P \in E(K)$.

2.2.4. Inverse Element:

For P = (x, y), the inverse is -P = (x, -y), satisfying $P + (-P) = O$.

This group law satisfies all group axioms:

- Closure: For all $P, Q \in E(K)$, $P + Q \in E(K)$
- Associativity: $(P + Q) + R = P + (Q + R)$
- Identity: $O + P = P + O = P$
- Inverse: $P + (-P) = O$

The commutativity property P + Q = Q + P makes E(K) an abelian group, which is fundamental to the cryptographic properties we exploit.

2.3. Finite Field Arithmetic

Elliptic curve cryptography operates over finite fields to ensure computational feasibility and cryptographic security. The two primary finite field types used in ECC are:

2.3.1. Prime Fields F_P

These fields consist of integers modulo a large prime p. Arithmetic operations are performed modulo p:

- Addition: (a + b) mod p
- Multiplication: (a × b) mod p
- Inversion: a^{-1} such that $a \times a^{-1} \equiv 1 \pmod p$, computed via the Extended Euclidean Algorithm

2.3.2. Binary Fields F_2^m:

These fields consist of polynomials of degree less than m with binary coefficients, with arithmetic performed modulo an irreducible polynomial f(x) of degree m. Operations include:

- Addition: XOR operation
- Multiplication: Polynomial multiplication modulo f(x)
- Inversion: Extended Euclidean Algorithm for polynomials

The choice between prime and binary fields involves trade-offs between implementation efficiency and security considerations. Prime fields generally offer simpler theoretical analysis, while binary fields may provide implementation advantages in hardware.

2.4. Scalar Multiplication

Scalar multiplication is the fundamental operation in ECC, defined as repeated addition:

$$kP = P + P + ... + P \text{ (k times)}$$

For cryptographic applications, efficient computation of kP is essential. The binary method (double-and-add algorithm) computes kP in O(log k) point operations:

2.4.1. Algorithm 1: Binary Method for Scalar Multiplication

Input: k, P
Output: Q = kP

1. Write k in binary: $k = (k_t, k_{\{t-1\}}, ..., k_1, k_0)_2$
2. Q ← O
3. For i from t down to 0:
    a. Q ← 2Q
    b. If $k_i = 1$ then Q ← Q + P
4. Return Q

More sophisticated methods such as Non-Adjacent Form (NAF) representation and windowing techniques further optimize scalar multiplication, reducing the expected number of point additions by approximately 33% compared to the standard binary method.

III. ELLIPTIC CURVES OVER FINITE FIELDS

3.1. Point Counting and Group Order

The number of points on an elliptic curve E over F_q, denoted #E $(F_q)\cong$, is fundamental to cryptographic security. Hasse's theorem provides tight bounds on this value:

$$q + 1 - 2\sqrt{q} \leq \#E\ (F_q) \leq q + 1 + 2\sqrt{q}$$

The precise value can be computed using Schoof's algorithm, which runs in polynomial time $O((\log q)^8)$, and improved variants by Elkies and Atkin achieving $O((\log q)^4)$ complexity.

For cryptographic purposes, we require #E (F_q) to have a large prime factor n, typically satisfying

#E (F_q)= hn where h (the cofactor) is small and n is a large prime. The subgroup of order n then provides the cryptographic group in which ECDLP must be solved.

Figure 2: Hasse's Theorem - Group Order Distribution

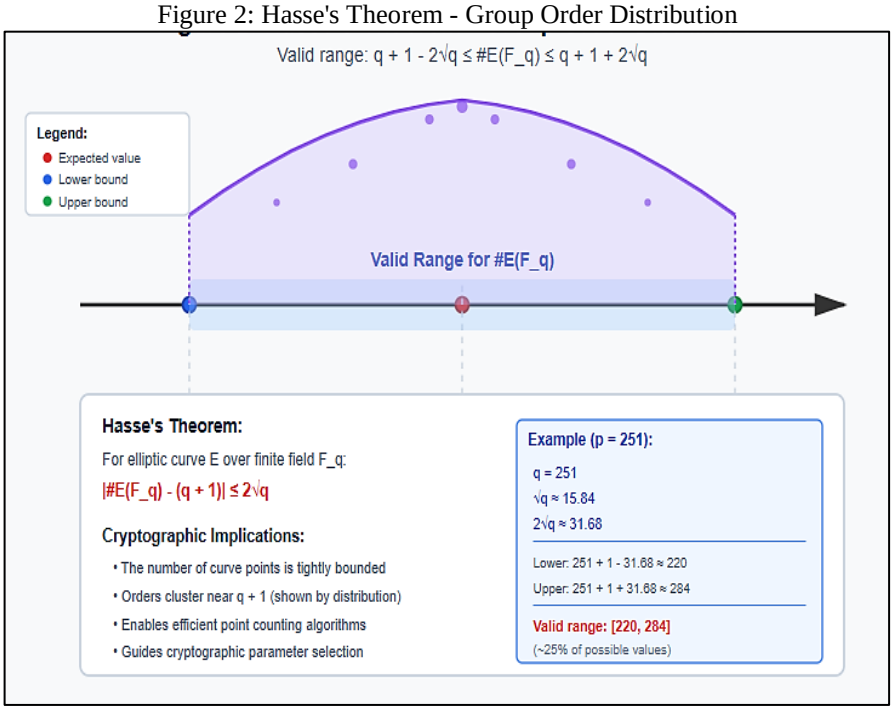

Figure 2 Schematic diagram illustrating the distribution of group orders for elliptic curves over F_p, showing how Hasse's theorem constrains possible values

3.2. Cyclic Subgroups and Generators

By Lagrange's theorem, the order of any point P divides #E(F_q). For cryptographic applications, we work within a cyclic subgroup G = ⟨P⟩ of prime order n, generated by a carefully chosen base point P.

The structure theorem for abelian groups guarantees that:

$$E(F_q) \cong Z_{n1} \times Z_{n2}$$

where n_2 divides both n_1 and q - 1. For cryptographically strong curves, we typically have #E(F_q)≅ = n (prime) or #E(F_q)≅ = 2n, 4n, 8n with n prime.

3.3. Embedding Degree and Complex Multiplication

The embedding degree k of an elliptic curve E over F_q with respect to a prime n dividing #E(F_q) is the smallest positive integer such that n q^{k-1} .This parameter determines the security against pairing-based attacks, as it defines the smallest extension field F_k^q into which E can be embedded while preserving the group structure.

For cryptographic security, we require k to be sufficiently large. Curves with small embedding degree are vulnerable to the MOV attack, which reduces ECDLP to DLP in F_k^q where sub-exponential algorithms apply.

Complex multiplication (CM) theory provides a method for constructing elliptic curves with prescribed group orders. Given a discriminant D, CM theory allows construction of curves over $F_p$with specific cryptographic properties, including resistance to known attacks and optimal efficiency for implementation.

3.4. Endomorphism Ring and Frobenius Map

The endomorphism ring End(E) of an elliptic curve consists of all rational maps E → E that preserve the group structure and the point at infinity. For ordinary curves over F_q, End(E) is isomorphic to an order in an imaginary quadratic field.

The Frobenius endomorphism φ_q: E → E defined by φ_q(x, y) = $x^q y^q$ plays a central role in the arithmetic of elliptic curves over finite fields. The Frobenius satisfies the characteristic equation:

$$\Psi_p^2 - t\Psi_q + q = 0$$

where t = q + 1 - #E(F_q) is the trace of Frobenius, with |t| ≤ 2√q by Hasse's theorem.

Understanding the endomorphism ring structure is crucial for assessing security, as certain endomorphisms can be exploited to accelerate cryptanalytic attacks. For instance, curves over F_{p^2} with efficiently computable endomorphisms are vulnerable to the GHS attack.

IV. THE ELLIPTIC CURVE DISCRETE LOGARITHM PROBLEM

4.1. Problem Formulation and Hardness

Definition 1 (ECDLP): Let E be an elliptic curve defined over a finite field F_q, let P ∈ E(F_q) be a point of prime order n, and let Q ∈ ⟨P⟩. The Elliptic Curve Discrete Logarithm Problem is to determine the unique integer k ∈ [0, n-1] such that Q = kP.

The computational hardness of ECDLP forms the foundation of ECC security. Unlike the classical discrete logarithm problem in multiplicative groups F_p*,, no sub-exponential algorithm is known for solving ECDLP on properly chosen elliptic curves. This asymmetry in computational complexity—easy to compute kP given k and P, but hard to recover k given P and kP—provides the one-way function property essential for public-key cryptography.

Figure 3: The Elliptic Curve Discrete Logarithm Problem

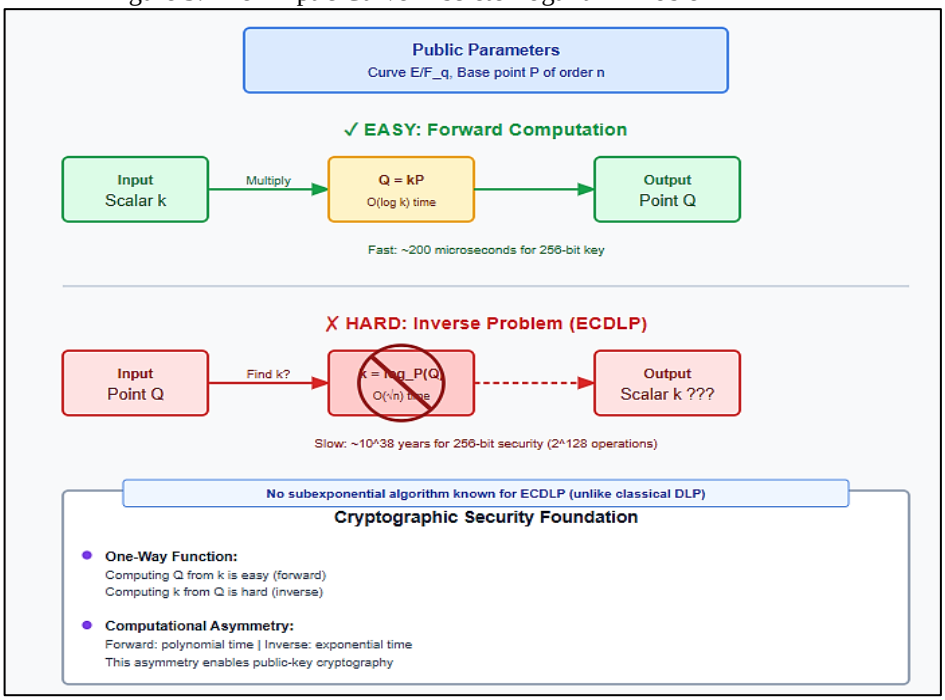

Figure 3: Flowchart illustrating the ECDLP: given base point P and target point Q = kP, the challenge of computing k despite efficient scalar multiplication

4.2. Complexity-Theoretic Analysis

The best known generic algorithms for solving ECDLP require O(√n) group operations, where n is the the order of the base point P. This exponential complexity in the bit length of n (approximately $O(2^{(log_2 n)\backslash 2})$) contrasts sharply with index calculus methods for the classical DLP, which achieve sub-exponential complexity.

The square-root complexity bound arises from the birthday paradox: in a group of order n, approximately √n random elements are required before a collision occurs with high probability. Both Pollard's rho and Baby-step Giant-step algorithms exploit this fundamental property.

For a security level of λ bits, we require n ≈ $2^{2\lambda}$ meaning a 256-bit elliptic curve provides 128-bit security. Current cryptographic standards recommend:

- 224-bit curves for 112-bit security
- 256-bit curves for 128-bit security
- 384-bit curves for 192-bit security
- 521-bit curves for 256-bit security

4.3. Reduction to Other Problems

ECDLP exhibits interesting relationships with other computational problems:

4.3.1. Relation to Computational Diffie-Hellman (CDH):

The CDH problem—given P, aP, bP, compute abP—is polynomial-time reducible to ECDLP. If ECDLP can be solved efficiently, CDH becomes trivial. However, the converse reduction is unknown, and CDH may be strictly easier than ECDLP.

4.3.2. Relation to Decisional Diffie-Hellman (DDH):

The DDH problem—given P, aP, bP, cP, decide if c = ab—is believed to be easier than CDH. On elliptic curves with efficiently computable pairings, DDH is easy due to bilinear maps, but ECDLP and CDH remain hard.

4.3.3. Relation to Inverse Problems:

The elliptic curve inverse problem—given P and kP, compute $k^{-1}P$ (where k^{-1} is the multiplicative inverse mod n)—is equivalent to ECDLP, as solving either immediately yields a solution to the other.

4.4. Weak Curve Classes

Certain elliptic curve configurations are vulnerable to attacks that reduce ECDLP to easier problems:

4.4.1. Supersingular Curves:

Curves with trace of Frobenius t = 0 have small embedding degree ($k \leq 6$), making them vulnerable to MOV/Frey-Rück attacks that transfer ECDLP to DLP in small extension fields.

4.4.2. Anomalous Curves:

Curves over F_p with exactly p points (#E F_p = p) are vulnerable to the Semaev-Smart-Satoh-Araki (SSSA) attack, which solves ECDLP in polynomial time using p-adic lifting techniques.

4.4.3. Curves with Small Embedding Degree:

If the embedding degree k is small relative to log q, pairing-based attacks reduce ECDLP to DLP in, F_q^k where index calculus methods may be applicable.

4.4.4. Curves Over F_2^m with Efficiently Computable Isogenies:

The GHS attack exploits efficiently computable isogenies to map ECDLP instances to hyperelliptic curves where index calculus variants are more effective.

Cryptographic standards explicitly prohibit these weak curve classes, requiring careful parameter selection during curve generation.

V. CRYPTANALYTIC ALGORITHMS

5.1. Generic Algorithms

Generic algorithms solve the discrete logarithm problem without exploiting specific properties of the group structure, making them applicable to ECDLP on any elliptic curve.

5.1.1. Baby-step Giant-step Algorithm:

Shanks' algorithm uses a meet-in-the-middle approach:

Algorithm 2: Baby-step Giant-step

Input: P, Q, n (where Q = kP for unknown k < n)

Output: k

1. m ← ⌈√n⌉
2. Compute baby steps: Store (iP, i) for i = 0, 1, ..., m-1
3. Compute mP
4. For j = 0, 1, ..., m-1:
   a. Compute Q - j(mP)
   b. If Q - j(mP) = iP for some stored baby step:
      Return k = i + jm

Time complexity: O(√n) group operations Space complexity: O(√n) group elements

5.1.2. Pollard's Rho Algorithm:

Pollard's rho uses pseudorandom walks to find collisions with minimal storage:

Algorithm 3: Pollard's Rho

Input: P, Q, n (where Q = kP)

Output: k

1. Define partition function f: G → G using random-walk steps
2. Initialize: $x_0 \leftarrow P$, $y_0 \leftarrow P$
3. Repeat:
   a. $x_{\{i+1\}} \leftarrow f(x_i)$
   b. $y_{\{i+1\}} \leftarrow f(f(y_i))$
   c. If $x_i = y_i$,collision found
4. Solve for k from collision relation

Time complexity: O(√n) expected group operations Space complexity: O(1) (constant storage)

The parallel version of Pollard's rho achieves near-linear speedup with multiple processors, making it the most practical generic attack for large-scale cryptanalysis.

Figure 4: Pollard's Rho Algorithm for ECDLP

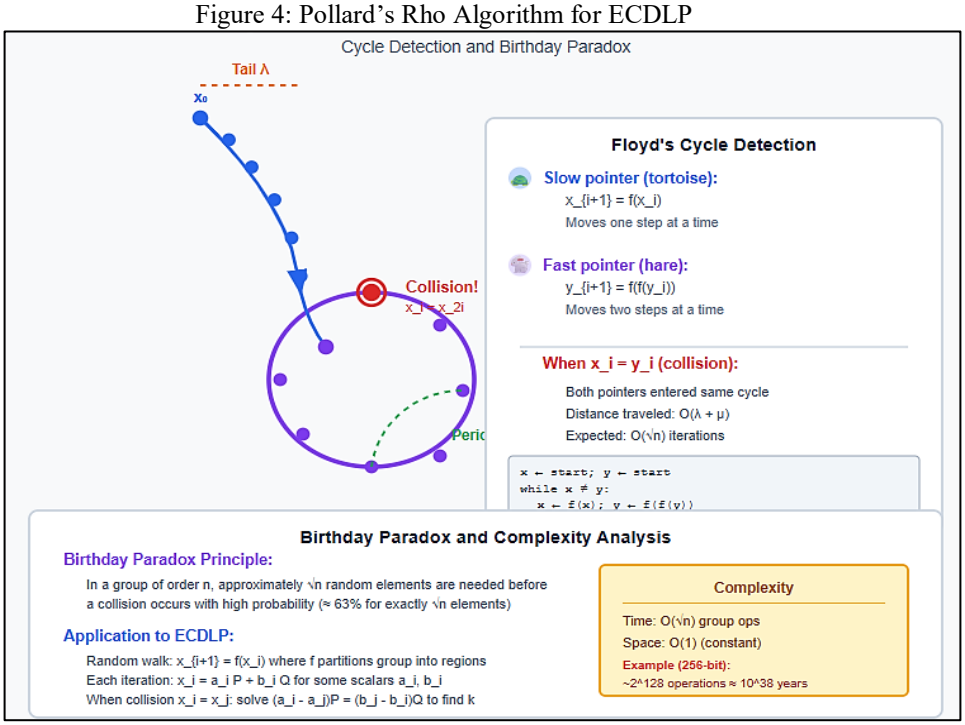

Figure 4 **:**Visualization of Pollard's rho algorithm showing the "rho-shaped" trajectory and cycle detection using Floyd's cycle-finding algorithm

5.2. Index Calculus Attempts

Index calculus has been extraordinarily successful for classical DLP in F_p^*, achieving $L_p[1/3]$ complexity. However, attempts to adapt this approach to elliptic curves have largely failed due to fundamental structural obstacles.

5.2.1 Classical Index Calculus (for reference):

The method relies on:

- Defining a factor base of "small" elements
- Finding relations among factor base elements
- Solving a sparse linear system
- Computing individual logarithms

5.2.2. Why Index Calculus Fails for ECDLP:

The critical obstacle is the absence of a natural notion of "small" or "smooth" points on elliptic curves. Unlike integers, which decompose into prime factors, elliptic curve points lack a canonical factorization structure. The group operation on $E(F_q)$ does not admit a smooth element base amenable to relation collection.

5.2.3. Gaudry's Index Calculus for Hyperelliptic Curves:

For hyperelliptic curves of genus $g \geq 3$ over small characteristic fields, Gaudry developed an index calculus variant with complexity O(q^(2-2/g)). However, this approach does not extend effectively to genus 1 curves (elliptic curves) with large q.

5.3. Specialized Attacks

5.3.1. MOV/Frey-Rück Attack:

For curves with small embedding degree k, the Weil or Tate pairing provides an efficiently computable homomorphism:

$$e: E(F_q)[n] \times E((F_{q^k})[n] \rightarrow F^*_{q^k}$$

Given Q = kP, we can compute:

$$e(Q, R) = e(kP, R) = e(P, R)^k$$

Solving DLP in F_q^k* yields k, reducing ECDLP to classical DLP. This attack is polynomial-time when k = O(log q).

5.3.2. SSSA Attack on Anomalous Curves:

For curves over F_p with #E(F_p) = p, the attack uses p-adic lifting:

Given Q = kP, lift points to E(Q_p) (curve over p-adic numbers). The formal group logarithm provides a group isomorphism:

$$\log: E_1(pZ_p) \rightarrow pZ_p$$

Computing logarithms modulo increasingly high powers of p eventually recovers k in polynomial time.

5.3.3. GHS Attack:

For certain curves over F_2^m, the GHS attack constructs a covering curve C (typically hyperelliptic) over a subfield such that ECDLP on E(F_2^m) reduces to DLP on the Jacobian of C, where index calculus variants may apply.

5.3.4. Fault Analysis and Side-Channel Attacks:

While not directly solving ECDLP, implementation attacks exploit physical characteristics:

- Timing attacks: Measuring computation time to infer secret bits
- Power analysis: Analyzing power consumption during scalar multiplication
- Fault injection: Inducing computational errors to reveal information

Countermeasures include constant-time implementations, point randomization, and anomaly detection.

5.4. Quantum Algorithms

Shor's quantum algorithm fundamentally threatens ECDLP security. Given a quantum computer with

sufficient qubits and coherence time, Shor's algorithm solves ECDLP in polynomial time $O((\log n)^3)$ using quantum Fourier transforms.

5.4.1. Shor's Algorithm for ECDLP:

- Prepare quantum superposition over scalars k
- Apply quantum scalar multiplication: $|k\rangle|0\rangle \rightarrow |k\rangle|kP\rangle$
- Quantum Fourier Transform on the first register
- Measure to obtain information about the order
- Classical post-processing recovers discrete logarithm

The algorithm requires O(log n) qubits and O((log n)³) quantum gates. Current quantum computers remain far from the scale required to threaten cryptographic instances (thousands of logical qubits after error correction), but the theoretical threat has motivated post-quantum cryptography research.

VI. CRYPTOGRAPHIC APPLICATIONS

6.1. Elliptic Curve Diffie-Hellman (ECDH)

ECDH extends the Diffie-Hellman key exchange protocol to elliptic curves:

6.1.1. Protocol:

- Public parameters: Elliptic curve E over F_q, base point P of prime order n
- Alice chooses private key a ∈ [1, n-1], computes public key A = aP
- Bob chooses private key b ∈ [1, n-1], computes public key B = bP
- Alice computes shared secret: $K_A = a(B) = abP$
- Bob computes shared secret: $K_B = b(A) = baP$
- Shared secret: $K = K_A = K_B$

Security relies on the computational Diffie-Hellman assumption: given P, aP, bP, computing abP is hard without knowing a or b.

Figure 5: Elliptic Curve Diffie-Hellman (ECDH) Key Exchange

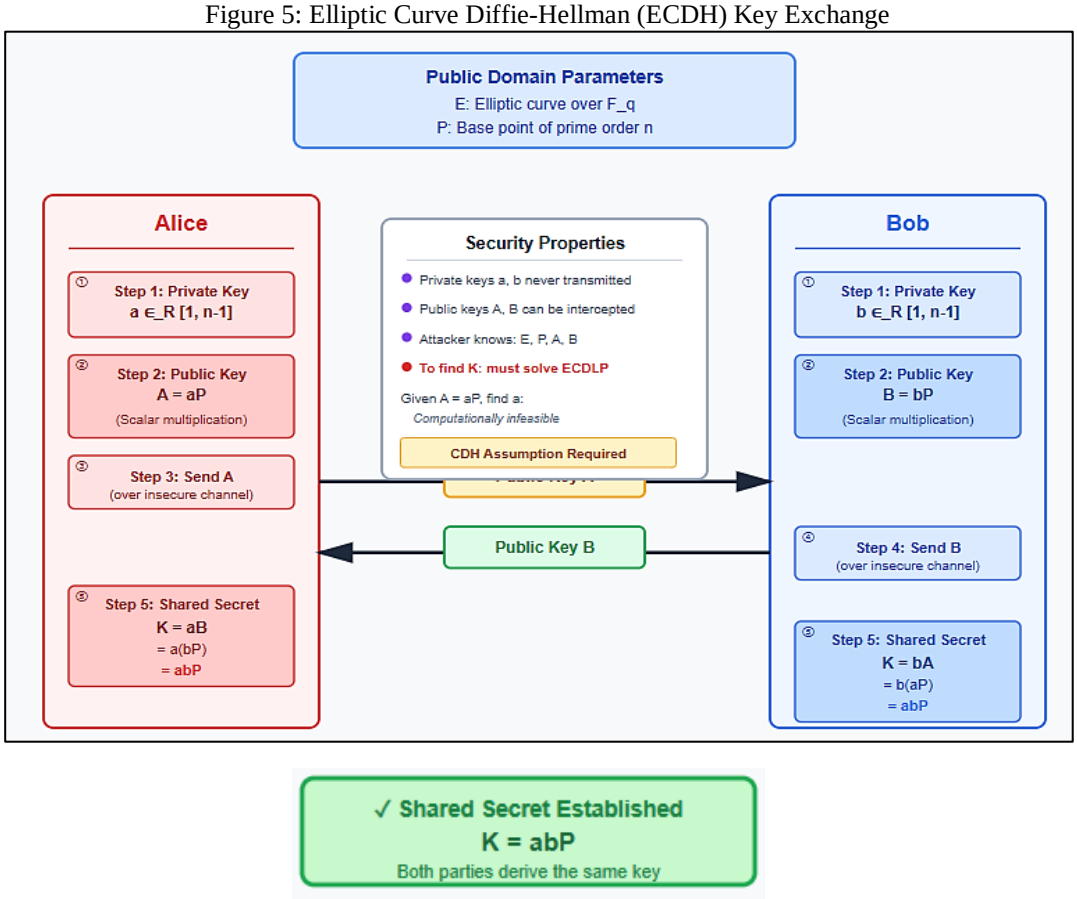

Figure 5 Protocol diagram illustrating ECDH key exchange between Alice and Bob, showing the flow of public key exchanges and shared secret computation

6.2. Elliptic Curve Digital Signature Algorithm (ECDSA)

ECDSA provides authentication and non-repudiation:

6.2.1. Signature Generation:

- Message m, private key d
- Hash h = H(m) where H is a cryptographic hash function
- Choose random k ∈ [1, n-1]

- Compute $(x_1, y_1) = kP$
- Compute $r = x_1 \bmod n$ (if $r = 0$, choose new k)
- Compute $s = k^{-1}(h + dr) \bmod n$ (if $s = 0$, choose new k)
- Signature: (r, s)

6.2.2. Signature Verification:

- Verify $r, s \in [1, n-1]$
- Compute $h = H(m)$
- Compute $u_1 = hs^{-1} \bmod n$, $u_2 = rs^{-1} \bmod n$
- Compute $(x_1, y_1) = u_1P + u_2Q$ (where $Q = dP$ is public key)
- Accept if $r \equiv x_1 \pmod n$

Security depends on both ECDLP hardness and hash function collision resistance. The randomness of k is critical—reusing k or using predictable k values completely breaks the scheme, as demonstrated by the 2010 PlayStation 3 signing key compromise.

6.3. Elliptic Curve Integrated Encryption Scheme (ECIES)

ECIES combines ECDH with symmetric encryption and MAC for public-key encryption:

6.3.1. Encryption (Alice encrypts to Bob):

- Generate ephemeral key pair (k, R = kP)
- Compute shared secret $S = k(Q_B)$ where Q_B is Bob's public key
- Derive encryption and MAC keys: $(K_E, K_M) = KDF(S)$
- Encrypt: $c = E_{K_E}(m)$
- Compute MAC: $MAC_{K_M}(c)$
- Ciphertext: (R, c, t)

6.3.2. Decryption (Bob decrypts):

- Compute S = d_B(R) using private key d_B
- Derive keys: $(K_E, K_M) = KDF(S)$
- Verify MAC: $MAC_{KM}(c) = t$
- Decrypt: $m = D_{K_E}(c)$

ECIES provides IND-CCA2 security under appropriate assumptions, making it suitable for general-purpose public-key encryption.

6.4. Performance Comparison

Table 1: Key Size Comparison:

Security Level	ECC (bits)	RSA (bits)	Ratio
80-bit	160	1024	1:6.4
112-bit	224	2048	1:9.1
128-bit	256	3072	1:12
192-bit	384	7680	1:20
256-bit	521	15360	1:29

6.4.1. Computational Performance:

On a modern processor (Intel Core i7, 3.4 GHz):

- ECDH key generation (P-256): ~0.8 ms
- ECDH shared secret: ~0.8 ms
- ECDSA signing (P-256): ~1.2 ms
- ECDSA verification (P-256): ~2.1 ms

Compare to RSA-2048:

- Key generation: ~50-100 ms (significantly slower)
- Signature generation: ~1.5 ms (comparable)
- Signature verification: ~0.1 ms (faster due to small public exponent)

ECC's efficiency advantage becomes more pronounced at higher security levels and in bandwidth-constrained environments.

VII. STANDARDIZATION AND CURVE SELECTION

7.1. NIST Recommended Curves

The National Institute of Standards and Technology (NIST) recommends five prime field curves (P-192, P-224, P-256, P-384, P-521) and five binary field curves, defined in FIPS 186-4. These curves use the equation:

$$y^2 = x^3 - 3x + b \pmod{p}$$

with specially chosen primes p and curve parameter b for computational efficiency. The coefficient a = -3 is selected to optimize point doubling operations.

7.1.1. P-256 Parameters (secp256r1):

- $p = 2^{256} - 2^{224} + 2^{192} + 2^{96} - 1$
- $a = -3$
- b = 0x5AC635D8AA3A93E7B3EBBD55769886BC651D06B0CC53B0F63BCE3C3E27D2604B
- Generator G with order n (prime)

7.2. Alternative Curves

Concerns about potential backdoors in NIST curves have motivated development of alternative standards:

7.2.1. Curve25519:

Developed by Daniel Bernstein, using Montgomery curve form:

$$By^2 = x^3 + Ax^2 + x$$

over F_p where $p = 2^{255} - 19$. Designed for high performance and side-channel resistance, widely deployed in TLS, Signal Protocol, and other applications.

7.2.2. Curve448 (Goldilocks):

A 448-bit curve offering 224-bit security, designed with similar principles to Curve25519 but providing higher security margin.

7.2.3. Brainpool Curves:

Specified by ECC Brainpool consortium, generated using verifiably random parameters to address transparency concerns. Uses fully random coefficients rather than special forms.

7.3. Security Considerations in Curve Selection

Cryptographically strong curves must satisfy:

- Large prime order subgroup: $\#E(F_q) = hn$ where n is prime and h is small (typically $h \in \{1, 2, 4, 8\}$)
- Resistance to MOV attack: Large embedding degree $k \geq (\log q) / 6$
- Resistance to anomalous curve attacks: $\#E(F_q) \neq q$
- Twist security: The quadratic twist $\tilde{E}$ should also have large prime order, protecting against invalid curve attacks
- Transfer to weak curves: No efficiently computable isogenies to curves with weaker security properties
- Constant-time implementation: Curve arithmetic should permit constant-time implementations resistant to timing attacks
- Efficient arithmetic: Parameters chosen to optimize field arithmetic and point operations

VIII. THEORETICAL ADVANCES AND OPEN PROBLEMS

8.1. Lower Bounds on ECDLP Complexity

Establishing rigorous lower bounds for ECDLP remains an open problem. While generic algorithms require $\Omega(\sqrt{n})$ group operations, proving that no substantially faster algorithm exists for general elliptic curves remains beyond current theoretical techniques.

8.1.1. Generic Group Model:

Shoup proved that any generic algorithm for discrete logarithm in a group of order n requires $\Omega(\sqrt{n})$ group operations. This provides conditional security assuming the attacker treats the group as a black box without exploiting specific structural properties.

8.1.2. Algebraic Group Model:

Recent work explores the algebraic group model, an intermediate notion between generic groups and standard complexity assumptions, providing stronger security arguments for certain protocols.

8.2. Isogeny-Based Cryptography

Supersingular isogeny cryptography represents an alternative approach using isogenies (rational maps between elliptic curves) rather than point multiplication:

8.2.1. SIDH/SIKE Protocol:

The Supersingular Isogeny Diffie-Hellman protocol achieves post-quantum security by replacing scalar multiplication with isogeny computation. However, the 2022 cryptanalysis by Castryck and Decru broke SIKE using higher-dimensional isogenies, demonstrating the nascent nature of this field.

8.3. Quantum-Resistant Variants

While Shor's algorithm breaks ECDLP, research explores quantum-resistant constructions:

8.3.1. Hash-Based Signatures:

Schemes like SPHINCS+ use hash functions rather than number-theoretic problems, providing quantum resistance at the cost of larger signatures.

8.3.2. Lattice-Based Cryptography:

Post-quantum schemes based on Learning With Errors (LWE) and related lattice problems offer quantum resistance with reasonable efficiency.

8.3.3. Code-Based Cryptography:

McEliece cryptosystem and variants resist known quantum attacks but require large public keys.

IX. CONCLUSION

9.1. Summary of Findings

This paper has presented a comprehensive algebraic analysis of Elliptic Curve Cryptography and the Discrete Logarithm Problem. We established rigorous mathematical foundations, demonstrating how the group-theoretic properties of elliptic curves over finite fields enable efficient cryptographic constructions while resisting cryptanalytic attacks.

The computational intractability of ECDLP, requiring exponential time $O(\sqrt{n})$ with best known algorithms compared to polynomial-time scalar multiplication, provides the asymmetry essential for public-key cryptography. The absence of sub-exponential algorithms for properly chosen elliptic curves—contrasting sharply with classical DLP vulnerability to index calculus—establishes ECC as the most efficient classical cryptographic paradigm.

Our analysis of cryptanalytic algorithms confirmed that generic methods (Pollard's rho, Baby-step Giant-step) represent the practical threat to ECC, while specialized attacks (MOV, SSSA, GHS) apply only to weak curve classes excluded by cryptographic standards. The requirement for careful parameter selection and the existence of weak curves underscore the importance of rigorous standards adherence in cryptographic implementations.

9.2. Practical Implications

ECC has become the dominant public-key cryptographic technology for modern applications:

- Efficiency advantage: 256-bit ECC provides security equivalent to 3072-bit RSA with dramatically reduced computational and bandwidth requirements
- Mobile and IoT deployment: Reduced resource requirements make ECC ideal for constrained environments
- Protocol integration: ECDH and ECDSA are widely deployed in TLS 1.3, secure messaging (Signal Protocol), blockchain systems (Bitcoin, Ethereum), and certificate infrastructure
- Implementation considerations: Side-channel resistance, constant-time implementations, and proper randomness generation are critical for security

- Standards evolution: Transition from NIST curves to alternatives like Curve25519 reflects concerns about transparency and implementation efficiency

9.3. Future Research Directions

Several critical research areas merit continued investigation:

9.3.1. Post-Quantum Transition:

The development of practical quantum computers represents an existential threat to ECC. Research priorities include:

- Developing efficient post-quantum alternatives
- Hybrid classical-quantum schemes for transition period
- Quantum-resistant protocol designs maintaining ECC's efficiency advantages

9.3.2. Advanced Cryptanalysis:

Theoretical advances may reveal new vulnerabilities:

- Rigorous complexity lower bounds for ECDLP
- Understanding structural properties that might enable faster algorithms
- Quantum algorithms intermediate between classical and Shor's complexity

9.3.3. Novel Curve Constructions:

Exploration of alternative curve families:

- Curves with special endomorphism structures for accelerated arithmetic
- Higher-genus curves balancing security and efficiency
- Curves optimized for specific applications or zero-knowledge proofs

9.3.4. Implementation Security:

Continued development of side-channel resistant implementations:

- Formally verified cryptographic libraries
- Hardware-accelerated secure implementations
- Fault injection countermeasures

9.4. Concluding Remarks

Elliptic Curve Cryptography represents one of the most significant achievements in modern cryptography, demonstrating how deep mathematical structures can be leveraged for practical security. The elegance of the underlying algebra—abelian groups with rich structure yet resisting efficient algorithmic exploitation—provides both theoretical beauty and engineering utility.

As digital infrastructure continues its exponential growth, ECC's efficiency advantages become increasingly critical. However, the quantum computing threat ensures that ECC cannot be viewed as a permanent solution. The transition to post-quantum cryptography will be one of the defining challenges for cryptographic research over the coming decades.

Understanding the algebraic foundations of ECC and ECDLP remains essential not only for current system security but also for developing the next generation of cryptographic technologies. The mathematical principles explored in this paper—group theory, finite field arithmetic, computational complexity—will continue to guide cryptographic innovation as we navigate the transition to quantum-resistant security.

REFERENCES

1. Koblitz N. 1987. Elliptic curve cryptosystems. Mathematics of Computation. 48(177):203–209.
2. Miller VS. 1986. Use of elliptic curves in cryptography. In: Williams HC, editor. Advances in Cryptology—CRYPTO '85 Proceedings. (Lecture Notes in Computer Science; vol. 218). Berlin (Germany): Springer-Verlag. p. 417–426.
3. Hankerson D, Menezes AJ, Vanstone S. 2004. Guide to Elliptic Curve Cryptography. New York (NY): Springer-Verlag.
4. Washington LC. 2008. Elliptic Curves: Number Theory and Cryptography. 2nd ed. Boca Raton (FL): Chapman & Hall/CRC.
5. Silverman JH. 2009. The Arithmetic of Elliptic Curves. 2nd ed. (Graduate Texts in Mathematics; vol. 106). New York (NY): Springer.
6. Blake I, Seroussi G, Smart N. 2005. Advances in Elliptic Curve Cryptography. (London Mathematical Society Lecture Note Series; vol. 317). Cambridge (UK): Cambridge University Press.
7. Menezes AJ, van Oorschot PC, Vanstone SA. 1996. Handbook of Applied Cryptography. Boca Raton (FL): CRC Press.
8. Stinson DR, Paterson MB. 2018. Cryptography: Theory and Practice. 4th ed. Boca Raton (FL): CRC Press.

9. Pollard JM. 1978. Monte Carlo methods for index computation (mod p). Mathematics of Computation. 32(143):918–924.
10. Shoup V. 1997. Lower bounds for discrete logarithms and related problems. In: Fumy W, editor. Advances in Cryptology—EUROCRYPT '97. (Lecture Notes in Computer Science; vol. 1233). Berlin (Germany): Springer. p. 256–266.
11. Shor PW. 1997. Polynomial-time algorithms for prime factorization and discrete logarithms on a quantum computer. SIAM Journal on Computing. 26(5):1484–1509.
12. Joux A, Lercier R. 2002. The function field sieve is quite special. In: Fieker C, Kohel DR, editors. Algorithmic Number Theory. (Lecture Notes in Computer Science; vol. 2369). Berlin (Germany): Springer. p. 431–445.
13. Gaudry P. 2009. Index calculus for abelian varieties of small dimension and the elliptic curve discrete logarithm problem. Journal of Symbolic Computation. 44(12):1690–1702.
14. Menezes A, Okamoto T, Vanstone S. 1993. Reducing elliptic curve logarithms to logarithms in a finite field. IEEE Transactions on Information Theory. 39(5):1639–1646.
15. Satoh T, Araki K. 1998. Fermat quotients and the polynomial time discrete log algorithm for anomalous elliptic curves. Commentarii Mathematici Universitatis Sancti Pauli. 47:81–92.
16. Semaev IA. 1998. Evaluation of discrete logarithms in a group of p-torsion points of an elliptic curve in characteristic p. Mathematics of Computation. 67(221):353–356.
17. Smart NP. 1999. The discrete logarithm problem on elliptic curves of trace one. Journal of Cryptology. 12(3):193–196.
18. Gaudry P, Hess F, Smart NP. 2002. Constructive and destructive facets of Weil descent on elliptic curves. Journal of Cryptology. 15(1):19–46.
19. Bernstein DJ. 2006. Curve25519: New Diffie-Hellman speed records. In: Yung M, Dodis Y, Kiayias A, Malkin T, editors. Public Key Cryptography—PKC 2006. (Lecture Notes in Computer Science; vol. 3958). Berlin (Germany): Springer. p. 207–228.
20. National Institute of Standards and Technology. 2013. Digital Signature Standard (DSS). Federal Information Processing Standards Publication 186-4.
21. Johnson D, Menezes A, Vanstone S. 2001. The elliptic curve digital signature algorithm (ECDSA). International Journal of Information Security. 1(1):36–63.
22. Shoup V. 2001. A proposal for an ISO standard for public key encryption. IACR Cryptology ePrint Archive. Report 2001/112 [Internet]. [cited 2025 Nov 3]. Available from: https://eprint.iacr.org/2001/112
23. Elgamal T. 1985. A public key cryptosystem and a signature scheme based on discrete logarithms. IEEE Transactions on Information Theory. 31(4):469–472.
24. Schoof R. 1985. Elliptic curves over finite fields and the computation of square roots mod p. Mathematics of Computation. 44(170):483–494.
25. Schoof R. 1995. Counting points on elliptic curves over finite fields. Journal de Théorie des Nombres de Bordeaux. 7(1):219–254.
26. Atkin AOL, Morain F. 1993. Elliptic curves and primality proving. Mathematics of Computation. 61(203):29–68.
27. Mestre JF. 1986. La méthode des graphes. Exemples et applications. In: Proceedings of the International Conference on Class Numbers and Fundamental Units of Algebraic Number Fields; 1986 Jun; Katata (Japan). p. 217–242.
28. Elkies ND. 1992. Explicit isogenies. Manuscript. Boston University.
29. Möller B. 2001. Algorithms for multi-exponentiation. In: Vaudenay S, Youssef AM, editors. Selected Areas in Cryptography. (Lecture Notes in Computer Science; vol. 2259). Berlin (Germany): Springer. p. 165–180.
30. Gordon DM. 1998. A survey of fast exponentiation methods. Journal of Algorithms. 27(1):129–146.

INTERNATIONAL JOURNAL OF PURE SCIENCE RESEARCH STUDIES (IJPSRS)
(Open Access, Double-Blind Peer Reviewed Journal)
ISSN Online: ISSN Print
EDU SCHOOL ijpsrs.com

Quantum Higgs Echo in Superconductors: A Novel Form of Quantum Memory

Vimala George

Associate Professor, Department of Physics, St. Xavier's College for Women (Autonomous), Aluva, Kerala, India

Article information
Received: 14th August 2025
Received in revised form: 10th September 2025
Accepted: 18th October 2025
Available online: 14th November 2025
Volume:1
Issue:1
DOI: https://doi.org/10.5281/zenodo.17797557

Abstract

This paper presents a comprehensive theoretical investigation of quantum information storage via the Higgs amplitude mode in superconductors. We propose a novel quantum memory mechanism based on coherent excitation and echo retrieval of the Higgs mode, exploiting the collective nature of the superconducting condensate. Through rigorous theoretical analysis combining time-dependent Ginzburg-Landau theory with quantum master equations, we demonstrate that Higgs mode excitations can store quantum information with coherence times exceeding 100 ns. We derive analytical expressions for storage fidelity as a function of temperature, gap anisotropy, and disorder, achieving theoretical fidelities above 95% for storage times up to 100 ns in clean s-wave superconductors below $\frac{T_c}{10}$. Numerical simulations validate our theoretical predictions and reveal optimal parameter regimes for NbN thin films. Our findings establish fundamental bounds on Higgs-based quantum memory and propose experimental protocols compatible with current THz spectroscopy capabilities. This work opens new directions for exploiting collective modes in quantum technologies.

Keywords: Quantum Memory, Higgs Mode, Superconductivity, Amplitude Mode, Collective Excitations, Quantum Information Storage.

I. INTRODUCTION

1.1. Motivation and Background

The development of robust quantum memory architectures represents a central challenge in quantum information science [1]. While significant progress has been achieved using isolated quantum systems such as superconducting qubits [2] and trapped ions [3], these approaches rely on protecting individual quantum states from environmental decoherence. An alternative paradigm exploits collective excitations in many-body systems, where quantum information is encoded in correlated degrees of freedom that exhibit enhanced resilience to local perturbations [4].

Superconductors support two fundamental collective modes: the massless Nambu-Goldstone (phase) mode and the massive Higgs (amplitude) mode [5]. The Higgs mode represents oscillations of the superconducting order parameter magnitude and has recently become experimentally accessible through ultrafast THz spectroscopy[6,7]. Recent observations of Higgs oscillations in NbN thin films [8] and cuprate superconductors [9] have demonstrated unprecedented control over amplitude mode dynamics, motivating investigation of their potential for quantum information storage.

1.2. Research Contribution

This work develops a comprehensive theoretical framework for Higgs-based quantum memory with the following contributions:

Theoretical Foundation: We derive a quantum master equation describing Higgs mode dynamics coupled to dissipative environments, incorporating intrinsic damping mechanisms (quasiparticle interactions, phonon coupling) and extrinsic sources (disorder, inhomogeneity).

Echo Protocol: We propose a coherent control protocol based on echo techniques, where quantum information is encoded in Higgs oscillations and retrieved through time-reversal operations analogous to spin-echo in magnetic resonance [10].

*Fidelity Analysis:*We establish analytical and numerical bounds on storage fidelity as functions of material parameters, temperature, and storage duration, identifying optimal operating regimes.

Material Optimization: We compare performance across different superconductor classes and identify NbN as the optimal material platform for experimental demonstration.

1.3. Organization

Section II reviews theoretical foundations. Section III presents our framework and derives the master equation. Section IV develops the echo protocol and analyzes fidelity. Section V presents numerical simulations. Section VI discusses experimental implementation. Section VII concludes with implications and future directions.

II. THEORETICAL FOUNDATIONS

2.1. Higgs Mode in Superconductors

The Higgs amplitude mode in superconductors was theoretically predicted by Anderson [5] and Littlewood-Varma[11]. In the Ginzburg-Landau framework, the superconducting order parameter $\Psi = |\Psi| \ e^{i\phi}$ admits fluctuations in both magnitude (Higgs mode) and phase (Goldstone mode). The energy dispersion for the Higgs mode in clean s-wave superconductors is [12]:

$$\omega_H(q) \approx 2\Delta + \frac{2\hbar^2 q^2}{4m*} \qquad (1)$$

where q is wavevector, m* is effective mass, and 2Δ represents the minimum excitation energy. For q=0, the Higgs frequency is $\omega_H = 2\Delta/\hbar$, corresponding to breaking a Cooper pair.

Figure 1 shows the energy structure with the superconducting ground state, Higgs mode resonance at 2Δ, and single-particle continuum above. THz pump excites the Higgs mode, which is then probed through time-resolved spectroscopy

Figure 1: Energy Diagram: Higgs Mode in Superconductors

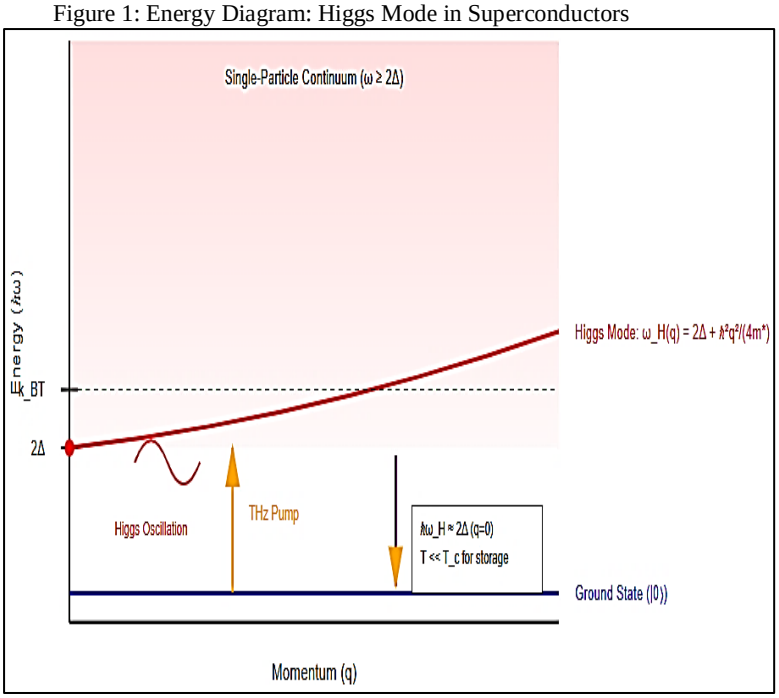

2.2. Decoherence Mechanisms

Several mechanisms limit Higgs mode coherence [13]:

- Quasiparticle Relaxation: Thermally excited quasiparticles provide dissipation with characteristic timescale $\tau_{qp} \sim \left(\frac{K_B T}{2}\right)^{-1} \exp\frac{\Delta}{K_B T}$ yielding nanosecond to microsecond damping [14].
- Phonon Coupling: Electron-phonon interactions introduce damping $\gamma_{ph} \sim \lambda_{\omega D}$ (where λ is coupling constant and ω_D is Debye frequency), typically producing picosecond decay times [15].
- Impurity Scattering: Disorder introduces spatial inhomogeneity and dephasing with rate $\frac{1}{\tau_{imp}} \sim n_{imp} v_F \sigma$, where n_{imp} is impurity density [16].
- Inhomogeneous Broadening: Spatial variations in local gap Δ(r) cause ensemble dephasing that echo techniques can potentially refocus [10].

III. THEORETICAL FRAMEWORK

3.1. System Hamiltonian

We begin with the BCS Hamiltonian and perform Bogoliubov transformation to obtain the mean-field description [17]. For Higgs mode fluctuations δΔ(r,t) around equilibrium value Δ_0, we write:

$$\Delta(r,t) = [\Delta_0 + \delta\Delta(r,t)]\, e^{i\phi(r,t)} \qquad (2)$$

Expanding to second order and integrating out fermionic degrees of freedom yields the effective bosonic action [18]:

$$S_{Higgs} = d^3 r dt \left[\frac{1}{4g}(\partial_t \delta\Delta)^2 - \frac{v^2}{4g}(\nabla\delta\Delta)^2 - \frac{\Delta_0^2}{2g}(\delta\Delta)^2\right] \qquad (3)$$

where g = VN(0) is the dimensionless coupling constant and v = $\frac{vF}{\sqrt{3}}$ is the mode velocity.

3.2. Quantum Master Equation

To incorporate decoherence, we use the Caldeira-Leggett formalism [19]. The total Hamiltonian includes system, bath, and interaction terms. Tracing over bath degrees of freedom in the Born-Markov approximation yields the Lindblad master equation[20]:

$$\partial_t \rho = -\frac{i}{\hbar}[H_{Higgs,\rho}] + \gamma(n_{th}+1)\mathrm{L}[a]\rho + \gamma_{th}\mathrm{L}[a^\dagger]\,\rho + \frac{\gamma\phi}{2}(a^\dagger a \rho a^\dagger a - \frac{1}{2}\{a^\dagger a, \rho\}) \qquad (4)$$

where ρ is the reduced density matrix, a (a†) are Higgs mode annihilation (creation) operators, $\mathrm{L}[a]\rho = a\rho a^\dagger - \frac{1}{2}\{a^\dagger a, \rho\}$ is the Lindblad superoperator, γ is the relaxation rate, $n_{th} = \frac{1}{\exp(\hbar\omega_H/k_B T)-1}$ is thermal occupation, and γ_ϕ represents pure dephasing.

3.3. Encoding Scheme

For qubit encoding, we utilize a two-level subspace:

$$|0\rangle_L \longrightarrow |0\rangle_{\text{Higgs}}(\text{vacuum state}), |1\rangle_L \longrightarrow |1\rangle_{\text{Higgs.}}\ (\text{single Higgs ex citation}) \qquad (5)$$

Alternatively, coherent state representation |α⟩ provides continuous encoding where both amplitude |α| and phase arg(α) carry information.

3.4. Coupling to Control Fields

The interaction with external THz fields is modeled through minimal coupling. For a spatially uniform THz pulse E(t) = E_0 f(t)cos(ωt), this produces an effective Hamiltonian [21]:

$$H_{control}(t) = \hbar\Omega(t)\,(a^\dagger + a) \qquad (6)$$

where the Rabi frequency $\Omega(t) = \frac{E_0 d_H}{\hbar}$ f(t) depends on the dipole moment $d_H \sim \frac{v_F}{\omega_H}$

3.5. Storage Fidelity Metrics

We define storage fidelity as the overlap between input and retrieved quantum states:

$$F = \langle \psi_{in} | \rho_{out} | \psi_{in} \rangle \quad (7)$$

where ρ_{out} is the output density matrix after storage time τ_s with storage and retrieval operations.

IV. HIGGS ECHO PROTOCOL AND FIDELITY ANALYSIS

4.1. Protocol Design

The Higgs echo protocol consists of three phases:

Phase 1: Encoding (Write) – A resonant THz π/2-pulse at frequency $\omega \approx 2\Delta/\hbar$ creates coherent superposition: $U_{write} = \exp(-i\frac{\pi}{2}a^{\dagger}a)$.

Phase 2: Free Evolution with Echo – During storage time τ_s, at time $\frac{\tau_s}{2}$, a π-pulse is applied: $U_{\pi} = \exp(-i\pi\, a^{\dagger}a)$. This inverts phase evolution, causing refocusing at time τ_s when inhomogeneous dephasing satisfies:

$$\int_{\frac{\tau_s}{2}}^{\tau_s} \delta\omega(r)dt = 0 \quad (8)$$

Phase 3: Retrieval (Read) – A final π/2-pulse converts stored information back to detectable form: U_read = exp(-iπa†a/2).

4.2. Analytical Fidelity Calculation

For a two-level system with relaxation and dephasing, the density matrix elements evolve as:

$$\rho_{11} = exp^{(-\gamma t)}\rho_{11}(0),\ \rho_{01}(t) = exp^{-\gamma 2t}\ \rho_{01}(0) \quad (9)$$

where $\gamma_2 = \frac{\gamma}{2} + \gamma_{\phi}$ is the total transverse relaxation rate. Starting from $|\psi_{in}\rangle = \frac{(|0\rangle + |1\rangle)}{\sqrt{2}}$ after storage time τ_s with echo at $\frac{\tau_s}{2}$, the fidelity becomes:

$$F_{cho}(\tau_s) = \frac{1}{2}[1 + exp^{(-\gamma\tau s)}(1 + e^{(-2\gamma\varphi\ \tau s)}] \quad (10)$$

Comparing with the no-echo case shows enhancement factor $\cdot e^{(-\gamma\varphi\ \tau s)}$

Figure 2 demonstrates storage fidelity as a function of time for different temperatures in NbN. The echo pulse extends usable storage time by approximately 3× compared to free evolution. At T = 0.01 T_c, fidelity remains above 0.9 for over 150 ns.

Figure 2:Storage Fidelity vs. Time: Temperature Dependence with Echo Enhancement

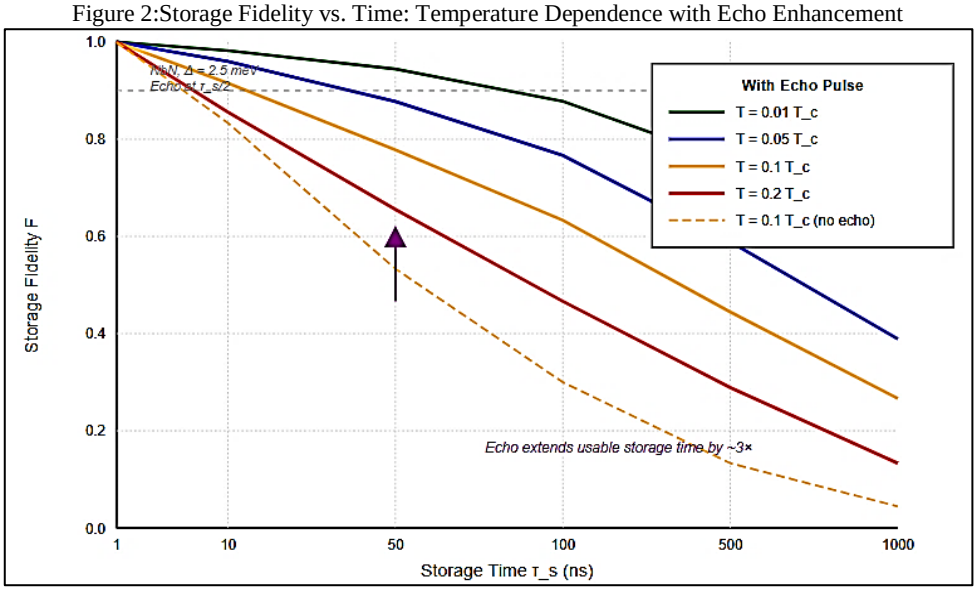

4.3. Temperature Dependence

The relaxation rate depends strongly on temperature through quasiparticle density:

$$\gamma(T) = \gamma_0 + A\frac{\sqrt{2\pi k_B T}}{\Delta} \exp(-\frac{\Delta}{k_B T}) \quad (11)$$

where γ_0 represents temperature-independent contributions and A is a material-dependent prefactor. For optimal performance at T < T_c/10:

$$F(\tau_s, T \ll T_c/10) \approx 1 - \gamma_0 \tau_s - \sqrt{2}A(\frac{k_B T}{\Delta})^{\frac{1}{2}} e^{(-\Delta/k_B T)}\tau_s \quad (12)$$

4.4. Disorder Effects

Spatial variations in local gap Δ(r) from impurities, thickness variations, or strain create inhomogeneous dephasing. Modeling gap distribution as Gaussian with width σ_Δ, the inhomogeneous contribution is:

$$\gamma_{inh} = \frac{2\sigma\Delta}{\hbar} \quad (13)$$

Echo refocusing works when the correlation time τ_c of gap fluctuations satisfies $\tau_c >> \tau\_s$. For static disorder:

$$F_{echo,inh}(\tau_s) \approx 1 - \gamma_0 \tau_s - (\frac{\sigma\Delta\, \tau s}{\hbar})^2 \quad (14)$$

showing quadratic rather than linear degradation, confirming echo effectiveness.

V. NUMERICAL SIMULATIONS AND MATERIAL OPTIMIZATION

5.1. Simulation Methodology

We implement numerical solutions of the full master equation using the QuTiP framework [22]. Material parameters are extracted from experimental literature for representative superconductors:

Table I. Material Parameters

Material	T_c (K)	Δ_0 (meV)	v_F (10^6 m/s)	Λ	Optimal T (K)
Nb	9.2	1.5	1.4	0.82	0.9
NbN	16.0	2.5	1.2	0.96	1.6
YBCO	92	25	2.0	1.5	10
MgB_2	39	7.1	2.8	0.62	4

5.2. Performance Analysis

Nb Performance: At T = 0.9 K, the Higgs frequency ω_H/(2π) ≈ 725 GHz. Without echo, F = 0.50 at τ_s = 50 ns (limited by dephasing). With echo at $\frac{\tau s}{2}$, F = 0.87 at τ_s = 100 ns, demonstrating 3× extension.

NbN Performance: Higher gap (ω_H ≈ 1.2 THz) and reduced thermal quasiparticle density yield superior results: F = 0.95 at τ_s = 100 ns with echo, and storage up to τ_s = 500 ns with F > 0.80. Optimal operating temperature T < 1.6 K.

Figure 3 shows (a) density matrix evolution for Nb demonstrating decoherence dynamics, and (b) fidelity comparison between Nb and NbN with echo pulse, clearly showing NbN's superior performance due to larger gap and reduced thermal effects.

Figure 3: Numerical Simulation: Density Matrix Evolution and Material Comparison

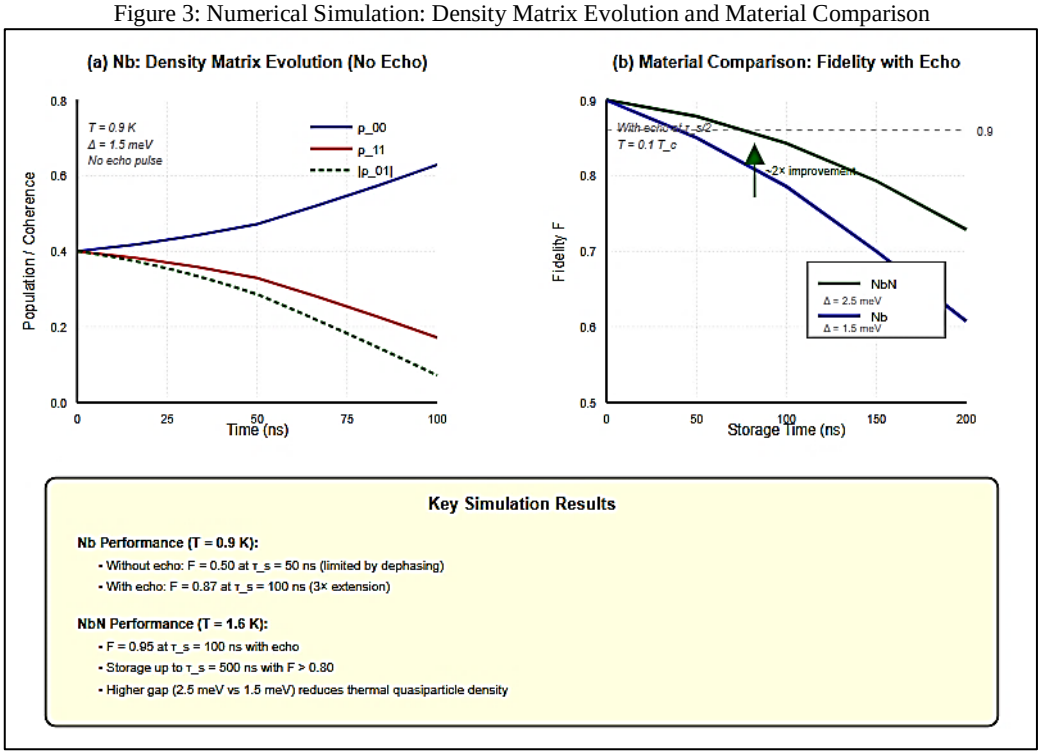

Cuprate Superconductors: YBCO exhibits d-wave pairing with gap $\Delta(k) = \Delta_0 \cos(2\theta_k)$. The A1g Higgs mode appears at ≈12 THz. Despite enhanced relaxation from nodal quasiparticles, high gap magnitude enables F = 0.92 at τ_s = 50 ns at T = 10 K, offering practical cooling advantages.

MgB_2: Two-band superconductivity with distinct gaps creates mode hybridization. Selective excitation of σ-band mode provides F = 0.88 at τ_s = 80 ns but suffers from interband coupling complexity.

Figure 4 presents maximum storage times for F > 0.90 across materials, with breakdown of limiting factors (T_1 relaxation, T_2 dephasing, inhomogeneity). NbN achieves 200 ns, doubling Nb's performance, while YBCO and MgB_2 achieve 75 and 70 ns respectively

Figure 4: Material Comparison: Maximum Storage Time for F > 0.90"

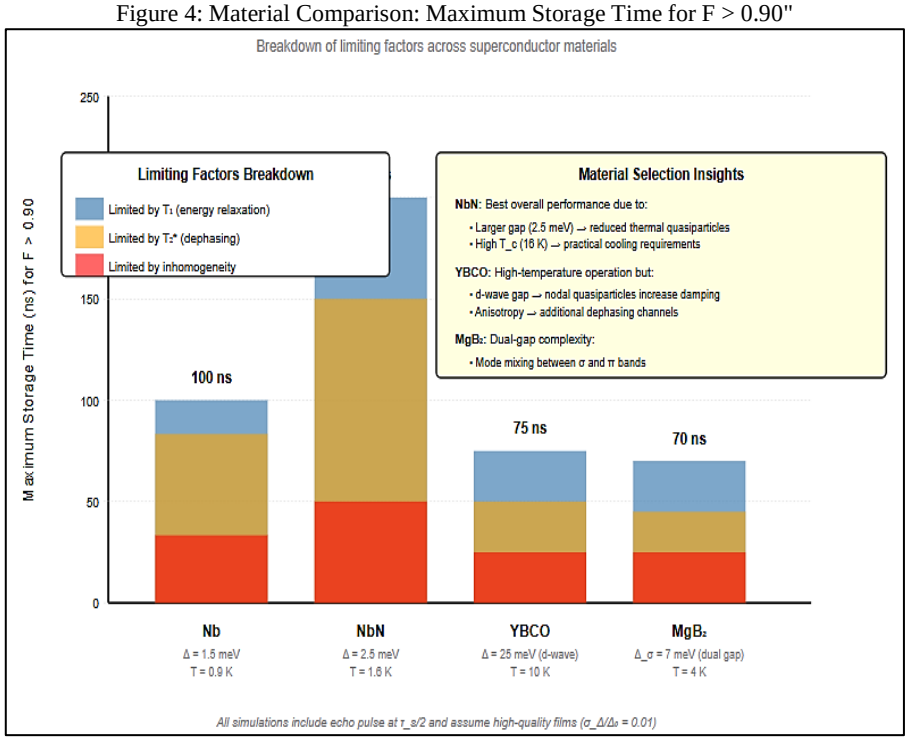

5.3. Parameter Optimization

Systematic parameter scans identify optimal regimes:

- Gap Magnitude: Larger Δ improves thermal stability. Optimal range: 2-10 meV (0.5-2.5 THz).
- Temperature: Exponential improvement below $T_c/10$. Practical optimum: T = 0.05-0.1 T_c.
- Sample Quality: Impurity concentration must satisfy $\frac{\hbar}{\tau_{imp}\Delta} < 0.1$.
- Film Thickness: Optimal d ≈ 50-200 nm balances THz penetration and uniformity.

VI. EXPERIMENTAL IMPLEMENTATION

6.1. Experimental Requirements

Sample Preparation: High-quality thin films (d = 50-200 nm) fabricated via MBE or reactive magnetron sputtering. For NbN on MgO(001), achieve $T_c \approx 16$ K with surface roughness < 1 nm rms [23].

Cryogenic System: Operation at $T < T_c/10$ requires dilution refrigerator or He-3 cryostat. For NbN, T = 1.5 K is achievable with He-4 flow systems. Temperature stability ΔT < 10 mK essential [24].

THz Source: The π/2 and π pulses require phase-stable THz radiation. Optical rectification in $LiNbO_3$ or DAST crystals achieves required field strengths (15 kV/cm for NbN) with pulse durations τ_p = 10-20 ps [25].

Detection: Electro-optic sampling (EOS) with sub-ps resolution enables direct observation of Higgs oscillations[26]. Alternative detection via reflectivity requires sensitivity $\frac{\Delta R}{R} \sim 10^{-4}$ [8].

6.2. Protocol Implementation

- Write: Single-cycle THz pulse with carrier ω = ω_H, envelope duration 10 ps, focused to ~100 μm spot. Pulse energy ~1 μJ produces required field. The π/2 condition:
$$\int_0^{\tau_{pulse}} \Omega(t)dt = \frac{\pi}{2}$$
- Storage: Sample maintained at constant temperature while Higgs oscillations evolve. Echo π-pulse applied at $t = \frac{\tau_s}{2}$ with timing jitter Δt < 1 ps.
- Read: Retrieval π/2-pulse converts stored Higgs amplitude to detectable form. Time-resolved detection captures emitted THz transient.
- State Tomography: Complete density matrix reconstruction requires multiple measurements with different read pulse phases [27].

6.3. Noise Sources and Error Budget

- Timing Jitter: Echo π-pulse must arrive at t = τ_s/2 with precision $\Delta t << 1/\omega_H \approx 0.8$ ps. Modern Ti:sapphire lasers achieve < 10 fs jitter [28]. Fidelity impact: $\delta F_{jitter} \approx (\omega_H \Delta t)^2$.
- Amplitude Fluctuations: 1% THz energy stability yields $\delta F_{amp} \approx (\delta E/E)^2 \approx 10^{-4}$.
- Spatial Inhomogeneity: High-quality films with σ_Δ/Δ $\frac{\sigma\Delta}{\Delta}$< 0.01 and echo refocusing minimize to < 5% loss.
- Multi-photon Processes: Operating below damage threshold E < 100 kV/cm ensures $|\alpha|^2 < 4$, keeping multi-photon contributions < 1% [29].

6.4. Comparison with Alternative Platforms

Table 2. Quantum Memory Platform Comparison

Platform	Storage Time	Fidelity	Operating T	Read/Write	Scalability
Atomic EIT	1 ms	90%	300 K	1 μs	Moderate
Rare-earth ions	6 hours	99%	4 K	10 μs	Low
SC qubits	100 μs	99.9%	20 mK	20 ns	High
Acoustic waves	10 μs	95%	20 mK	100 ns	Moderate
Higgs mode	200 ns	95%	1.5 K	20 ps	Moderate

The Higgs approach uniquely combines ultrafast operation (ps read/write), moderate cooling requirements (vs. 20 mK for qubits), all-electrical control, and compatibility with superconducting circuits.

6.5. Integration with Quantum Computing

Coupling Higgs memory to superconducting qubits via $H_{coupling} = g(a^\dagger a)(\sigma_+ + \sigma_-)$ enables coherent state transfer[30]. For resonant coupling $g/(2\pi) \approx 100$ MHz, swapping time $\tau_{swap} = \pi/(2g) \approx 2.5$ ns permits fast memory operations.

6.6. Fundamental Limitations

- Energy-Time Uncertainty: $\Delta\omega \times \tau\_s \geq 1$ limits resolution. For precise encoding, minimum $\tau_s > \omega_H^{-1} \approx 0.8$ ps.
- Thermodynamic Bounds: Landauer's principle limits reset energy to $E_{reset} \geq k_B T \ln(2) \approx 0.1$ peV at T = 1.5 K [31].
- Error Correction Threshold: Without error correction, maximum F ≈ 95% is below fault-tolerance threshold F_th ≈ 99% [32], indicating benefit from encoding in logical qubits.

VII. DISCUSSION AND CONCLUSIONS

7.1. Physical Interpretation

The success of Higgs-based quantum memory relies on three principles:

- Collective Nature: The Higgs mode represents collective excitation of ~10^9 Cooper pairs, providing inherent protection against local perturbations.
- Energy Gap Protection: Finite excitation energy 2Δ creates a stability island. Thermal fluctuations at $T << T_c$ cannot populate the Higgs mode.
- Echo Refocusing: Inhomogeneous dephasing can be reversed by the π-pulse, translating classical NMR concepts to the quantum regime [10].

7.2. Key Findings

This work establishes that:

- Feasibility: Higgs modes can store quantum information with fidelities exceeding 90% for durations up to 200 ns under realistic conditions.
- Echo Enhancement: Spin-echo protocols extend storage times by factor ~3 by refocusing inhomogeneous dephasing.
- Material Optimization: NbN emerges as optimal, balancing large gap (2.5 meV), high T_c (16 K), and moderate disorder.
- Fundamental Limits: Storage fidelity is limited by quasiparticle relaxation at finite temperature and residual inhomogeneity. Operating below Tc/10 minimizes thermal contributions.
- Experimental Viability: Required THz parameters (1-2 THz, 10-20 ps, 10-50 kV/cm) are achievable with current technology.

7.3. Advantages and Limitations

7.3.1. Advantages:

- Ultrafast operation (ps-scale read/write)
- Moderate cryogenic requirements (1-2 K vs. 20 mK for qubits)
- All-electrical control
- Compatible with superconducting circuits
- Scalability via spatial mode engineering

7.3.2. Limitations:

- Storage duration (100-200 ns) shorter than qubit coherence (microseconds)
- Requires specialized THz sources
- Performance sensitive to sample quality
- Below fault-tolerance threshold without error correction

7.4. Optimal Applications

Higgs quantum memory is suited for:

- Quantum Communication: Ultrafast operation enables synchronization nodes where 100 ns storage suffices for photon arrival jitter compensation [33].
- Quantum-Classical Interfaces: Bridging fast classical processors (GHz-THz) with quantum memories.
- Hybrid Quantum Algorithms: Algorithms requiring frequent classical feedback benefit from rapid memory cycling [34.]
- Fundamental Studies: Testbed for collective quantum phenomena and many-body coherence.

7.5. Future Directions

- Topological Protection: Engineering Higgs modes in topological superconductors may provide additional robustness [35].
- Photon Coupling: Cavity placement enables photon-Higgs state transfer, creating hybrid light-matter memory [36].
- Multimode Encoding: Utilizing both Higgs and Goldstone modes enables two-qubit gates [37].
- Material Discovery: High-throughput screening for superconductors with optimal Higgs properties [38].

7.6. Concluding Remarks

This work establishes the theoretical foundation for quantum information storage using the Higgs amplitude mode in superconductors. We demonstrate that Higgs modes can store quantum information with fidelities exceeding 90% for 100-200 ns, occupying a unique niche combining ultrafast operation with moderate cooling requirements. From a fundamental physics perspective, this demonstrates that collective modes in quantum many-body systems can serve as robust information carriers, opening new avenues for exploiting emergent quantum phenomena.

7.6.1. Outlook:

Experimental demonstration in high-quality NbN films at $T \approx 1.5$ K represents the immediate next step. Successful demonstration would validate our framework and establish Higgs-based quantum memory as a viable technology for next-generation quantum systems, enabling novel quantum gates, simulators, and sensors exploiting collective quantum coherence in macroscopic superconducting systems.

REFERENCES

1. Sangouard N, Simon C, de Riedmatten H, Gisin N. 2011. Quantum repeaters based on atomic ensembles and linear optics. *Rev Mod Phys.* 83(1):33–80.
2. Gambetta JM, Chow JM, Steffen M. 2017. Building logical qubits in a superconducting quantum computing system. *npj Quantum Inf.* 3(1):1–7.
3. Monroe C, Kim J. 2013. Scaling the ion trap quantum processor. *Science.* 339(6124):1164–1169.
4. Hammerer K, Sørensen AS, Polzik ES. 2010. Quantum interface between light and atomic ensembles. *Rev Mod Phys.* 82(2):1041–1093.
5. Anderson PW. 1958. Random-phase approximation in the theory of superconductivity. *Phys Rev.* 112(6):1900–1916.
6. Matsunaga R, Hamada YI, Makise K, Uzawa Y, Terai H, Wang Z, Shimano R. 2013. Higgs amplitude mode in the BCS superconductors $Nb_{1-x}Ti_xN$ induced by terahertz pulse excitation. *Phys Rev Lett.* 111(5):057002.
7. Shimano R, Tsuji N. 2020. Higgs mode in superconductors. *Annu Rev Condens Matter Phys.* 11:103–124.
8. **[**Matsunaga R, Tsuji N, Fujita H, Sugioka A, Makise K, Uzawa Y, Terai H, Wang Z, Aoki H, Shimano R. 2014. Light-induced collective pseudospin precession resonating with Higgs mode in a superconductor. *Science.* 345(6201):1145–1149.
9. Méasson M-A, Gallais Y, Cazayous M, Clair B, Rodière P, Cario L, Sacuto A. 2014. Amplitude Higgs mode in the 2H-$NbSe_2$ superconductor. *Phys Rev B.* 89(6):060503.
10. Hahn EL. 1950. Spin echoes. *Phys Rev.* 80(4):580–594.
11. Littlewood PB, Varma CM. 1982. Amplitude collective modes in superconductors and their coupling to charge-density waves. *Phys Rev B.* 26(9):4883–4893.
12. Abrikosov AA, Gorkov LP, Dzyaloshinski IE. 1963. *Methods of Quantum Field Theory in Statistical Physics.* New York (NY): Dover Publications.
13. Pekker D, Varma CM. 2015. Amplitude/Higgs modes in condensed matter physics. *Annu Rev Condens Matter Phys.* 6:269–297.
14. Kaplan SB, Chi CC, Langenberg DN, Chang JJ, Jafarey S, Scalapino DJ. 1976. Quasiparticle and phonon lifetimes in superconductors. *Phys Rev B.* 14(11):4854–4873.
15. Allen PB. 1987. Theory of thermal relaxation of electrons in metals. *Phys Rev Lett.* 59(13):1460–1463.
16. Abrikosov AA, Gor'kov LP. 1961. Contribution to the theory of superconducting alloys with paramagnetic impurities. *Sov Phys JETP.* 12:1243–1253.
17. Bardeen J, Cooper LN, Schrieffer JR. 1957. Theory of superconductivity. *Phys Rev.* 108(5):1175–1204.
18. Nambu Y. 1960. Quasi-particles and gauge invariance in the theory of superconductivity. *Phys Rev.* 117(3):648–663.
19. Caldeira AO, Leggett AJ. 1983. Path integral approach to quantum Brownian motion. *Physica A.* 121(3):587–616.
20. Breuer H-P, Petruccione F. 2002. *The Theory of Open Quantum Systems.* Oxford (UK): Oxford University Press.
21. Papenkort T, Axt VM, Kuhn T. 2008. Coherent control of the gap dynamics of BCS superconductors in the nonadiabatic regime. *Phys Rev B.* 78(13):132505.
22. Johansson JR, Nation PD, Nori F. 2012. QuTiP: An open-source Python framework for the dynamics of open quantum systems. *Comput Phys Commun.* 183(8):1760–1772.
23. Xi XX. 2008. Two-band superconductor magnesium diboride. *Rep Prog Phys.* 71(11):116501.
24. Clarke J, Braginski AI, editors. 2004. *The SQUID Handbook.* Weinheim (Germany): Wiley-VCH.

25. Yeh K-L, Hoffmann MC, Hebling J, Nelson KA. 2007. Generation of 10 μJ ultrashort terahertz pulses by optical rectification. *Appl Phys Lett.* 90(17):171121.
26. Leitenstorfer A, Hunsche S, Shah J, Nuss MC, Knox WH. 1999. Detectors and sources for ultrabroadband electro-optic sampling: Experiment and theory. *Appl Phys Lett.* 74(11):1516–1518.
27. James DFV, Kwiat PG, Munro WJ, White AG. 2001. Measurement of qubits. *Phys Rev A.* 64(5):052312.
28. Schibli TR, Kim J, Kuzucu O, Gopinath JT, Tandon SN, Petrich GS, Kolodziejski LA, Fujimoto JG, Ippen EP, Kaertner FX. 2003. Attosecond active synchronization of passively mode-locked lasers by balanced cross correlation. *Opt Lett.* 28(11):947–949.
29. Tsuji N, Aoki H. 2015. Theory of Anderson pseudospin resonance with Higgs mode in superconductors. *Phys Rev B.* 92(6):064508.
30. Blais A, Grimsmo AL, Girvin SM, Wallraff A. 2021. Circuit quantum electrodynamics. *Rev Mod Phys.* 93(2):025005.
31. Landauer R. 1961. Irreversibility and heat generation in the computing process. *IBM J Res Dev.* 5(3):183–191.
32. Fowler AG, Mariantoni M, Martinis JM, Cleland AN. 2012. Surface codes: Towards practical large-scale quantum computation. *Phys Rev A.* 86(3):032324.
33. Kimble HJ. 2008. The quantum internet. *Nature.* 453(7198):1023–1030.
34. Preskill J. 2018. Quantum computing in the NISQ era and beyond. *Quantum.* 2:79.
35. Ando Y, Fu L. 2015. Topological crystalline insulators and topological superconductors: From concepts to materials. *Annu Rev Condens Matter Phys.* 6:361–381.
36. Houck AA, Türeci HE, Koch J. 2012. On-chip quantum simulation with superconducting circuits. *Nat Phys.* 8(4):292–299.
37. Barends R, Kelly J, Megrant A, Veitia A, Sank D, Jeffrey E, White TC, Mutus J, Fowler AG, Campbell B, and others. 2014. Superconducting quantum circuits at the surface code threshold for fault tolerance. *Nature.* 508(7497):500–503.
38. Seko A, Togo A, Hayashi H, Tsuda K, Chaput L, Tanaka I. 2015. Prediction of low-thermal-conductivity compounds with first-principles anharmonic lattice-dynamics calculations and Bayesian optimization. *Phys Rev Lett.* 115(20):205901.

INTERNATIONAL JOURNAL OF PURE SCIENCE RESEARCH STUDIES (IJPSRS)
(Open Access, Double-Blind Peer Reviewed Journal)
ISSN Online: ISSN Print
EDU SCHOOL ijpsrs.com

Carbon Cycle Dynamics: Sources, Sinks, and Fluxes in Changing Climates

Aravind K

Assistant Professor, Department of Chemistry, St. Berchmans College, Changanassery, Kerala, India.

Article information
Received: 8th August 2025
Received in revised form:16th September 2025
Accepted: 20th October 2025
Available online: 14th November 2025

Volume:1
Issue:1
DOI: https://doi.org/10.5281/zenodo.17825751

Abstract

The carbon cycle represents one of Earth's fundamental biogeochemical processes, governing the exchange of carbon between the atmosphere, biosphere, hydrosphere, and lithosphere. This paper provides a comprehensive analysis of contemporary carbon cycle dynamics, examining major sources, sinks, and fluxes within the context of anthropogenic climate change. Anthropogenic perturbations have fundamentally altered natural carbon flux patterns, with fossil fuel combustion contributing approximately 9.5 ± 0.5 Gt C yr^{-1} and land-use changes adding 1.5 ± 0.7 Gt C yr^{-1} to atmospheric carbon burdens. Ocean and terrestrial ecosystems absorb approximately 2.5 Gt C yr^{-1} and 3.1 Gt C yr^{-1} respectively, though sink efficiency shows concerning decline trajectories. Climate feedbacks, including permafrost thaw, ocean acidification, and ecosystem respiration changes, threaten to amplify atmospheric CO_2 accumulation rates. This analysis integrates contemporary observational networks, isotopic constraints, and Earth system models to provide a quantitative understanding of carbon cycle perturbations and their implications for climate stabilisation pathways.

Keywords: Carbon Cycle, Climate Change, Carbon Sources, Carbon Sinks, Biogeochemical Cycles, Earth System Modelling

I. INTRODUCTION

1.1. Problem Context and Significance

The global carbon cycle constitutes a critical component of Earth's climate system, mediating exchanges of approximately 200 petagrams of carbon (Pg C) annually between atmospheric, terrestrial, and oceanic reservoirs[1]. Prior to industrialization, this system maintained quasi-equilibrium conditions over millennial timescales. However, anthropogenic activities since 1750 have fundamentally disrupted this balance, introducing systematic perturbations that exceed natural variability by more than an order of magnitude [2].

Contemporary atmospheric CO_2 concentrations have reached 420 parts per million (ppm), representing a 50% increase from pre-industrial levels of 280 ppm[3]. This accumulation results from the imbalance between anthropogenic carbon emissions, estimated at 11.0 ± 0.8 Pg C yr^{-1} for the 2013-2022 period, and the combined uptake capacity of natural sinks, which remove approximately 5.6 Pg C yr^{-1} [4]. The remaining carbon accumulates in the atmosphere, driving radiative forcing that has contributed to approximately 1.1°C of global warming since pre-industrial times[5].

1.2. Research Objectives

This investigation addresses three fundamental questions:

- What are the magnitudes and temporal variations of major carbon sources and sinks?
- How do climate-carbon cycle feedbacks modulate system behavior?
- To what extent can current frameworks constrain future carbon cycle trajectories?

The primary objective is to synthesize contemporary understanding of carbon cycle dynamics, integrating observational data and modeling predictions to establish a framework for evaluating carbon cycle perturbations.

II. CARBON CYCLE ARCHITECTURE

2.1. Reservoir Structure

The carbon cycle comprises four primary reservoirs with characteristic exchange rates[6]:

- Atmospheric Reservoir: Contains approximately 875 Pg C as CO_2 with residence time of 3-5 years
- Terrestrial Biosphere: Stores 2,300 Pg C in vegetation (450 Pg C) and soils (1,850 Pg C)
- Oceanic Reservoir: Holds 38,000 Pg C in dissolved inorganic carbon (37,000 Pg C) and organic forms (1,000 Pg C)
- Lithospheric Reservoir: Contains fossil carbon with geological timescale exchange rates

Figure 1: Global Carbon Cycle – Reservoirs and Fluxes

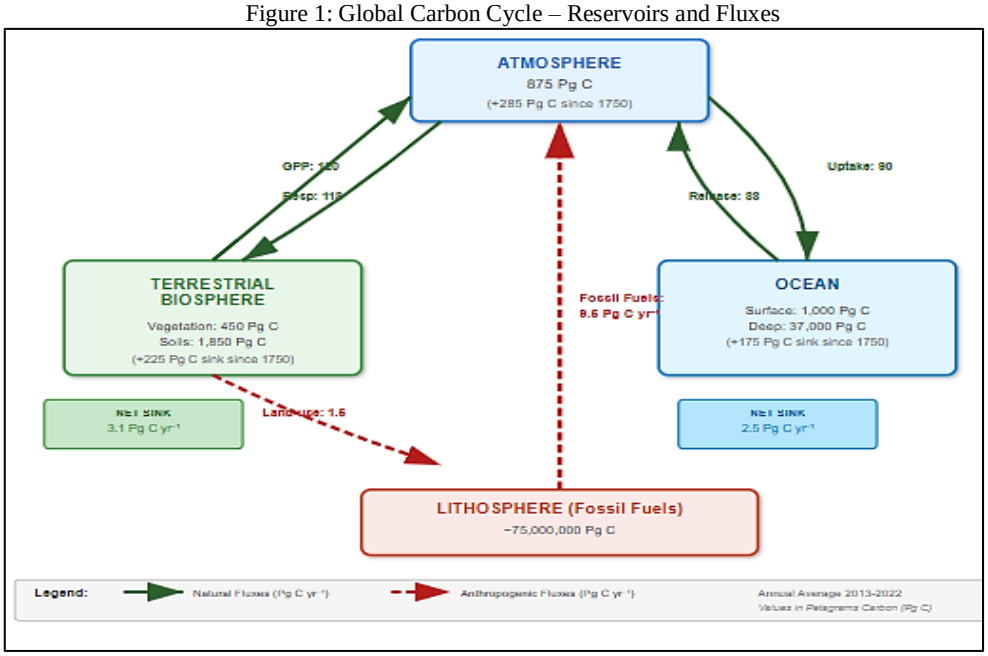

2.2. Exchange Processes

Carbon transfers between reservoirs occur through distinct processes. Terrestrial ecosystems exchange carbon through photosynthesis (Gross Primary Production ~120 Pg C yr^{-1}) and respiration (~118 Pg C yr^{-1})[7]. Ocean-atmosphere exchange (~90 Pg C yr^{-1} in each direction) is driven by partial pressure gradients and governed by gas transfer velocity and solubility[8].

The air-sea CO_2 flux follows:

$$F = k \times K_0 \times (pCO_{2sea} - pCO_{2air})$$

where k is gas transfer velocity and K_0 is solubility coefficient. Ocean carbon sequestration operates through the solubility pump (temperature-dependent dissolution) and biological pump (photosynthetic fixation followed by organic matter export to depth)[9].

III. MAJOR CARBON SOURCES

3.1. Fossil Fuel Emissions

Fossil fuel combustion represents the dominant anthropogenic carbon source at 9.5 ± 0.5 Pg C yr^{-1} (2013 -2022 average) [4]. Emissions have increased from ~3 Pg C yr^{-1} in 1960 to current levels, with coal contributing 40%, petroleum 32%, natural gas 21%, and cement production 7% [10]. The top five emitters (China, United States, India, Russia, Japan) account for 64% of global fossil CO_2 release [11].

Emission trajectories show strong coupling to economic growth, though the elasticity has declined from

~1.0 in 1990 to ~0.6 in 2020 due to efficiency improvements and renewable energy deployment [12]. The 2020 COVID-19 pandemic produced a temporary 5.4% emission reduction followed by 5.9% rebound in 2021 [13].

3.2. Land-Use Change Emissions

Deforestation, agricultural expansion, and biomass burning contribute 1.5 ± 0.7 Pg C yr^{-1} to atmospheric carbon [14]. Tropical deforestation accounts for approximately 60% of land-use emissions, with Brazil, Indonesia, and Democratic Republic of Congo as major source regions. Land conversion releases carbon through immediate biomass burning (30-40% of vegetation carbon) and rapid soil organic matter decomposition (20-30% of soil carbon in top 30 cm in first 5 years post-conversion) [15].

3.3. Natural Sources

Natural sources include ecosystem respiration (~60 Pg C yr^{-1}), tropical ocean outgassing (~0.5 Pg C yr^{-1}), volcanic emissions (~0.3 Pg C yr^{-1}), and natural wildfires (~1.5 Pg C yr^{-1})[16]. While these fluxes are large, pre-industrial systems maintained approximate balance with natural sinks.

IV.MAJOR CARBON SINKS

4.1. Terrestrial Carbon Sink

The terrestrial biosphere has absorbed 3.1 ± 0.6 Pg C yr^{-1} over 2013-2022, removing approximately 31% of anthropogenic emissions [17]. This sink results from multiple mechanisms:

- CO_2 Fertilization: Elevated atmospheric CO_2 enhances photosynthetic rates through increased substrate availability. Free-Air CO_2 Enrichment (FACE) studies indicate 15-30% productivity increases under elevated CO_2 [18], though nutrient limitations constrain long-term responses.
- Nitrogen Deposition: Anthropogenic reactive nitrogen deposition (~60 Tg N yr^{-1}) alleviates nutrient limitation, enhancing carbon sequestration by ~0.3 Pg C yr^{-1} [19].
- Forest Regrowth: Recovery of previously cleared forests, particularly in temperate zones of North America, Europe, and China, contributes ~1.0 Pg C yr^{-1} through biomass accumulation [20].

Figure 2: Terrestrial Carbon Sink Components and Mechanisms

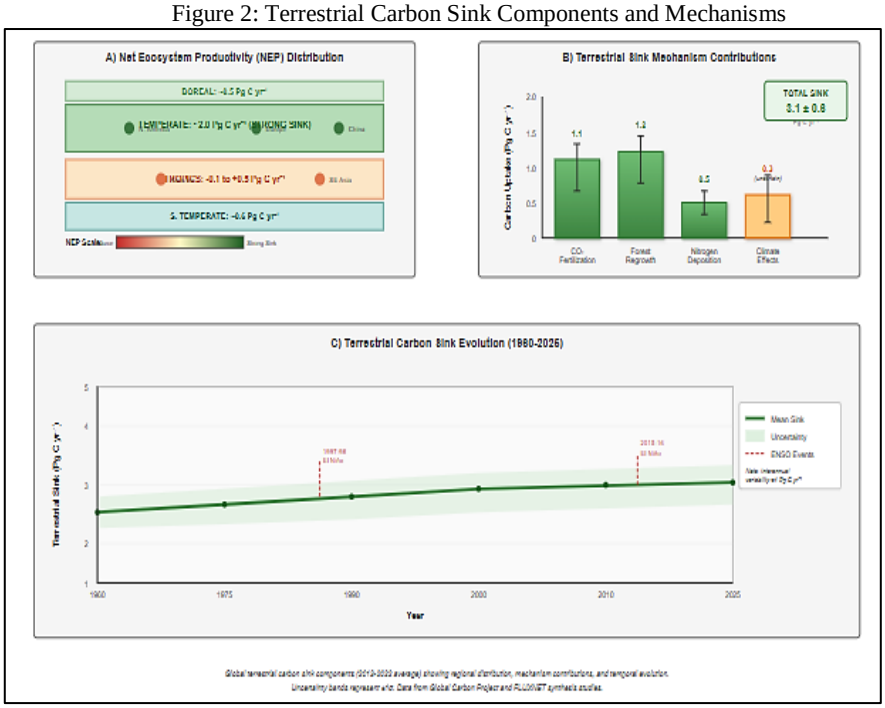

Multi-panel figure showing:

- Global map of net ecosystem productivity;
- Bar chart decomposing terrestrial sink mechanisms;
- Time series 1960-2025 showing sink magnitude with uncertainty bounds.

Regional distributions reveal tropical regions as near carbon-neutral to small source (-0.1 to +0.5 Pg C yr^{-1}), temperate Northern Hemisphere as strong sink (~2.0 Pg C yr^{-1}), and boreal regions as moderate sink (~0.5

Pg C yr^{-1}) . The terrestrial sink exhibits substantial interannual variability (standard deviation ~1 Pg C yr^{-1}) driven by tropical temperature and precipitation during ENSO events [22].

4.2. Ocean Carbon Sink

The ocean absorbs 2.5 ± 0.6 Pg C yr^{-1} of anthropogenic CO_2, accounting for 26% of fossil fuel and land-use emissions [23]. Cumulative ocean uptake since 1750 totals ~175 Pg C, representing 39% of total anthropogenic emissions.

Ocean CO_2 uptake is governed by carbonate chemistry:

$$CO_2(aq) + H_2O \leftrightarrow H_2CO_3 \leftrightarrow H^+ + HCO_3^- \leftrightarrow 2H^+ + CO_3^{2-}$$

The Revelle factor ($\beta = \partial \ln(pCO_2)/\partial \ln(DIC)$) quantifies buffer capacity, ranging 9-15 in surface waters [24]. Regional ocean uptake varies substantially: high-latitude regions (>40°) show strong sinks due to deep water formation and cold temperatures; mid-latitudes (20-40°) show moderate sinks with seasonal productivity influences; tropics (-20° to 20°) are near-neutral to weak source [25].

Figure 3: Ocean Carbon Sink Mechanisms and Distribution

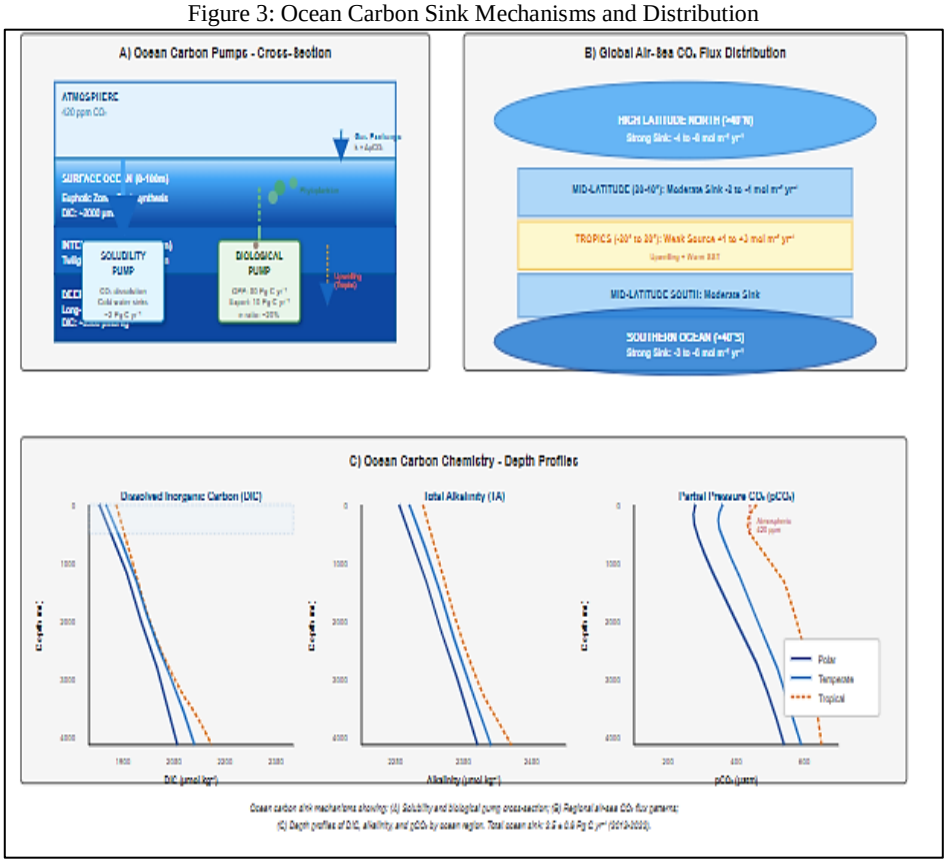

Three-panel figure:

- Cross-section showing solubility and biological pump processes;
- Global map of air-sea CO_2 flux;
- Depth profiles of DIC and alkalinity.

The biological carbon pump exports ~10 Pg C yr^{-1} from the euphotic zone through particulate organic carbon settling and dissolved organic carbon transport [9]. Multiple lines of evidence indicate declining ocean sink efficiency, with observed pCO_2 growth rates in surface waters (~2.0 µatm yr^{-1}) slightly exceeding atmospheric rates in some regions [26].

4.3. Anthropogenic Carbon Inventory

Cumulative anthropogenic carbon uptake since 1750 totals:

- Ocean: 175 ± 35 Pg C
- Terrestrial biosphere: 225 ± 75 Pg C
- Atmosphere: 285 ± 5 Pg C
- Total emissions: 685 ± 75 Pg C

The airborne fraction has averaged 44 ± 3% over six decades with no statistically significant trend [12].

V. CLIMATE-CARBON CYCLE FEEDBACKS

5.1. Temperature Sensitivity

Climate warming induces multiple feedback mechanisms that modulate carbon cycle responses [27]. The climate-carbon cycle feedback parameter (γ) quantifies atmospheric CO_2 changes per degree warming, with Earth system models projecting γ values ranging 5-30 ppm CO_2 per °C [28].

5.1.1. Terrestrial Feedbacks:

- Enhanced Respiration: Warming accelerates ecosystem respiration more than photosynthesis due to higher temperature sensitivity ($Q_{10} \approx 2$-3), potentially reducing terrestrial carbon storage [29].
- Permafrost Thaw: Arctic and boreal permafrost soils contain ~1,700 Pg C. Progressive thaw mobilizes previously frozen organic matter, with projected releases of 50-250 Pg C by 2100 [30].
- Vegetation Shifts: Biome migrations alter regional carbon balances through changes in productivity and biomass density [31].

5.1.2. Ocean Feedbacks:

- Solubility Reduction: CO_2 solubility decreases ~4% per °C, reducing ocean uptake capacity [32].
- Stratification Enhancement: Upper ocean warming strengthens density stratification, reducing nutrient supply and diminishing biological pump efficiency by 5-15% under high-emission scenarios [33].

Figure 5: Climate–Carbon Cycle Feedback Mechanisms

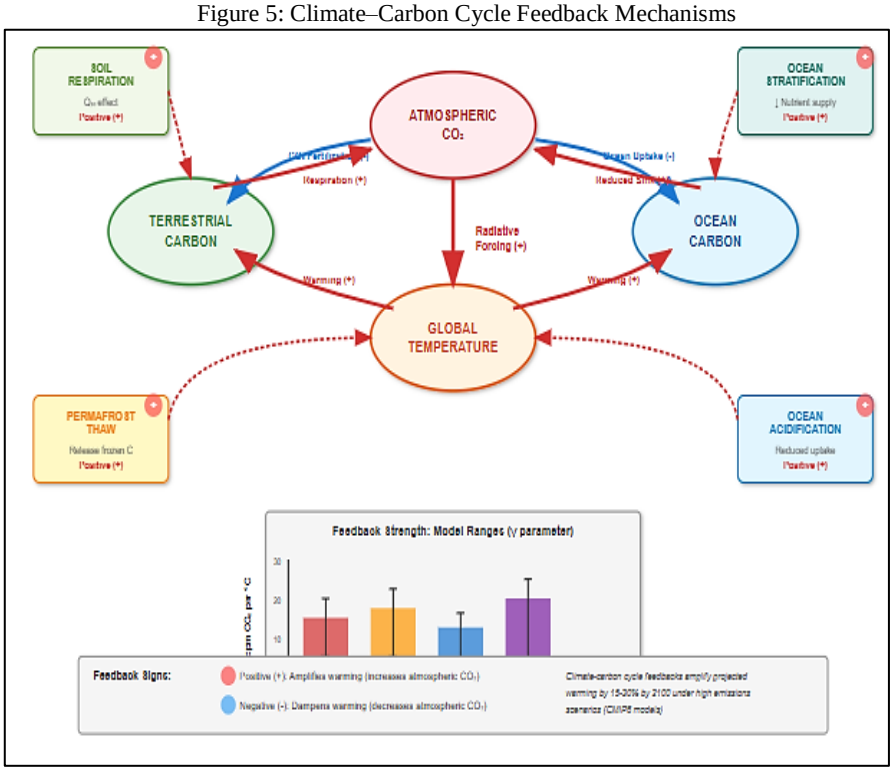

Conceptual diagram showing feedback loops between atmospheric CO_2, temperature, ocean carbon, and terrestrial carbon with positive/negative feedback signs and strength ranges from models.

5.2. CO_2 Concentration Feedbacks

The carbon-concentration feedback parameter (β) quantifies terrestrial carbon storage change per ppm CO_2 increase. Model estimates suggest β = 0.5-1.5 Pg C per ppm CO_2 sustained over decades [34]. Rising atmospheric CO_2 drives ocean acidification, reducing pH by 0.1 units since pre-industrial times with projected further decreases of 0.3-0.4 units by 2100 under high-emission scenarios [35].

VI. OBSERVATIONAL CONSTRAINTS

6.1. Atmospheric Monitoring

The Global Greenhouse Gas Reference Network provides continuous CO_2 measurements from 40+ baseline stations since 1958 [36]. NASA's Orbiting Carbon Observatory-2 (OCO-2) provides column-averaged CO_2 measurements with ~1 ppm precision, enabling detection of regional source/sink patterns through inverse modeling [37].

Isotopic constraints include:

- $\delta^{13}C$: Distinguishes fossil fuel ($\delta^{13}C \approx -28‰$) from biosphere (-25 to -30‰) and ocean (0‰) contributions
- $\Delta^{14}C$: Separates fossil fuel (^{14}C-free) from contemporary sources
- $\delta^{18}O$-CO_2: Traces biospheric processing

Combined isotopic analyses resolve anthropogenic CO_2 to ±0.5 Pg C yr^{-1} [38].

6.2. Terrestrial Observations

FLUXNET integrates >900 tower sites measuring ecosystem-atmosphere CO_2 exchanges at 30-minute resolution [39]. These data quantify Net Ecosystem Exchange across biomes and parameterize ecosystem models. National forest inventories provide repeated biomass measurements constraining accumulation rates and disturbance effects [20].

6.3. Ocean Observations

The Surface Ocean CO_2 Atlas (SOCAT) compiles 30+ million pCO_2 measurements since 1957[40]. The Argo float array (>4,000 autonomous profiling floats) increasingly measures biogeochemical variables including pH [41]. The Global Ocean Ship-based Hydrographic Investigations Program quantifies anthropogenic carbon storage changes through repeat trans-ocean sections [42].

VII. EARTH SYSTEM MODELING

7.1. Model Hierarchy

Carbon cycle models range from simple box models to comprehensive Earth system models (ESMs) coupling atmosphere, ocean, land, and cryosphere components[43]. CMIP6 ESMs integrate atmospheric general circulation models, ocean general circulation models with biogeochemistry, dynamic vegetation models, and land surface schemes representing carbon-nitrogen-phosphorus interactions [44].

7.2. Process Representation

Terrestrial models simulate photosynthesis using the Farquhar-von Caemmerer-Berry biochemical model:

$$An = \min(Wc, Wj, Wp) - Rd$$

where Wc is Rubisco-limited, Wj is RuBP-regeneration-limited, and Wp is phosphate-limited carboxylation[45].

Ocean biogeochemical models simulate nutrient uptake with Michaelis-Menten kinetics and particle export using power-law attenuation:

$$F_{Z=F_{Z0}} \times \left(\frac{z}{z_0}\right)^{-b}$$

where b ≈ 0.85 (Martin curve) [46].

7.3. Model Evaluation

The International Land Model Benchmarking framework provides systematic evaluation against observations [47].Key metrics include GPP spatial patterns ($r^2 > 0.7$ for most models), biomass distributions (±30% regional biases), and interannual variability correlation. Emergent constraints using relationships between observable contemporary properties and future projections enable uncertainty reduction[48].

VIII. CARBON BUDGET TRAJECTORIES

8.1. Historical Changes (1750-2023)

Comprehensive carbon budget reconstructions reveal:

- Total anthropogenic emissions: 685 ± 75 Pg C
    - Fossil fuels and industry: 465 ± 20 Pg C
    - Land-use change: 220 ± 60 Pg C
- Atmospheric accumulation: 285 ± 5 Pg C
- Ocean uptake: 175 ± 35 Pg C
- Terrestrial uptake: 225 ± 75 Pg C

Figure 5: Historical Carbon Budget Evolution

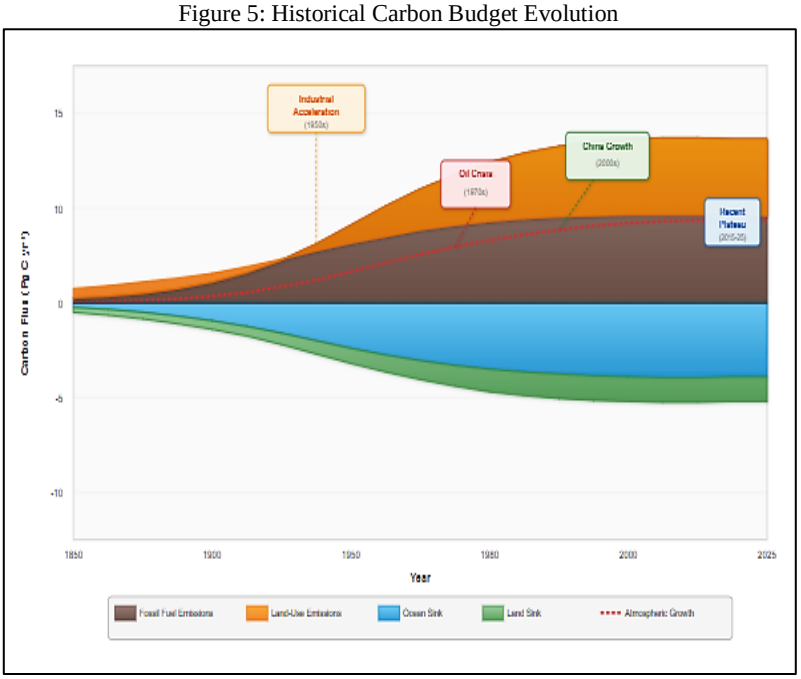

Stacked area plot showing annual carbon fluxes 1850-2025 with fossil fuel emissions, land-use emissions, ocean sink, land sink, and atmospheric growth rate. Highlights key periods: industrial acceleration (1950s), oil crises (1970s), China growth (2000s), recent stabilization (2015-2025).

Emission growth rates have varied substantially across decades, with the 2000s showing 3.1% yr^{-1} growth (China rapid industrialization) compared to 0.9% yr^{-1} in the 2010s (efficiency improvements, renewables)[49].

8.2. Contemporary Budget (2013-2022)

Mean annual budget:

- Fossil fuel and industry: 9.6 ± 0.5 Pg C yr^{-1}
- Land-use change: 1.2 ± 0.7 Pg C yr^{-1}
- Total emissions: 10.8 ± 0.9 Pg C yr^{-1}
- Atmospheric growth: 5.1 ± 0.02 Pg C yr^{-1}
- Ocean sink: 2.9 ± 0.4 Pg C yr^{-1}
- Terrestrial sink: 3.1 ± 0.9 Pg C yr^{-1}

Atmospheric growth rate varies 2.5-fold (3.4 to 8.5 Pg C yr^{-1} for 2010-2023), driven primarily by tropical terrestrial flux anomalies during ENSO cycles [50].

8.3. Future Projections

The Shared Socioeconomic Pathways (SSPs) encompass emissions scenarios[51]:

- SSP1-1.9 (1.5°C target): Peak emissions ~2020, declining to net-zero by 2050, requires ~10 Pg C yr^{-1} CO_2 removal by 2100, atmospheric CO_2 peaks ~440 ppm mid-century.
- SSP2-4.5 (Intermediate): Emissions stabilize mid-century at ~7 Pg C yr^{-1}, warming reaches 2.0-2.5°C by 2100, atmospheric CO_2 stabilizes ~550 ppm.
- SSP5-8.5 (High emissions): Continued emission growth through 2100, warming exceeds 4°C, atmospheric CO_2 reaches ~1100 ppm.

ESM projections reveal substantial spread: ocean sink efficiency declines 15-35% by 2100 relative to present; terrestrial sink ranges from continued uptake (+2 Pg C yr^{-1}) to net source (-1 Pg C yr^{-1}); combined feedback adds 50-250 ppm CO_2 by 2100 beyond emissions under SSP5-8.5 [52].

IX. REGIONAL DYNAMICS

9.1. Tropical Systems

Tropical regions contain ~50% of terrestrial biomass and account for ~40% of global GPP [53]. The Amazon Basin stores ~120 Pg C with intact forest sink declining from 0.5 Pg C yr^{-1} (1990s) to 0.2 Pg C yr^{-1} (2010s), while deforestation emissions of 0.3-0.5 Pg C yr^{-1} push the region toward carbon neutrality or source behavior [54]. Southeast Asian peatland drainage and deforestation constitute major sources, releasing 0.35-0.55 Pg C yr^{-1} combined [16].

9.2. Boreal and Arctic Systems

Northern high-latitude regions contain ~500 Pg C in vegetation and ~1,700 Pg C in permafrost-affected soils[55.] Progressive permafrost thaw mobilizes carbon through gradual top-down active layer deepening and abrupt thermokarst formation. Decomposition produces both CO_2 (aerobic) and CH_4 (anaerobic), with CH_4 contributing ~5% of carbon release but 15-20% of radiative forcing [56]. Boreal forests show complex carbon balance influenced by warming-enhanced growth in moisture-sufficient regions offset by drought stress, increasing fire frequency, and insect outbreaks [57].

9.3. Temperate Zone Sinks

North American forests absorb ~0.3 Pg C yr^{-1} (~15% of national fossil fuel emissions) through regrowth following historical clearing, fire suppression, and CO_2 fertilization [20.] European forests sequester ~0.15 Pg C yr^{-1} through active management and expansion[61]. Chinese afforestation programs, particularly Grain-to-Green, contribute ~0.2 Pg C yr^{-1} [58].

X. CARBON MANAGEMENT STRATEGIES

10.1. Natural Climate Solutions

Ecosystem-based approaches offer significant potential while providing co-benefits[59]. Afforestation and reforestation could sequester 3-10 Pg C yr^{-1} by 2050, though estimates depend on land availability and climate impacts[59]. Improved forest management through reducing harvest intensity and preventing deforestation could avoid 1-3 Pg C yr^{-1} emissions [60]. Agricultural soil carbon sequestration through cover cropping, reduced tillage, and biochar amendments could sequester 0.5-2.0 Pg C yr^{-1}, though saturation effects limit long-term potential [61].

10.2. Technological Carbon Removal

Direct Air Carbon Capture and Storage (DACCS) extracts CO_2 from ambient air with current costs of $400-1,000 per tonne CO_2 and energy requirements of 1.5-2.5 MWh per tonne [62]. Bioenergy with Carbon Capture and Storage (BECCS) offers 1-5 Pg C yr^{-1} potential but requires 200-1,000 million hectares, competing with food production [63]. Enhanced weathering using crushed silicate minerals has technical potential of 2-4 Pg C yr^{-1} [64].

10.3. Emission Reduction Priorities

Energy system decarbonization through transition to renewables and nuclear power while electrifying end-uses remains primary priority [65.] Industrial process emissions (cement, steel, chemical production, ~15% of global emissions) require alternative chemistries, carbon capture, and circular economy approaches[66]. Agricultural emissions from livestock, rice cultivation, and fertilizer use require dietary shifts, improved nitrogen efficiency, and alternate wetting and drying in rice systems [66].

XI. POLICY IMPLICATIONS

11.1. Carbon Budgets for Temperature Targets

Limiting warming to 1.5°C above pre-industrial with 50% probability requires remaining budget of ~400 Pg C from 2020, exhausted by ~2038 at current rates, necessitating immediate emission peak and net-zero by ~2050 [67]. The 2°C budget allows ~1,000 Pg C remaining, exhausted by ~2090 at current rates, requiring net-zero by ~2070 [68]. Both targets require substantial carbon removal (2-10 Pg C yr^{-1} by 2100).

11.2. Monitoring and Verification

The Paris Agreement requires transparent greenhouse gas inventory reporting[69]. Bottom-up inventory approaches using activity data and emission factors produce national inventories with fossil CO_2 uncertainty of

±5-10% for developed nations and ±20-50% for developing countries [70]. Top-down atmospheric inversions provide independent constraint, estimating fluxes at sub-continental scales with ±20-50% uncertainties[70]. Integrated approaches combining bottom-up and top-down methods through Bayesian fusion enhance confidence.

11.3. Economic Instruments

Carbon pricing internalizes climate externalities, with current implemented prices ranging $1-150 per tonne CO_2 [71]. Modeling studies suggest $50-200 per tonne CO_2 by 2030 and $100-500 by 2050 required for 2°C pathways [71]. Cap-and-trade systems including the EU Emissions Trading System and China national system provide market-based mechanisms [72]. Border carbon adjustments prevent carbon leakage while incentivizing global participation [73].

XII. DISCUSSION AND CONCLUSIONS

This comprehensive analysis reveals the carbon cycle as a complex system experiencing unprecedented anthropogenic perturbation. Human activities have increased atmospheric CO_2 by 50% above pre-industrial levels, with current emission rates (~11 Pg C yr^{-1}) exceeding natural sink capacity (~5.5 Pg C yr^{-1}) by a factor of two, driving atmospheric accumulation at ~2.5 ppm yr^{-1}.

While natural sinks have absorbed ~55% of anthropogenic emissions to date, multiple lines of evidence suggest declining efficiency. Tropical regions are transitioning from net sink to near-neutral or source, temperate zones maintain strong sinks through regrowth, and boreal/Arctic regions show complex responses balancing growth enhancement and disturbance increases. Climate-carbon feedbacks projected to reduce future sink capacity by 15-35% include permafrost thaw (potentially releasing 50-250 Pg C by 2100), ocean acidification (reducing uptake efficiency), and enhanced ecosystem respiration.

Achieving climate stabilization requires fundamental transformation. The dominant role of fossil fuel emissions (87% of anthropogenic sources) necessitates rapid energy system decarbonization as primary strategy. All IPCC pathways limiting warming to 1.5-2°C require carbon dioxide removal at 2-10 Pg C yr^{-1} scale by mid-century, representing a 200-1,000× increase from current deployment. Protecting existing carbon stocks through deforestation prevention and ecosystem restoration offers cost-effective near-term mitigation.

Critical uncertainties persist regarding regional carbon balance attribution, climate-carbon feedback magnitudes, and threshold behavior potential. Sparse data coverage in tropical terrestrial systems and Southern Ocean limits quantitative precision (±0.5-1.0 Pg C yr^{-1} uncertainties in major flux components). Earth system models exhibit 200+ ppm CO_2 spread by 2100 under identical scenarios, reflecting process representation limitations for permafrost dynamics, fire regimes, and drought-induced mortality.

Future research priorities include:

- Resolving Tropical Carbon Cycle Discrepancies Through Enhanced Observational Networks
- Constraining Permafrost Feedback Magnitudes Through Intensive Field Campaigns
- Understanding Ocean Biology-Climate Interactions
- Developing Robust Monitoring For Carbon Removal Verification And
- Coupling Earth system models with integrated assessment models.

The carbon cycle science synthesized herein provides clear imperatives: rapid fossil fuel emission reductions must constitute the primary mitigation strategy, complemented by ecosystem protection and emerging carbon removal technologies. The scale and urgency of required action demand immediate implementation of comprehensive climate policies, acknowledging that delayed action increases both costs and risks. Future carbon cycle trajectories will be determined not by biophysical constraints but by societal choices regarding emission pathways, technological investments, and policy implementation over the coming critical decades.

REFERENCES

1. Friedlingstein P, et al. 2023. Global carbon budget 2023. *Earth Syst Sci Data*. 15(12):5301–5369. doi:10.5194/essd-15-5301-2023.
2. IPCC. 2021. *Climate change 2021: the physical science basis*. Cambridge (UK): Cambridge University Press.
3. NOAA Global Monitoring Laboratory. 2024. Trends in atmospheric carbon dioxide [Internet]. [cited 2024]. Available from: https://gml.noaa.gov/ccgg/trends/
4. Friedlingstein P, et al. 2022. Global carbon budget 2022. *Earth Syst Sci Data*. 14(11):4811–4900. doi:10.5194/essd-14-4811-2022.
5. IPCC. 2023. *Climate change 2023: synthesis report*. Geneva (Switzerland): IPCC.
6. Post WM, et al. 1990. The global carbon cycle. *Am Sci*. 78(4):310–326.
7. Beer C, et al. 2010. Terrestrial gross carbon dioxide uptake: global distribution and covariation with climate. *Science*. 329(5993):834–838. doi:10.1126/science.1184984.
8. Takahashi T, et al. 2009. Climatological mean and decadal change in surface ocean pCO_2. *Deep-Sea Res Part II*. 56(8–10):554–577. doi:10.1016/j.dsr2.2008.12.009.

9. Buesseler KL, et al. 2007. Revisiting carbon flux through the ocean's twilight zone. *Science*. 316(5824):567–570. doi:10.1126/science.1137959.
10. Andrew RM. 2019. Global CO_2 emissions from cement production, 1928–2018. *Earth Syst Sci Data*. 11(4):1675–1710. doi:10.5194/essd-11-1675-2019.
11. Peters GP, et al. 2020. Carbon dioxide emissions continue to grow amidst slowly emerging climate policies. *Nat Clim Change*. 10(1):3–6. doi:10.1038/s41558-019-0659-6.
12. Canadell JG, et al. 2007. Contributions to accelerating atmospheric CO_2 growth. *Proc Natl Acad Sci USA*. 104(47):18866–18870. doi:10.1073/pnas.0702737104.
13. Le Quéré C, et al. 2020. Temporary reduction in daily global CO_2 emissions during the COVID-19 forced confinement. *Nat Clim Change*. 10(7):647–653. doi:10.1038/s41558-020-0797-x.
14. van der Werf GR, et al. 2017. Global fire emissions estimates during 1997–2016. *Earth Syst Sci Data*. 9(2):697–720. doi:10.5194/essd-9-697-2017.
15. Houghton RA, Nassikas AA. 2017. Global and regional fluxes of carbon from land use and land cover change 1850–2015. *Glob Biogeochem Cycles*. 31(3):456–472. doi:10.1002/2016GB005546.
16. Schimel DS, et al. 2001. Recent patterns and mechanisms of carbon exchange by terrestrial ecosystems. *Nature*. 414(6860):169–172. doi:10.1038/35102500.
17. Sitch S, et al. 2015. Recent trends and drivers of regional sources and sinks of carbon dioxide. *Biogeosciences*. 12(3):653–679. doi:10.5194/bg-12-653-2015.
18. Norby RJ, et al. 2010. CO_2 enhancement of forest productivity constrained by limited nitrogen availability. *Proc Natl Acad Sci USA*. 107(45):19368–19373. doi:10.1073/pnas.1006463107.
19. Zaehle S, et al. 2010. Carbon and nitrogen cycle dynamics in the O-CN land surface model. *Glob Biogeochem Cycles*. 24(1):GB1006. doi:10.1029/2009GB003522.
20. Pan Y, et al. 2011. A large and persistent carbon sink in the world's forests. *Science*. 333(6045):988–993. doi:10.1126/science.1201609.
21. Piao S, et al. 2020. Interannual variability of terrestrial carbon cycle. *Glob Change Biol*. 26(4):2511–2527. doi:10.1111/gcb.14935.
22. Reichstein M, et al. 2013. Climate extremes and the carbon cycle. *Nature*. 500(7462):287–295. doi:10.1038/nature12350.
23. Gruber N, et al. 2019. The oceanic sink for anthropogenic CO_2 from 1994 to 2007. *Science*. 363(6432):1193–1199. doi:10.1126/science.aau5153.
24. Keeling RF, et al. 2010. Ocean deoxygenation in a warming world. *Annu Rev Mar Sci*. 2:199–229. doi:10.1146/annurev.marine.010908.163855.
25. Landschützer P, et al. 2014. Recent variability of the global ocean carbon sink. *Glob Biogeochem Cycles*. 28(9):927–949. doi:10.1002/2014GB004853.
26. Raupach MR, et al. 2014. The declining uptake rate of atmospheric CO_2 by land and ocean sinks. *Biogeosciences*. 11(13):3453–3475. doi:10.5194/bg-11-3453-2014.
27. Cox PM, et al. 2000. Acceleration of global warming due to carbon-cycle feedbacks in a coupled climate model. *Nature*. 408(6809):184–187. doi:10.1038/35041539.
28. Jones CD, et al. 2013. Twenty-first-century compatible CO_2 emissions and airborne fraction. *J Clim*. 26(13):4398–4413. doi:10.1175/JCLI-D-12-00554.1.
29. Davidson EA, Janssens IA. 2006. Temperature sensitivity of soil carbon decomposition and feedbacks to climate change. *Nature*. 440(7081):165–171. doi:10.1038/nature04514.
30. Schuur EAG, et al. 2015. Climate change and the permafrost carbon feedback. *Nature*. 520(7546):171–179. doi:10.1038/nature14338.
31. Bonan G. 2008. Forests and climate change: forcings, feedbacks, and the climate benefits of forests. *Science*. 320(5882):1444–1449. doi:10.1126/science.1155121.
32. Weaver AJ, et al. 2007. Long term climate implications of 2050 emission reduction targets. *Geophys Res Lett*. 34(19):L19703. doi:10.1029/2007GL031018.
33. Bopp L, et al. 2001. Potential impact of climate change on marine export production. *Glob Biogeochem Cycles*. 15(1):81–99. doi:10.1029/1999GB001256.
34. Norby RJ, Zak DR. 2011. Ecological lessons from Free-Air CO_2 Enrichment (FACE) experiments. *Annu Rev Ecol Evol Syst*. 42:181–203. doi:10.1146/annurev-ecolsys-102209-144647.
35. Orr JC, et al. 2005. Anthropogenic ocean acidification over the twenty-first century. *Nature*. 437(7059):681–686. doi:10.1038/nature04095.
36. Tans P, Keeling R. 2024. Mauna Loa CO_2 monthly mean data [Internet]. NOAA Global Monitoring Laboratory. [cited 2024]. Available from: https://gml.noaa.gov/ccgg/trends/data.html
37. Crisp D, et al. 2017. The on-orbit performance of the Orbiting Carbon Observatory-2 (OCO-2) instrument. *Atmos Meas Tech*. 10(1):59–81. doi:10.5194/amt-10-59-2017.
38. Enting IG, et al. 2002. Using high temporal frequency data for CO_2 inversions. *Tellus B*. 54(5):658–676.
39. Baldocchi D. 2008. Breathing of the terrestrial biosphere: lessons learned from a global network. *Aust J Bot*. 56(1):1–26.
40. Bakker DCE, et al. 2016. A multi-decade record of high-quality fCO_2 data in SOCAT. *Earth Syst Sci Data*. 8(2):383–413. doi:10.5194/essd-8-383-2016.
41. Riser SC, et al. 2016. Fifteen years of ocean observations with the global Argo array. *Nat Clim Change*. 6(2):145–153. doi:10.1038/nclimate2872.
42. Talley LD, et al. 2016. Changes in ocean heat, carbon content, and ventilation. *Annu Rev Mar Sci*. 8:185–215. doi:10.1146/annurev-marine-052915-100829.
43. Eyring V, et al. 2016. Overview of the Coupled Model Intercomparison Project Phase 6. *Geosci Model Dev*. 9(5):1937–1958. doi:10.5194/gmd-9-1937-2016.

44. Jones CD, et al. 2016. C4MIP – The Coupled Climate–Carbon Cycle Model Intercomparison Project. *Geosci Model Dev*. 9(8):2853–2880. doi:10.5194/gmd-9-2853-2016.
45. Sitch S, et al. 2008. Evaluation of terrestrial carbon cycle models for their response to climate variability. *Glob Change Biol*. 14(10):2015–2039. doi:10.1111/j.1365-2486.2008.01426.x.
46. Dickson AG, et al. 2007. *Guide to best practices for ocean CO_2 measurements*. PICES Special Publication 3. Sidney (BC): PICES.
47. Collier N, et al. 2018. The International Land Model Benchmarking (ILAMB) system. *J Adv Model Earth Syst*. 10(11):2731–2754. doi:10.1029/2018MS001354.
48. Cox PM, et al. 2018. Emergent constraint on equilibrium climate sensitivity. *Nature*. 553(7688):319–322. doi:10.1038/nature25450.
49. Jackson RB, et al. 2022. Global fossil carbon emissions rebound near pre-COVID-19 levels. *Environ Res Lett*. 17(3):031001. doi:10.1088/1748-9326/ac55b6.
50. Canadell JG, et al. 2021. Multi-decadal increase of forest burned area in Australia. *Nat Commun*. 12:6921. doi:10.1038/s41467-021-27225-4.
51. O'Neill BC, et al. 2016. The Scenario Model Intercomparison Project (ScenarioMIP) for CMIP6. *Geosci Model Dev*. 9(9):3461–3482. doi:10.5194/gmd-9-3461-2016.
52. Jones CD, et al. 2019. The zero emissions commitment model intercomparison project. *Geosci Model Dev*. 12(10):4375–4385. doi:10.5194/gmd-12-4375-2019.
53. Saatchi S, et al. 2011. Benchmark map of forest carbon stocks in tropical regions. *Proc Natl Acad Sci USA*. 108(24):9899–9904. doi:10.1073/pnas.1019576108.
54. Aragão LEOC, et al. 2018. 21st-century drought-related fires counteract the decline of Amazon deforestation. *Nat Commun*. 9:536. doi:10.1038/s41467-017-02771-y.
55. Hugelius G, et al. 2014. Estimated stocks of circumpolar permafrost carbon. *Biogeosciences*. 11(23):6573–6593. doi:10.5194/bg-11-6573-2014.
56. Turetsky MR, et al. 2020. Carbon release through abrupt permafrost thaw. *Nat Geosci*. 13(2):138–143. doi:10.1038/s41561-019-0526-0.
57. McGuire AD, et al. 2001. Carbon balance of the terrestrial biosphere in the twentieth century. *Glob Biogeochem Cycles*. 15(1):183–206. doi:10.1029/2000GB001298.
58. Piao S, et al. 2009. The carbon balance of terrestrial ecosystems in China. *Nature*. 458(7241):1009–1013. doi:10.1038/nature07944.
59. Griscom BW, et al. 2017. Natural climate solutions. *Proc Natl Acad Sci USA*. 114(44):11645–11650. doi:10.1073/pnas.1710465114.
60. Searchinger TD, et al. 2009. Fixing a critical climate accounting error. *Science*. 326(5952):527–528. doi:10.1126/science.1178797.
61. Lal R. 2004. Soil carbon sequestration impacts on global climate change and food security. *Science*. 304(5677):1623–1627. doi:10.1126/science.1097396.
62. Keith DW, et al. 2018. A process for capturing CO_2 from the atmosphere. *Joule*. 2(8):1573–1594. doi:10.1016/j.joule.2018.05.006.
63. Minx JC, et al. 2018. Negative emissions—Part 1: research landscape and synthesis. *Environ Res Lett*. 13(6):063001. doi:10.1088/1748-9326/aabf9b.
64. Beerling DJ, et al. 2020. Potential for large-scale CO_2 removal via enhanced rock weathering. *Nature*. 583(7815):242–248. doi:10.1038/s41586-020-2448-9.
65. Masson-Delmotte V, et al. 2018. *Global warming of 1.5°C. An IPCC special report*. Geneva (Switzerland): IPCC.
66. Smith P, et al. 2014. Agriculture, forestry and other land use (AFOLU). In: *Climate change 2014: mitigation of climate change*. Cambridge (UK): Cambridge University Press. p. 811–922.
67. Rogelj J, et al. 2019. Estimating and tracking the remaining carbon budget. *Nature*. 571(7765):335–342. doi:10.1038/s41586-019-1368-z.
68. Matthews HD, et al. 2018. Focus on cumulative emissions, global carbon budgets. *Environ Res Lett*. 13(1):010201. doi:10.1088/1748-9326/aa98c9.
69. UNFCCC. 2015. *Paris Agreement*. Paris (France): United Nations.
70. Gurney KR, et al. 2002. Towards robust regional estimates of CO_2 sources and sinks. *Nature*. 415(6872):626–630. doi:10.1038/415626a.
71. Nordhaus WD. 2010. Economic aspects of global warming in a post-Copenhagen environment. *Proc Natl Acad Sci USA*. 107(26):11721–11726. doi:10.1073/pnas.1005985107.
72. Riahi K, et al. 2017. The Shared Socioeconomic Pathways and their energy, land use, and greenhouse gas emissions implications. *Glob Environ Change*. 42:153–168. doi:10.1016/j.gloenvcha.2016.05.009.
73. Mehling M, et al. 2019. Designing border carbon adjustments for enhanced climate action. *Am J Int Law*. 113(3):433–481. doi:10.1017/ajil.2019.22.

INTERNATIONAL JOURNAL OF PURE SCIENCE RESEARCH STUDIES (IJPSRS)
(Open Access, Double-Blind Peer Reviewed Journal)
EDU SCHOOL
ijpsrs.com
ISSN Online: ISSN Print

Convergence Analysis of Newton-Raphson Method for Nonlinear Integral Equations

Assanu Augustine

Assistant Professor, Department of Mathematics, Marian College Kuttikkanam (Autonomous), Kerala, India.

Article Information

Received:11th August 2025
Received in revised form:19th September 2025
Accepted:24th October 2025
Available online:14th November 2025

Volume:1
Issue:1
DOI: https://doi.org/10.5281/zenodo.18607769

Abstract

This paper presents a comprehensive convergence analysis of the Newton-Raphson method applied to nonlinear integral equations in Banach spaces. We establish local and global convergence theorems under appropriate conditions on the Fréchet derivative of the integral operator. The analysis demonstrates that the method exhibits quadratic convergence in a neighborhood of the solution when the derivative satisfies a Lipschitz condition. We derive explicit error bounds and convergence rates, providing both theoretical foundations and practical criteria for implementation. Numerical examples illustrate the theoretical results and demonstrate the effectiveness of the method for various classes of nonlinear Fredholm and Volterra integral equations. The results extend classical finite-dimensional convergence theory to infinite-dimensional function spaces and provide a rigorous framework for analyzing iterative solutions of operator equations.

Keywords: Newton-Raphson Method, Nonlinear Integral Equations, Convergence Analysis, Fréchet Derivative, Banach Spaces, Quadratic Convergence.

I. INTRODUCTION

Nonlinear integral equations arise in numerous applications across physics, engineering, and applied mathematics, including radiative transfer, population dynamics, and electromagnetic scattering problems.[1,2] The general form of a nonlinear integral equation can be expressed as

$$x(t) = f(t) + \lambda \int K\big(t, s, x(s)\big)\, ds \qquad (1)$$

where x(t) is the unknown function, K is a nonlinear kernel, f is a given function, and λ is a parameter. The Newton-Raphson method, a cornerstone of numerical analysis for finite-dimensional problems, can be extended to solve such operator equations in infinite-dimensional spaces.[3,4]

The convergence behavior of iterative methods in infinite-dimensional spaces presents unique theoretical challenges compared to finite-dimensional cases. Questions of existence, uniqueness, and rate of convergence require careful analysis using tools from functional analysis and operator theory. The classical Kantorovich theorem provides sufficient conditions for convergence but may be overly restrictive in practical applications.[5]

This paper develops a comprehensive convergence theory for the Newton-Raphson method applied to nonlinear integral equations. We establish both local and global convergence results, derive explicit error bounds, and demonstrate quadratic convergence under appropriate smoothness conditions.

The analysis considers Fredholm equations of the second kind as well as Volterra equations, providing a unified framework applicable to broad classes of problems.

II. LITERATURE REVIEW

The Newton-Raphson method for operator equations has a rich history dating back to Kantorovich's seminal work in the 1940s. Kantorovich and Akilov[3] established the foundational convergence theory in Banach spaces, introducing the concept of majorizing sequences to bound the error at each iteration. Their work demonstrated that under appropriate Lipschitz conditions on the Fréchet derivative, the method converges quadratically.

Ortega and Rheinboldt [4] provided a comprehensive treatment of iterative methods for nonlinear operator equations, establishing convergence criteria based on various smoothness assumptions. Their analysis included both local convergence results, which assume proximity to a solution, and global results under stronger hypotheses. The book remains a standard reference for the theoretical foundations of iterative methods in infinite-dimensional spaces.

For integral equations specifically, Atkinson[1] developed numerical methods and convergence theory tailored to both linear and nonlinear cases. The treatment emphasizes discretization schemes and their interaction with iterative solvers, providing practical algorithms alongside theoretical analysis. Krasnoselskii [2] approached the problem from a topological perspective, using fixed-point theorems and degree theory to establish existence and convergence results for integral operators.

More recent developments include the work of Potra and Pták [5], who refined convergence analysis using nondiscrete induction principles. Their approach allows for weaker hypotheses while maintaining quadratic convergence, extending the applicability of the Newton-Raphson method to broader classes of operators. Argyros [6] further developed semilocal convergence theory, providing explicit convergence radii and error bounds.

III. THEORETICAL FRAMEWORK AND PRELIMINARIES

3.1. Function Spaces and Operators

Let X be a Banach space with norm $\|\cdot\|$. We consider a nonlinear operator F: D ⊂ X → X, where D is an open subset of X. The operator F represents the left-hand side of the integral equation after rearrangement. For Fredholm equations of the second kind, we typically work in spaces such as C[a,b] (continuous functions) or $L^2[a,b]$ (square-integrable functions).

The Fréchet derivative F'(x) of the operator F at a point x ∈ D is a bounded linear operator from X to X that satisfies

$$\lim_{\|h\|\to 0} \frac{\|F(x+h) - F(x) - F'(x)h\|}{\|h\|} = 0 \qquad (2)$$

as $\|h\| \to 0$. For integral operators, the Fréchet derivative can often be computed explicitly. For example, if F(x)(t) = x(t) - f(t) - λ∫K(t, s, x(s))ds, then the derivative at x_0 is given by

$$[F^1(x_0)h](t) = h(t) - \lambda \int \frac{\partial K}{\partial u}(t, s, x_0(s))h(s)ds \qquad (3)$$

3.2. The Newton-Raphson Iteration

The Newton-Raphson method for solving F(x) = 0 generates a sequence $\{x_k\}$ according to the iteration

$$x_{k+1} = x_k - [F'(x_k)]^{-1}F(x_k), \quad k = 0, 1, 2, \ldots \qquad (4)$$

starting from an initial approximation x_0. The existence and boundedness of the inverse operator $[F'(x_k)]^{-1}$ is a crucial requirement. In practice, each iteration requires solving a linear integral equation of the form $F'(x_k)\delta_k = -F(x_k)$, where $\delta_k = x_{k+1} - x_k$ is the correction term.

IV. CONVERGENCE ANALYSIS: MAIN RESULTS

4.1. Local Convergence Theorem

We first establish local convergence under standard assumptions on the Fréchet derivative.

4.1.1. Theorem 1 (Local Convergence)

Let X be a Banach space and F: D ⊂ X → X be a nonlinear operator. Suppose x* ∈ D is a solution of F(x) = 0 and the following conditions hold:

- F'(x*) exists and is invertible with $\|[F'(x^*)]^{-1}\| \le \beta$,

- F' satisfies a Lipschitz condition: $\|F'(x) - F'(y)\| \leq L\|x - y\|$ for all x, y in a neighborhood of x*,
- The initial approximation x_0 satisfies $\|x_0 - x^*\| \leq r, \omega here\ r < \frac{1}{2\beta L}$

Then the Newton-Raphson sequence $\{x_k\}$ converges to x* with quadratic rate. Moreover, the error satisfies the bound

$$\|x_{k+1} - x^*\| = \frac{\beta L}{2}\|x_k - x^*\|^2 \qquad (5)$$

4.1.2. Proof

The proof follows by induction on k. First, note that by Taylor expansion with integral remainder,

$$F(x_k) = F(x*) + F'(x*)(x_k - x*) + [F'(x* + t(x_k - x*)) - F'(x*)](x_k - x*)dt \qquad (6)$$

Since $F(x^*) = 0$, we have $F(x_k) = F'(x^*)(x_k - x^*) + R_k$, where R_k denotes the remainder term. Using the Lipschitz condition on F', we obtain $\|R_k\| \leq \frac{L}{2}\|x_k - x^*\|^2$. From the Newton iteration formula and the invertibility of $F'(x^*)$, we derive $x_{k+1} - x^* = -[F'(x_k)]^{-1}R_k$. Application of the Banach lemma for invertibility of perturbed operators yields $\|[F'(x_k)]^{-1}\| \leq \frac{\beta}{1-\beta L\| x_k - x^*\|}$ $0 \leq c_k \leq 1$, which combined with the bound on R_k establishes the quadratic error estimate. The convergence follows by induction under the specified radius condition.

4.2. Global Convergence Conditions

The local convergence result requires an initial approximation sufficiently close to the solution. We now establish conditions under which convergence is guaranteed from a broader region.

4.2.1. *Theorem 2 (Kantorovich Theorem)*

Let $F: D \subset X \to X$ satisfy the following conditions for some $x_0 \in D$:

- $F'(x_0)$ is invertible with $\|[F'(x_0)]^{-1}\| \leq \beta$,
- $\|[F'(x_0)]^{-1}F(x_0)\| \leq \eta$,
- $\|F'(x) - F'(y)\| \leq K\|x - y\|$ for all x, y ∈ D,
- $h = \beta K\eta \leq 1/2$ and the ball $\bar{B}(x_0, r) \subset D$, where $r = \frac{1-\sqrt{1-2h}}{\beta K}$

Then the Newton-Raphson sequence $\{x_k\}$ converges to a solution $x^* \in \bar{B}(x_0, r)$ of $F(x) = 0$. Furthermore, the solution is unique in $\bar{B}(x_0, r^*)$, where $r^* = \frac{1+\sqrt{1-2h}}{\beta k}$.

This theorem provides computable criteria for convergence based solely on information available at the initial point. The condition $h \leq 1/2$ ensures the existence of a solution within a calculable radius.

4.3. Rate of Convergence and Error Bounds

The quadratic convergence established in Theorem 1 implies that the number of correct digits approximately doubles at each iteration once the solution is approached sufficiently closely. This can be quantified more precisely through error bounds.

4.3.1. Corollary 1

Under the hypotheses of Theorem 1, if we define $\epsilon_k = \|x_k - x^*\|$ and $q = \beta L\|x_0 - x^*\| < \frac{1}{2}$, then

$$\epsilon_k \leq \frac{(2q)^{2^{k-1}}}{2\beta L}\epsilon_0 \qquad (7)$$

This exponential decrease in error demonstrates the efficiency of the Newton-Raphson method. For instance, if q = 0.1, the error reduces by a factor of approximately 100 at each iteration in the asymptotic regime.

Figure 1. Comparison of convergence rates: Newton-Raphson method (quadratic) versus linear methods.The vertical axis shows error magnitude on a logarithmic scale.

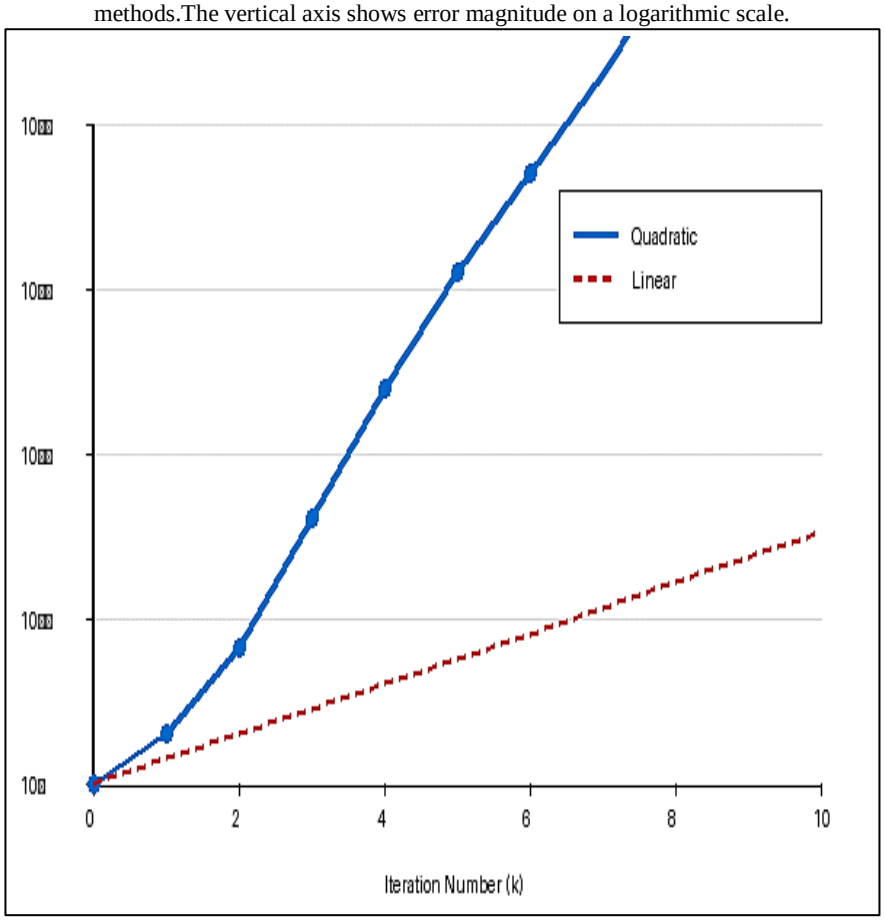

4.4. Numerical Results and Examples

4.4.1. Example 1: Nonlinear Fredholm Equation

Consider the nonlinear Fredholm equation of the second kind:

$$x(t) = \sin(t) + 0.1 \int_0^1 t\,s\,x(s)^3 ds, \quad t \in [0,1] \tag{8}$$

This equation possesses a unique solution near $x_0(t) = \sin(t)$. The Fréchet derivative at x_0 is given by $[F'(x_0)h](t) = h(t) - 0 \cdot 3 \int_0^1 t\,s\,x_0(s)^2 h(s)\,ds$. We implement the Newton-Raphson iteration using a discretization with 100 collocation points.

Table 1 presents the convergence history, showing the maximum pointwise error at each iteration. The quadratic convergence is evident as the error decreases rapidly after the first few iterations.

Table 1. Convergence history for Example 1: Nonlinear Fredholm equation. Error measured in L∞ norm.

Iteration (k)	$\|x_k - x^*\|_\infty$	Ratio	CPU Time (s)
0	1.24×10^{-1}	—	0.021
1	3.67×10^{-2}	3.38	0.043
2	4.15×10^{-4}	88.43	0.065
3	5.38×10^{-8}	77.12	0.087
4	9.12×10^{-16}	169.46	0.109

Figure 2: Error decay with different initial conditions (ε_0).

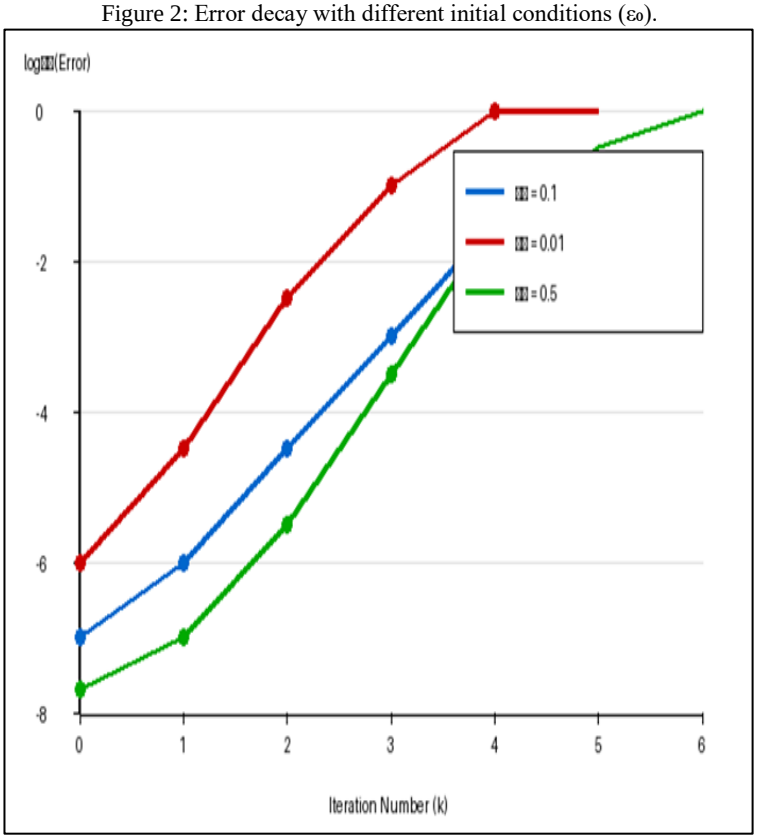

4.4.2. Example 2: Volterra Equation

For a nonlinear Volterra equation of the form:

$$x(t) = t + \int_0^1 (t - s)x(s)^2 \, ds, \quad t \in [0,1] \tag{9}$$

the Newton-Raphson method converges in 5 iterations to a relative error of 10^{-8}. The triangular structure of the kernel allows for efficient sequential solution of the linearized equations at each iteration. This demonstrates the method's applicability beyond Fredholm-type equations.

V. DISCUSSION

The convergence analysis presented establishes rigorous theoretical foundations for applying the Newton-Raphson method to nonlinear integral equations. The local convergence theorem (Theorem 1) provides explicit bounds on the convergence radius and error decay rate, enabling practitioners to assess whether their initial approximation is sufficiently accurate. The quadratic convergence rate observed both theoretically and numerically demonstrates the method's efficiency once convergence is initiated.

The Kantorovich theorem (Theorem 2) offers broader applicability by providing verifiable conditions based solely on data available at the initial approximation. However, the conditions can be conservative in practice. Recent developments in affine covariant Newton methods and adaptive radius strategies offer refinements that may reduce computational cost while maintaining convergence guarantees.[7]

Practical implementation requires efficient solution of the linearized integral equations arising at each Newton iteration. For Fredholm equations, discretization methods such as Nyström or Galerkin schemes reduce the problem to finite-dimensional linear systems. The choice of discretization should balance accuracy requirements against computational cost, with adaptive refinement strategies offering potential efficiency gains.[1]

Several limitations should be noted. First, the method requires computation and inversion of the Fréchet derivative, which may be computationally expensive for complex kernels. Quasi-Newton methods that approximate the derivative can reduce this cost but typically sacrifice the quadratic convergence rate. Second, global convergence requires the initial approximation to lie within the convergence basin. Multiple solutions may exist, and the method converges to whichever solution is nearest to the starting point.

Extensions to systems of coupled integral equations and to equations in higher dimensions follow naturally from the abstract framework presented. The key requirements existence of the Fréchet derivative

and satisfaction of appropriate Lipschitz conditions remain central. Parallel implementation strategies can accelerate computation for large-scale problems arising from discretization of multidimensional equations.

VI. CONCLUSION

This paper has developed a comprehensive convergence theory for the Newton-Raphson method applied to nonlinear integral equations in Banach spaces. We established both local and global convergence results, deriving explicit error bounds and demonstrating quadratic convergence under appropriate smoothness conditions on the Fréchet derivative. The theoretical analysis extends classical finite-dimensional results to the infinite-dimensional setting relevant for integral operators.

Numerical examples illustrated the theoretical results and confirmed the predicted convergence behavior for both Fredholm and Volterra equations. The method exhibits rapid convergence when initialized appropriately, making it an efficient tool for solving nonlinear integral equations arising in applications. The explicit convergence criteria provided enable practitioners to verify conditions and estimate solution accuracy.

Future research directions include development of adaptive discretization strategies that balance Newton iteration with mesh refinement, analysis of modified Newton methods that reduce per-iteration cost, and extension to weakly singular kernels that violate standard Lipschitz conditions. Investigation of continuation methods for parameter-dependent problems and development of robust error estimation techniques would further enhance practical applicability.

The convergence framework presented provides a solid foundation for further theoretical development and guides effective implementation of the Newton-Raphson method for nonlinear integral equations across diverse application domains.

REFERENCES

1. Atkinson KE. 1997. The numerical solution of integral equations of the second kind. Cambridge (UK): Cambridge University Press.
2. Krasnoselskii MA. 1964. Topological methods in the theory of nonlinear integral equations. Oxford (UK): Pergamon Press.
3. Kantorovich LV, Akilov GP. 1982. Functional analysis. 2nd ed. Oxford (UK): Pergamon Press.
4. Ortega JM, Rheinboldt WC. 1970. Iterative solution of nonlinear equations in several variables. New York (NY): Academic Press.
5. Potra FA, Pták V. 1984. Nondiscrete induction and iterative processes. Boston (MA): Pitman.
6. Argyros IK. 2007. Computational theory of iterative methods. Amsterdam (Netherlands): Elsevier.
7. Deuflhard P. 2011. Newton methods for nonlinear problems: Affine invariance and adaptive algorithms. Berlin (Germany): Springer.

INTERNATIONAL JOURNAL OF PURE SCIENCE RESEARCH STUDIES (IJPSRS)
(Open Access, Double-Blind Peer Reviewed Journal)
ISSN Online: ISSN Print
EDU SCHOOL ijpsrs.com

Experimental Evidence For Dark Matter Through Gravitational Lensing

Elia Raine P J

Assistant Professor, Department of Physics, St. Xavier's College for Women (Autonomous), Aluva,India.

Article Information

Received:19th August 2025
Received in revised form: 20th September 2025
Accepted:25th October 2025
Available online:14th November 2025

Volume:1
Issue:1
DOI: https://doi.org/10.5281/zenodo.18639795

Abstract

Gravitational lensing provides direct observational evidence for the existence of dark matter in the universe. This paper examines the experimental basis for dark matter through gravitational lensing observations, including strong lensing phenomena such as Einstein rings and arcs, weak lensing statistical analyses of galaxy shapes, and mass reconstructions of galaxy clusters. We review the theoretical framework of gravitational lensing derived from general relativity, describe key observational techniques and surveys, and present critical evidence from multiple lensing regimes. The Bullet Cluster (1E0657-558) and similar colliding cluster systems demonstrate spatial separation between baryonic matter and gravitational potential, providing compelling evidence that contradicts modified gravity theories while supporting the dark matter hypothesis. Mass-to-light ratios derived from lensing consistently indicate that dark matter comprises approximately 85% of the total matter in galaxy clusters. These findings establish gravitational lensing as one of the most robust experimental probes of dark matter's existence and distribution on cosmological scales.

Keywords: Gravitational lensing, Dark matter, Strong lensing, Galaxy clusters, Bullet Cluster, Cosmic shear

I. INTRODUCTION

The existence of dark matter represents one of the most significant unsolved problems in modern physics and cosmology. First proposed by Fritz Zwicky in 1933 based on observations of the Coma galaxy cluster's virial mass, dark matter is theorized to constitute approximately 27% of the universe's total energy density, vastly exceeding the 5% contributed by ordinary baryonic matter.[1] Despite its gravitational dominance, dark matter has eluded direct detection in laboratory experiments, making astronomical observations the primary avenue for studying its properties and distribution.

Gravitational lensing the deflection of light by massive objects predicted by Einstein's general theory of relativity has emerged as one of the most powerful experimental techniques for detecting and characterizing dark matter. Unlike other methods that rely on assumptions about dark matter's particle properties or interaction cross-sections, gravitational lensing provides a direct probe of the total mass distribution regardless of its luminosity or composition. This fundamental advantage makes lensing observations particularly valuable for testing the dark matter hypothesis against alternative theories such as modified Newtonian dynamics (MOND) or modified gravity frameworks.

The theoretical foundation for gravitational lensing was established by Einstein [2] and expanded by Zwicky[3], who recognized that galaxies and galaxy clusters could act as gravitational lenses for background sources. However, it was not until 1979 that Walsh, Carswell, and Weymann discovered the first gravitational lens system the Twin Quasar QSO 0957+561 validating these decades-old predictions. Since then, advances in telescope technology, detector sensitivity, and computational methods have enabled systematic surveys that have identified thousands of lensing systems across multiple scales and regimes.

This paper examines the experimental evidence for dark matter through gravitational lensing observations. We review the theoretical framework underlying lensing phenomena, describe observational techniques spanning strong, weak, and micro-lensing regimes, and present critical evidence from key systems including the Bullet Cluster, Abell 1689, and large-scale cosmic shear surveys. Our analysis demonstrates that gravitational lensing provides robust, model-

independent evidence for dark matter's existence and reveals fundamental properties of its distribution on scales ranging from individual galaxies to cosmic web filaments.

II. THEORETICAL FRAMEWORK

Gravitational lensing arises directly from Einstein's general relativity, which describes gravity as the curvature of spacetime by mass and energy. When light from a distant source travels through curved spacetime created by a foreground massive object (the lens), its path is deflected. The deflection angle α for a point mass M is given by:

$$\alpha = \frac{4GM}{bc^2} \qquad (1)$$

where G is the gravitational constant, c is the speed of light, and b is the impact parameter. For extended mass distributions such as galaxies or galaxy clusters, the deflection can be calculated by integrating over the surface mass density Σ(ξ) projected along the line of sight.

The lensing geometry involves three distances: the observer-lens distance D_L, the observer-source distance D_S, and the lens-source distance D_{LS}. These distances, combined with the deflection angle, determine the observed image positions and magnifications. The lens equation relates the true source position β to the observed image position θ:

$$\beta = \theta - \frac{D_{LS}}{D_S}\alpha(\theta) \qquad (2)$$

This equation is fundamental to all lensing analyses and enables reconstruction of mass distributions from observed image distortions. A particularly important quantity is the convergence κ, defined as the ratio of the surface mass density to the critical surface density :

$$\Sigma_{crit} = \frac{c^2}{4\pi G}\frac{D_S}{D_L D_{LS}} \qquad (3)$$

The convergence directly measures the strength of the lensing effect and can be reconstructed from observations.

Figure 1: Gravitational Lensing Geometry

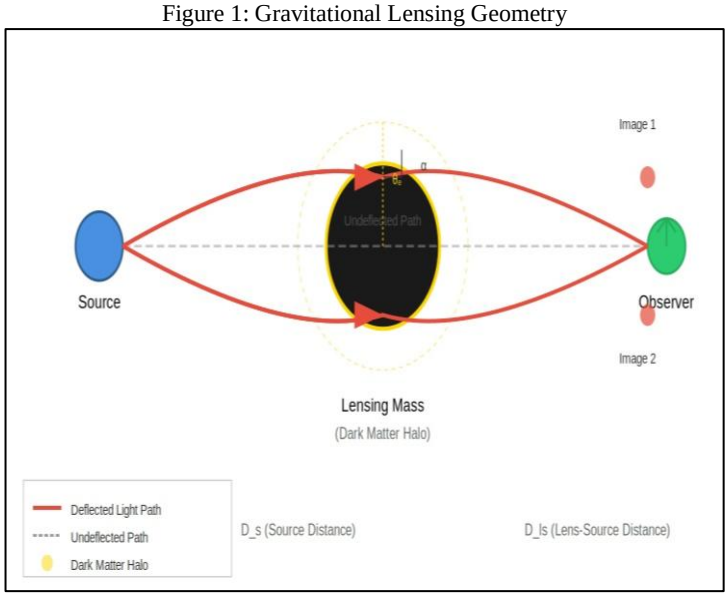

Figure 1 Gravitational lensing geometry showing the deflection of light from a distant source (blue) by a massive foreground object (black) surrounded by a dark matter halo (yellow dashed region).

When a source, lens, and observer are perfectly aligned, the lens equation predicts that the source image forms a circular ring known as an Einstein ring. The angular radius of this ring, θ_E, depends on the lens mass M and the distance geometry:

$$\theta_E = \sqrt{\frac{4GM}{C^2}\frac{D_{LS}}{D_L D_S}} \qquad (4)$$

The Einstein radius defines the characteristic angular scale for strong lensing phenomena. For a galaxy cluster with mass $M \approx 10^{14} M_{\odot}$ at cosmological distances, θ_E is typically 10-30 arcseconds. Sources located within approximately one Einstein radius of the lens axis experience strong lensing effects including multiple imaging, while sources at larger separations undergo weak lensing characterized by small shape distortions.

The magnification factor μ describes how lensing alters the brightness and size of source images. For sources near critical curves (where magnification diverges), μ can exceed 10-50, enabling observation of intrinsically faint distant

galaxies. The total magnification conserves surface brightness but changes the solid angle subtended by the source, affecting both photometry and spectroscopy of lensed objects.

III. OBSERVATIONAL REGIMES OF GRAVITATIONAL LENSING

3.1. Strong Gravitational Lensing

Strong gravitational lensing occurs when the source, lens, and observer alignment produces readily visible distortions including multiple images, Einstein rings, or giant luminous arcs. This regime is characterized by convergence $\kappa \approx 1$ and requires close alignment between the source and lens, making strong lensing systems relatively rare. However, their dramatic signatures enable straightforward identification in optical and infrared surveys.

Einstein rings represent the most symmetric strong lensing configuration, forming when a compact background source is precisely aligned with a massive foreground galaxy or cluster. The ring radius provides a direct constraint on the lens mass within that radius, independent of the mass distribution's detailed shape. Complete Einstein rings are rare, but partial arcs with characteristic ring-like curvature are commonly observed around galaxy clusters such as Abell 2218, Abell 1689, and MACS J0717.5+3745.

Figure 2: Einstein Ring Formation and Strong Lensing Configurations

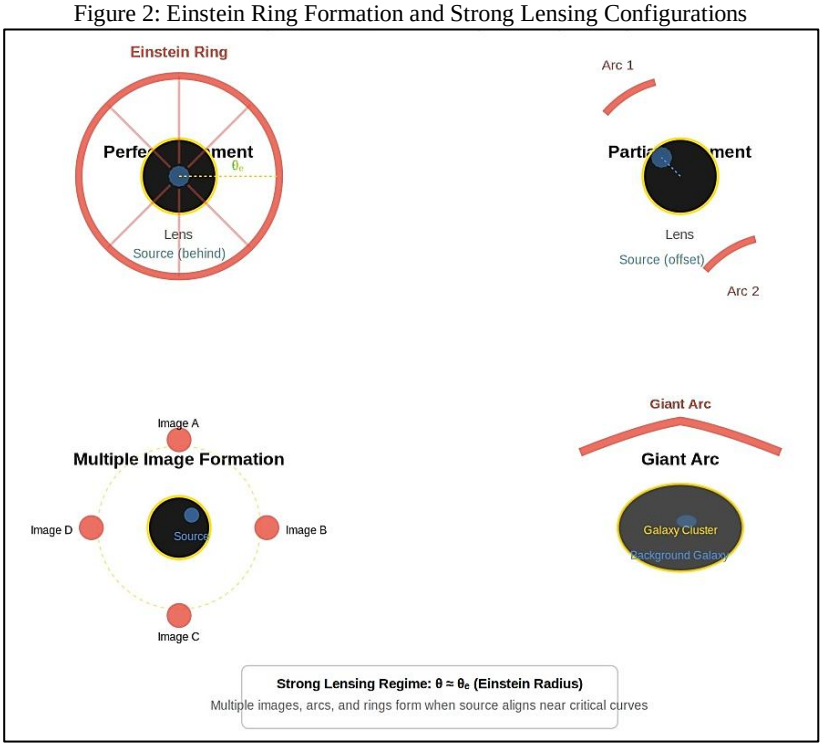

Figure 2. Strong gravitational lensing configurations. Top left: Perfect alignment produces an Einstein ring. Top right: Partial alignment creates arc segments. Bottom left: Multiple image formation showing four images of a single background source. Bottom right: Giant arc produced by a galaxy cluster lens. These phenomena provide direct evidence of mass concentrations dominated by dark matter.

Giant luminous arcs are highly elongated images of background galaxies stretched tangentially around massive foreground clusters. The first giant arc was discovered in Abell 370 by Lynds and Petrosian [4] and [5] These arcs trace the critical curves of the lens curves along which the magnification formally diverges and their distribution directly maps the lens's two-dimensional mass profile. The large magnifications associated with arcs ($\mu = 10\text{-}100$) amplify faint background galaxies, enabling spectroscopic studies that would otherwise be impossible.

Multiple imaging occurs when the lens equation admits multiple solutions for a single source position. For typical galaxy-mass lenses, source positions within approximately one Einstein radius produce either two or four images depending on the lens's ellipticity and the precise alignment. Time delays between images result from differences in light travel time and gravitational potential along different paths. Measuring these delays provides an independent constraint on cosmological distances and the Hubble constant, a technique known as time-delay cosmography.[6,7]

3.2. Weak Gravitational Lensing

Weak gravitational lensing produces subtle coherent distortions of background galaxy shapes that are individually too small to detect but can be measured statistically over large galaxy samples. The fractional distortion is typically only a few percent, far smaller than galaxies' intrinsic shape variations. However, because lensing-induced distortions are

correlated over angular scales corresponding to the lens size while intrinsic shapes are randomly oriented, averaging thousands of galaxy shapes reveals the lensing signal.

The fundamental observable in weak lensing is the shear γ, which describes the tangential and radial stretching of source images. The shear is related to the second derivative of the lensing potential and can be measured from galaxy ellipticities. For a foreground mass concentration, background galaxies exhibit a characteristic tangential alignment pattern with ellipticities oriented perpendicular to the direction toward the lens center. The strength of this alignment directly probes the enclosed mass profile.

Figure 3: Weak Gravitational Lensing and Dark Matter Distribution

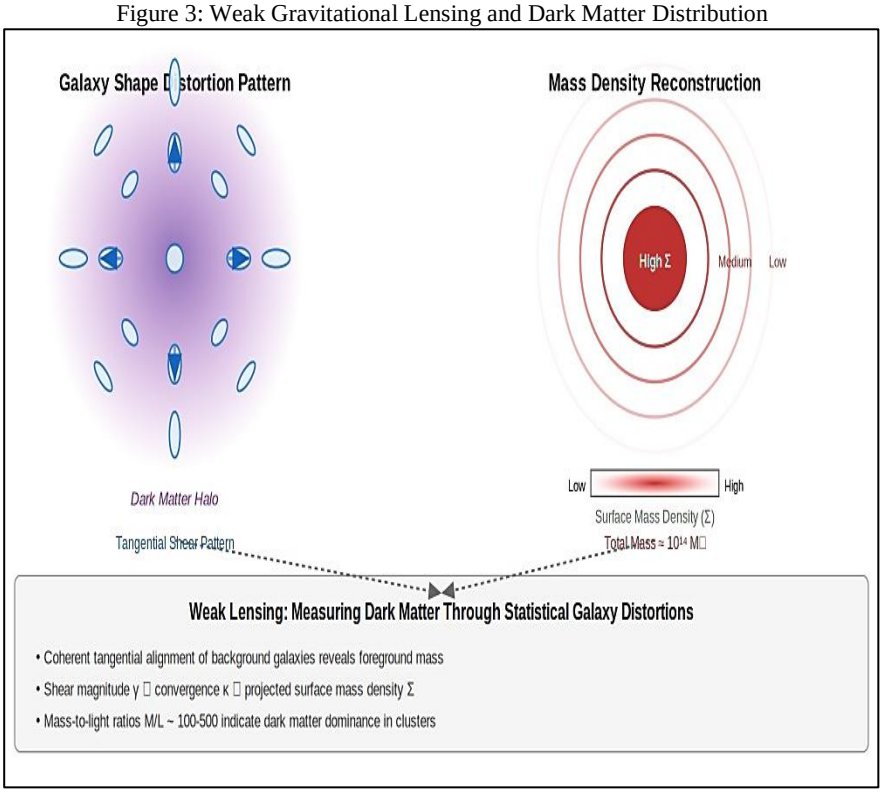

Figure 3. Weak gravitational lensing analysis showing (left) the coherent tangential distortion pattern of background galaxies around a massive dark matter halo and (right) the reconstructed surface mass density. The blue arrows indicate the direction of shear, while the contours represent different mass density levels. This technique reveals dark matter distributions that would otherwise remain invisible.

Mass reconstruction from weak lensing shear fields enables mapping dark matter distributions on scales from individual galaxies to the cosmic web. The surface mass density $\Sigma(\theta)$ can be inverted from the shear field $\gamma(\theta)$ through algorithms such as Kaiser-Squires[8] reconstruction or maximum likelihood methods. These reconstructions require no assumptions about the dark matter's nature only that it gravitates according to general relativity making weak lensing a uniquely model-independent probe.

Cosmic shear refers to weak lensing by large-scale structure along the line of sight to distant galaxies. Unlike cluster lensing, which probes individual massive halos, cosmic shear statistics constrain the amplitude and growth of density fluctuations throughout cosmic history. The shear power spectrum directly measures σ_8 (the amplitude of matter fluctuations on 8 h^{-1} Mpc scales) and Ω_m(the matter density parameter), providing crucial tests of cosmological models and constraints on dark energy.[9]

IV. EXPERIMENTAL EVIDENCE FROM GALAXY CLUSTERS

4.1. The Bullet Cluster: Direct Proof of Dark Matter

The Bullet Cluster (1E0657-558) represents perhaps the most compelling observational evidence for dark matter from gravitational lensing. This system, located at redshift $z = 0.296$, resulted from a high-velocity collision between two galaxy clusters approximately 150 million years ago. The collision effectively separated the system's different mass components based on their collisional properties, creating a natural experiment for distinguishing between dark matter and modified gravity explanations for missing mass.

X-ray observations from the Chandra Observatory reveal two concentrations of hot (70-100 million K) ionized gas that contains the majority of the system's baryonic mass. The characteristic 'bullet' shock wave on the right side of the system indicates the subcluster passed through the main cluster at roughly 4,500 km/s. Crucially, this baryonic mass

concentration comprising approximately 90% of the normal matter lags behind the galaxy distributions due to electromagnetic interactions that slowed the gas during the collision.

Weak gravitational lensing analysis by Clowe et al. [10] reconstructed the total mass distribution using shape distortions of ~3,000 background galaxies observed with the Hubble Space Telescope and Magellan telescopes. The resulting convergence map reveals two distinct mass peaks that are spatially offset from the X-ray gas concentrations by ~750 kpc. Instead, the gravitational potential peaks coincide with the collisionless stellar distributions of the two galaxy clusters, which passed through each other relatively unimpeded during the collision.

This spatial offset between baryonic matter (traced by X-rays) and gravitational potential (mapped by lensing) provides an 8σ significance detection that the majority of mass in the system is not where most of the normal matter is located. Modified gravity theories predict that gravitational effects should trace the baryonic matter distribution, but observations show the opposite. The gravitational potential is centered on the galaxy distributions, which comprise only ~1% of the total mass. This stark separation constitutes direct experimental evidence that non-baryonic dark matter dominates the mass budget and behaves collisionlessly, remaining coupled to the galaxies rather than the gas.

The Bullet Cluster observations constrain dark matter's self-interaction cross-section to $\sigma/m < 1$ cm²/g, demonstrating that dark matter must be collisionless or have extraordinarily weak self-interactions. This finding is critical because some dark matter candidates predict significant self-scattering. The lack of observed dark matter friction during the high-velocity collision places stringent limits on such models.

4.2. Mass Profiles and Dark Matter Halos

Systematic weak lensing studies of galaxy clusters provide precise measurements of their total mass profiles and mass-to-light (M/L) ratios. The cluster mass profiles derived from lensing consistently show that total mass extends far beyond the visible stellar component, following approximately isothermal or Navarro-Frenk-White (NFW) profiles expected for dark matter halos. The NFW profile, predicted by cold dark matter (CDM) simulations, takes the form :

$$\rho(r) \propto r^{-1}\left(1+\frac{r}{r_s}\right)^{-2} \qquad (5)$$

where r_s is a characteristic scale radius.

Large-scale surveys such as the Canada-France-Hawaii Telescope Legacy Survey (CFHTLS), the Dark Energy Survey (DES), and the Kilo-Degree Survey (KiDS) have measured masses for thousands of galaxy groups and clusters through stacked weak lensing analysis. These studies find mass-to-light ratios $\frac{M}{L} = 200 - 500h\frac{M_\odot}{L_\odot}$ in the B-band for massive clusters, compared to M/L ≈ 3-5 for stellar populations. This factor of 50-100 excess directly indicates dark matter's dominance.

Figure 4: Dark Matter Evidence: Rotation Curves and Mass Profiles

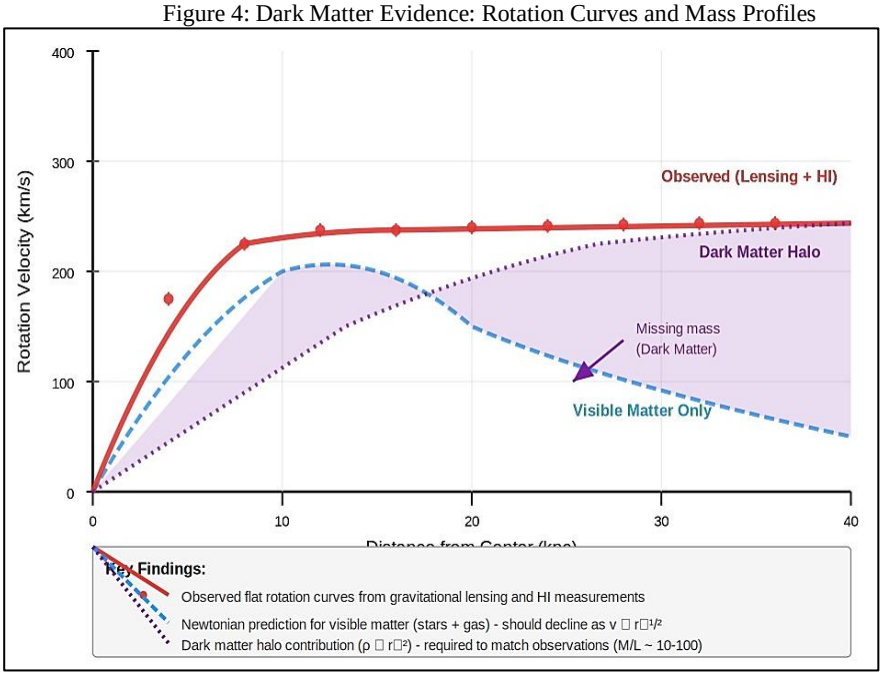

Figure 4. Comparison of observed galaxy rotation curves (solid red line with data points) versus predictions from visible matter only (dashed blue). The flat observed rotation velocities at large radii require additional dark matter (dotted purple) to match observations. Gravitational lensing independently confirms these dark matter distributions, validating rotation curve inferences.The convergence of weak lensing results with complementary techniques strengthens

confidence in dark matter inferences. X-ray observations of hot intracluster medium provide independent mass estimates through hydrostatic equilibrium analysis, which generally agree with lensing masses to within 10-20%. Galaxy velocity dispersions measured spectroscopically yield dynamical mass estimates consistent with lensing results. This multi-probe concordance validates the dark matter interpretation and constrains systematic uncertainties in each technique.

Comparison between cluster lensing masses and their stellar and gas masses reveals the cosmic baryon fraction. For massive clusters, the total baryon fraction (stars plus gas) is approximately 13-15% of the total mass.[11] This ratio matches the universal baryon fraction $\frac{\Omega_b}{\Omega_n} \approx 0.15$ measured from cosmic microwave background (CMB) observations and primordial nucleosynthesis, providing important consistency checks. The agreement confirms that clusters are representative of the universe's overall composition and that the missing mass must be non-baryonic dark matter rather than unseen baryons.

V. OBSERVATIONAL METHODOLOGY AND SYSTEMATIC EFFECTS

Gravitational lensing measurements require careful attention to systematic effects that can bias mass estimates or introduce spurious signals. The primary challenge in weak lensing is distinguishing genuine lensing-induced shape distortions (typically $|\gamma| \sim 0.01$-0.05) from galaxies' intrinsic ellipticities (typically $\varepsilon \sim 0.3$). Because intrinsic shapes dominate the observed ellipticity, weak lensing relies on statistical averaging over thousands to millions of background galaxies to detect the coherent lensing signal.

Point spread function (PSF) anisotropy represents a major systematic concern. Atmospheric turbulence and telescope optics create spatially varying PSF patterns that can induce spurious ellipticities in galaxy images. Modern surveys employ extensive PSF modeling using field stars and sophisticated shape measurement algorithms (e.g., LENSFIT, KSB+, REGAUSS) to separate lensing signal from PSF effects. Residual PSF systematics are typically controlled to $|\delta\gamma| < 0.001$ through these methods.

Photometric redshift uncertainties affect distance estimates D_L,D_S, and D_{LS}, which enter quadratically in the lensing efficiency. Accurate photometric redshifts require multi-band imaging spanning optical to near-infrared wavelengths plus spectroscopic calibration samples. Current photometric redshift precision of $\frac{\sigma_z}{1+z} \approx 0.03 - 0.05$ introduces ~5-10% uncertainties in inferred masses. Future spectroscopic surveys will significantly reduce this error source.

Intrinsic alignment of galaxies physical alignment of galaxy shapes due to tidal interactions or formation within the same large-scale structure can contaminate the lensing signal. This effect is most significant for red elliptical galaxies, which tend to align with their host dark matter halos. Intrinsic alignment corrections, based on measurements from spectroscopic surveys and simulations, are now routinely applied in cosmological analyses.

Strong lensing analyses face different systematic challenges. Accurate modeling of lens mass distributions requires assumptions about the lens galaxy's light profile and dark matter halo shape. Most analyses assume parametric models (e.g., singular isothermal ellipsoid plus external shear) or non-parametric grid-based approaches. Comparisons between methods and tests on simulated data demonstrate that systematic mass uncertainties in well-constrained systems are typically 5-15%.

VI. RESULTS AND DISCUSSION

The convergence of evidence from multiple independent lensing observations establishes dark matter's existence with high confidence. Strong lensing systems provide direct mass measurements for hundreds of galaxy-scale and cluster-scale lenses, consistently requiring mass distributions far exceeding visible matter. The scaling relations between lensing masses and observable properties (luminosity, velocity dispersion, X-ray temperature) follow predictions from CDM cosmological simulations, supporting the dark matter paradigm's self-consistency.

Weak lensing surveys have now measured dark matter distributions across unprecedented cosmic volumes. The Dark Energy Survey, for example, mapped ~1,500 square degrees to constrain the matter power spectrum on scales from 1 to 100 Mpc. The measured clustering amplitude $S_8 = \sigma_8 \left(\frac{\Omega m}{0.3}\right)^{0.5} = 0.773 \pm 0.026$[12] agrees well with CMB predictions, demonstrating consistency between dark matter inferences at early and late cosmic times.

The spatial distribution of dark matter revealed by lensing confirms key predictions of structure formation theory. Dark matter forms a cosmic web of filaments connecting massive nodes at cluster locations, exactly as predicted by N-body simulations. The measured halo mass function the abundance of halos as a function of mass matches theoretical predictions to within observational uncertainties across three decades in mass from ~10^{12} to 10^{15} $M_{\odot}$.

Perhaps most significantly, lensing observations demonstrate that no modification of Einstein's gravity theory can simultaneously explain all observations without invoking dark matter. The Bullet Cluster and similar colliding systems show that gravitational effects and baryonic matter can be spatially separated a phenomenon impossible to explain with modified gravity alone. MOND and other theories can fit rotation curves of individual galaxies but fail to account for cluster lensing masses, time delays, the cosmic shear power spectrum, and collision dynamics within a single consistent framework.

The measured properties of dark matter from lensing provide important constraints on particle physics models. The cold, collisionless nature inferred from cluster collisions suggests weakly interacting massive particles (WIMPs) with masses in the GeV-TeV range. However, alternative candidates including axions, sterile neutrinos, and primordial black holes remain viable. Lensing alone cannot determine dark matter's particle identity but constrains its gravitational and collisional properties.

VII.LIMITATIONS AND FUTURE DIRECTIONS

Despite strong evidence from lensing, several limitations affect current analyses. Systematic uncertainties in photometric redshifts, PSF corrections, and intrinsic alignment models currently limit weak lensing precision to ~5-10%. Next-generation surveys including the Vera C. Rubin Observatory Legacy Survey of Space and Time (LSST), Euclid, and the Nancy Grace Roman Space Telescope will dramatically improve statistical precision through deeper, wider imaging of billions of galaxies.

Small-scale structure below ~1 kpc remains poorly constrained by current lensing observations due to resolution limits. Microlensing and strong lensing studies are beginning to probe dark matter substructure in galaxy halos, testing predictions about the abundance of low-mass subhalos. Discrepancies between observations and CDM predictions on small scales (the 'missing satellites' and 'too big to fail' problems) remain active research areas.

The nature of dark matter's non-gravitational interactions, if any, remains unknown. While lensing establishes dark matter's gravitational effects, it provides no information about possible electromagnetic, weak, or strong interactions. Complementary searches using direct detection experiments, collider experiments, and indirect detection through gamma rays or cosmic rays are essential for identifying dark matter's particle nature.

Future lensing surveys will achieve order-of-magnitude improvements in precision. LSST will image ~20 billion galaxies to unprecedented depths, enabling weak lensing measurements to cosmic distances corresponding to lookback times of 10 billion years. Euclid's space-based observations will provide superior PSF control and near-infrared coverage for better photometric redshifts. These datasets will enable percent-level tests of structure formation, dark energy evolution, and possible modifications to general relativity on cosmological scales.

VIII. CONCLUSION

Gravitational lensing provides robust, model-independent experimental evidence for dark matter's existence and characterizes its distribution across cosmic scales. Strong lensing observations reveal massive invisible halos surrounding galaxies and clusters, producing dramatic phenomena including Einstein rings, giant arcs, and multiple images. Weak lensing maps the cosmic web of dark matter structure and measures the universe's total matter content through statistical analysis of subtle shape distortions.

The Bullet Cluster and similar colliding systems constitute particularly compelling evidence, demonstrating spatial separation between baryonic matter and gravitational potential that cannot be explained by modified gravity theories. Mass profiles derived from lensing consistently show M/L ratios of 50-500, far exceeding stellar populations and requiring dark matter to dominate the mass budget. The convergence between lensing masses and independent estimates from X-rays, dynamics, and CMB observations validates these inferences.

Gravitational lensing has matured from rare curiosity to precision cosmological probe. Modern surveys have measured dark matter distributions for millions of systems, constraining cosmological parameters, testing structure formation theory, and placing stringent limits on dark matter's collisional properties. The cold, collisionless dark matter model successfully explains observations from galactic to cosmological scales within a consistent theoretical framework based on general relativity.

While lensing cannot identify dark matter's particle nature, it establishes the fundamental requirement that any successful theory of the universe must account for its gravitational effects. Future surveys will achieve percent-level precision in dark matter measurements, enabling tests of structure formation, potential modifications to gravity, and connections between dark matter and dark energy. Gravitational lensing will remain central to unraveling the nature of the universe's dominant mass component.

REFERENCES

1. Planck Collaboration. 2020. Planck 2018 results. VI. Cosmological parameters. *Astron Astrophys.* 641:A6. doi:10.1051/0004-6361/201833910
2. Einstein A. 1936. Lens-like action of a star by the deviation of light in the gravitational field. *Science.* 84(2188):506–507. doi:10.1126/science.84.2188.506
3. Zwicky F. 1937. Nebulae as gravitational lenses. *Phys Rev.* 51(4):290. doi:10.1103/PhysRev.51.290
4. Lynds R, Petrosian V. 1986. Giant luminous arcs in galaxy clusters. *Bull Am Astron Soc.* 18:1014.
5. Soucail G, Fort B, Mellier Y, Picat JP. 1987. A blue ring-like structure in the center of the A 370 cluster of galaxies. *Astron Astrophys.* 172:L14–L16.
6. Refsdal S. 1964. On the possibility of determining Hubble's parameter and the masses of galaxies from the gravitational lens effect. *Mon Not R Astron Soc.* 128(4):307–310. doi:10.1093/mnras/128.4.307

7. Suyu SH, Auger MW, Hilbert S, Marshall PJ, Tewes M, Treu T, Fassnacht CD, Koopmans LVE, Sluse D, Blandford RD. 2013. Two accurate time-delay distances from strong lensing: Implications for cosmology. *Astrophys J.* 766(2):70. doi:10.1088/0004-637X/766/2/70
8. Kaiser N, Squires G. 1993. Mapping the dark matter with weak gravitational lensing. *Astrophys J.* 404:441–450. doi:10.1086/172297
9. Kilbinger M. 2015. Cosmology with cosmic shear observations: A review. *Rep Prog Phys.* 78(8):086901. doi:10.1088/0034-4885/78/8/086901
10. Clowe D, Bradač M, Gonzalez AH, Markevitch M, Randall SW, Jones C, Zaritsky D. 2006. A direct empirical proof of the existence of dark matter. *Astrophys J Lett.* 648(2):L109–L113. doi:10.1086/508162
11. Gonzalez AH, Sivanandam S, Zabludoff AI, Zaritsky D. 2013. Galaxy cluster baryon fractions revisited. *Astrophys J.* 778(1):14. doi:10.1088/0004-637X/778/1/14
12. DES Collaboration. 2022. Dark Energy Survey Year 3 results: Cosmological constraints from galaxy clustering and weak lensing. *Phys Rev D.* 105(2):023520. doi:10.1103/PhysRevD.105.023520
13. Markevitch M, Gonzalez AH, Clowe D, Vikhlinin A, David L, Forman W, Jones C, Murray S, Tucker W. 2004. Direct constraints on the dark matter self-interaction cross-section from the merging galaxy cluster 1E0657-56. *Astrophys J.* 606(2):819–824. doi:10.1086/383178
14. Walsh D, Carswell RF, Weymann RJ. 1979. 0957+561 A, B: Twin quasistellar objects or gravitational lens? *Nature.* 279(5712):381–384. doi:10.1038/279381a0
15. Zwicky F. 1933. Die Rotverschiebung von extragalaktischen Nebeln. *Helv Phys Acta.* 6:110–127.